NONDESTRUCTIVE EVALUATION AND STRUCTURAL HEALTH MONITORING BASED ON HIGHLY NONLINEAR SOLITARY WAVES

by

Xianglei Ni

Bachelor of Engineering in Civil Engineering, Tsinghua University, Beijing, 2004

Master of Engineering in Civil Engineering, Dalian University of Technology, Dalian, 2007

Submitted to the Graduate Faculty of

Swanson School of Engineering in partial fulfillment

of the requirements for the degree of

PhD in Civil Engineering

University of Pittsburgh

2011

UNIVERSITY OF PITTSBURGH

SWANSON SCHOOL OF ENGINEERING

This dissertation was presented

by

Xianglei Ni

It was defended on

November 09, 2011

and approved by

Irving J. Oppenheim, PhD, Professor, Civil and Environmental Engineering Department, CMU

Jeen-Shang Lin, PhD, Associate Professor, Civil and Environmental Engineering Department

Julie M. Vandenbossche, PhD, Assistant Professor, Civil and Environmental Engineering Department

Albert To, PhD, Assistant Professor, Mechanocal Engineering and Materials Science Department

Dissertation Director: Piervincenzo Rizzo, PhD, Assistant Professor, Civil and Environmental Department

NONDESTRUCTIVE EVALUATION AND STRUCTURAL HEALTH MONITORING BASED ON HIGHLY NONLINEAR SOLITARY WAVES

Xianglei Ni, PhD

University of Pittsburgh, 2011

Recent decades have witnessed the rapid growth and acceptance of nondestructive evaluation (NDE) techniques in assessment of infrastructures' conditions. Assessing the conditions of infrastructures is important to determine their safety and reliability which have a great impact on today's society. The existing NDE techniques include acoustics, ultrasound, radiology, thermography, electromagnetic method, optical method, and so on. Properly employed NDE techniques can reduce the maintenance and repair cost and improve the reliability of the infrastructures.

In the last two decades, the study of the highly nonlinear solitary waves (HNSWs) has received much attention. Most of these studies focused on the propagation of HNSWs in granular systems, but little work on applications of HNSW-based NDE method has been done. HNSWs are mechanical waves that can form and travel in highly nonlinear systems, one-dimensional chain of identical spheres is one of the most common systems that can support the generation and propagation of HNSWs. In the study presented in this dissertation, a new NDE technique based on the generation and propagation of HNSWs was investigated and applied to different structural materials.

First, fundamental research on the generation of HNSWs in a chain of stainless steel beads by laser pulses was conducted. The results showed that the laser-based generation of HNSWs produces results that are equivalent to those obtained by means of a mechanical striker.

Then, the feasibility of tuning HNSWs by electromagnetically induced precompression was demonstrated experimentally. By changing the precompression on the chain of particles, the properties of the HNSWs could be tuned in a wide range. Then a HNSW-based transducer was designed and built. The transducer was remotely and automatically controlled by National Instruments PXI running Labview. The ability of the new transducer to generate repeatable HNSWs was assessed. Finally, the HNSW transducer was used to monitor cement setting, concrete curing and epoxy curing, to evaluate the bond condition of an aluminum lap-joint, and to detect the impact damages in a composite plate. The results showed that the HNSW-based technique is promising for structural NDE. A pilot numerical study on acoustic lens which is a device can focus the acoustic waves at a focal point was also conducted.

TABLE OF CONTENTS

LIST OF TABLES

LIST OF FIGURES

PREFACE

First, I would like to thank Professor P. Rizzo for providing me the opportunity to perform this research. I couldn't finish this dissertation without his guidance and continuous support through the process of my research.

I sincerely appreciate the collaboration with Dr. J. Yang, Dr. D. Kathri, Prof. C. Daraio at Caltech, and Dr. S. Nassiri, Prof. J. Vandenbossche. I am thankful to Mr. C. Hager for his help in preparing some of the experiments. The help from Mr. X. Zhu in Labview programming is acknowledged.

Financial supports from NSF CMMI-0825983, 2009 ASNT Fellowship Award, and MCSI are acknowledged.

Most of all, I owe my deepest gratitude to my wife and my mother for their love and support.

1.0 INTRODUCTION

The rapidly expanding role of nondestructive evaluation (NDE), also usually called nondestructive testing (NDT), in manufacturing, power, construction, and maintenance industries, as well as in basic research and development, has generated a large demand for practitioners, engineering, and scientists with knowledge of the subject [1]. NDE is defined by the American Society of Nondestructive Testing (ASNT) as comprising those test methods used to examine an object, material or system without impairing its future usefulness [2]. Properly-employed NDE methods can have a dramatic effect on the cost and reliability of objects being tested. The design of new engineering systems often incorporates novel materials whose long-term degradation processes are not well understood. Existing infrastructures are aging and the increase of axle loads on transportation grids is unavoidable. These circumstances demand that damage in new or aging systems can be detected at the earliest possible time in an effort to prevent life-threatening failures that can also lead to costly consequences for the taxpayers and the environment. Effective NDE and Structural Health Monitoring (SHM) techniques able to detect and quantify structural damage are therefore needed to ensure the performance, the proper response, as well as the minimum maintenance costs of any engineering system.

This study attempts to develop a new NDE paradigm based on the use of highly nonlinear solitary waves (HNSWs), able to detect defects at early stages and/or characterize the mechanical properties of materials.

1.1 HIGHLY NONLINEAR SOLITARY WAVES

Highly nonlinear solitary waves (HNSWs) are mechanical waves that can form and travel in highly nonlinear systems [3]. HNSW has a finite wavelength that is independent on its amplitude. The wave speed and frequencyof HNSW are tunable. One-dimensional chain of identical spheres is one of the most common systems that can support the generation and propagation of HNSWs. HNSW in one-dimensional chain of spherical particles was first investigated by Nesterenko [4] analytically and numerically and subsequently by Lazaridi and Nesterenko [5] experimentally. The passage of HNSWs through the contact of two chains which consist of spherical granules with different diameters and masses was investigated experimentally and numerically by Nesterenko et al. [6]. Coste et al. [7] studied experimentally the propagation of high-amplitude solitary waves in a chain of beads under Hertz contact, subjected to a small static force controlled by a dynamometer. Falcon et al. [8] investigated the collision of a one-dimensional column of beads with a fixed wall and developed a non-dissipative numerical model based on a nonlinear interaction law between nearest neighbors which gives results in agreement with the experimental data. Sen et al. [9] studied numerically on the motion of an initial perturbation in a chain of spheres which are under Hertz contact. The

evidence of backscattering of the solitonlike pulse was presented in the presence of the light mass impurities in the Hertzian chain. They suggested that the acoustic backscattering can be a possible probe of buried light mass impurities in granular beds. Chatterjee [10] studied HNSWs in an initially uncompressed one-dimensional chain of elastic spheres with power law interaction where the power law index is greater than but close to unity. An asymptotic solution for the solitary wave was developed. Sen et al. [11] conducted a numerical study on ejection of ferrofluid gains using nonlinear acoustic impulses that might travel as nondispersive solitons. The proposed mechanism has the potential to help design a nozzle-free inkjet printer of unparalleled resolution. Coste and Gilles [12] demonstrated experimentally that at low static precompression, for all beads made of different materials, the acoustic waves propagate in the chain as predicted by Hertz's theory. At larger precompression, after the onset of permanent plastic deformation at the contacts, the brass beads exhibit non-Hertzian behavior. Hinch and Saint-Jean [13] studied the fragmentation of a long line of stationary touching balls when hit on its end by another ball for both linear contact law and Hertz contact law. Manciu et al. [14-15] studied the propagation and backscattering of solution-like pulses in a chain of quartz beads with Hertzian contacts. They presented preliminary data for three-dimensional granular beds and suggested the soliton-like pulses can form and can be used as a valuable tool for probing buried impurities in granular assemblies. Manciu et al. [16] presented a numerical study and demonstrated that the crossing of identical solitary waves in a chain of discrete particles with Hertzian contacts led to the spawning of weak secondary solitary waves at the point of intersection of the solitary waves. Manciu et al. [17] studied the wave propagation in a chain of elastic beads with dissipative contacts and randomly distributed masses. It was shown that even

in the presence of disorder, the impulse still travels as a compact object. Sen and Manciu [18] obtained an iteratively exact solution to describe the solitary wave as a function of material parameters and an infinite set of coefficients which depend on the power law index. Xu and Hong [19] studied numerically the propagation, reflection and collision of solitary waves in the vertical granular chain under gravity. Hong and Xu [20] found different characteristics in the backscattered signal depending on the presence of light and heavy impurities in granular chain and pointed out that the difference is due to soliton confinement in the region of the light impurity of the granular chain. Manciu and Sen [21] expanded the study in [16] about the formation of secondary solitary wave formation in systems with generalized Hertz interactions. Nesterenko et al. [22] investigated the strongly nonlinear wave interaction with the interface of two granular chains under magnetically induced precompression. Anomalous reflected compression and transmitted rarefaction waves were observed. Job et al. [23] studied the reflection of solitary waves in a chain of identical elastic beads at a wall with different elastic properties numerically and experimentally. Vergara [24] studied numerically the scattering of nonlinear solitary waves from an interface created by joining two one-dimensional chains of spherical particles of different radii and masses. Dariao et al. [25] measured the propagation of strongly nonlinear solitary waves in a chain of Teflon beads experimentally. The wave speeds and profiles of solitary waves of the experimental results were in reasonable agreement with the numerical solution based on the Hertz interaction law. Fast decomposition of long initial pulse into a train of solitary waves and a speed of propagation of solitary wave well below the sound speed in air were observed in the experiment. Hong [26] proposed that a granular container having multiple interfaces with an appropriate alignment of elastic properties and masses may

play a role as an effective protector for an external impulse. Daraio et al. [27] investigated the impulse confinement and the disintegration of the shock and solitary waves in one-dimensional chains of alternating ensembles of beads with high and low elastic moduli and different masses. It was found that the trapped energy is contained within the "softer" sections of the chain and is slowly released in the form of weak and separated pulses over time. Daraio and Nesterenko [28] experimentally measured the propagation of strongly nonlinear solitary waves in a chain of polymer coated beads and showed that the chains of composite beads with a "hard" core and a "soft" coating do support the Hertzian interaction and formation of strongly nonlinear solitary waves. Daraio et al. [29] used a permanent magnet to apply static precompression to a chain of Polytetrafluoroethylene (PTFE) or stainless steel beads to demonstrate the tenability of solitary waves by adjusting the precompression. The experimental results agreed well with the long-wave approximation and numerical calculations based on the Hertz contact law. Rosas et al. [30] had explicitly demonstrated the two-wave structure in a granular chain without compression. Job et al. [31] studied the solitary wave trains in granular chain analytically, numerically and experimentally, and the results revealed that the amplitude of solitary waves decays approximately exponentially along the chain. Porter et al. [32] investigated the propagation of HNSWs in heterogeneous, periodic granular chains in which the stainless steel beads were alternated with PTFE beads periodically. The experimental results are in good agreement with the numerical simulation based on Hertzian interaction and the theoretical analysis of long-wave approximation. Sen et al. [33] reviewed the studies on solitary waves in the granular chain, introduced the theory of solitary waves in the chains of elastic beads, and discussed the possible technological applications. Khatri et al. [34] studied the coupling between HNSWs in a one-

dimensional chain of beads and linear elastic media. The experimental observations agreed well with the results from finite element analysis. Carretero-González et al. [35] proposed an extended Hertzian model to account for the dissipative effect and developed optimization methods to compute the exponents and prefactors in the extend model. The experiments on the chains consisting of beads made of different materials revealed a common dissipation exponent and a material-dependent prefactor. Porter et al. [36] expanded the work in [32] and extended the existing theory from uniform granular lattices to non-uniform ones. Theocharis et al. [37] investigated nonlinear localized modes in one-dimensional chains of compressed elastic beads with one or two light-mass impurities. Molinari and Daraio [38] studied the existence of stationary shock waves in uniform and non-uniform chains of spherical particles with Hertzian contacts. Herbold et al. [39] investigated the formation and propagation of pulses in one-dimensional chains of stainless steel cylinders alternated with PTFE spheres in linear, weakly nonlinear and strongly nonlinear regimes. Fraternali et al. [40] applied the evolutionary algorithm to study the optimal design of composite granular protectors using one-dimensional chains of beads composed of various sizes, masses, and stiffnesses. Boechler et al. [41] used experiments, theory, and numerical simulations to investigate the discrete breathers in a compressed one-dimensional diatomic granular crystal. They analyzed how a modulational instability generates discrete breathers in the weakly nonlinear regime and proved the existence of discrete breathers experimentally. Theocharis et al. [42] further studied the existence and stability of discrete breathers, and examined an unstable discrete gap breather centered on a heavy particle with a symmetric spatial energy profile and a potentially stable discrete gap breather centered on a light particle with an asymmetric spatial energy profile. Ponson et al. [43]

investigated the propagation of highly nonlinear waves in disordered granular chains composed of diatomic units of spheres that interact via Hertzian contact. Each unit was oriented in one or two possible ways, and the level of disorder in the chain is quantified by counting the number of units with the same orientation. It was found that in low-disorder chains the solitary pulse propagated with exponentially decayed amplitude and beyond a critical level of disorder the wave amplitude decayed as a power law instead. Daraio et al. [44] investigated the propagation of highly nonlinear pulses in a two-dimensional granular system that consists of a double Y-shaped guide in which different mass/elastic modulus chains of spheres were arranged. The numerical analysis agreed with the experimental results for most cases. Spadoni and Daraio [45] introduced the generation and control of compact acoustic pulses (sound bullets) by a tuable, nonlinear acoustic lens which consists of ordered arrays of granular chains. The amplitude, size of sound bullets and the focusing location can be controlled by changing the static precompression on the chains. The focusing effect was demonstrated by theory, numerical simulation and experiment. Boechler et al. [46] presented an experiment to demonstrate that the presence of a light-mass defect near a boundary in a statically compressed one-dimensional chain of particles resulted in bifurcations and a subsequent jump to quasiperiodic and chaotic states. The combination of frequency filtering effect and bifurcation could be used to achieve acoustic switching and rectification. Leonard et al. [47] studied the wave propagation in a two-dimensional square packing of uncompressed stainless steel beads excited by impulsive loadings. The solitary waves only travelled through the initially excited chains. The results from the experiment and numerical simulation were in good agreement. Boechler et al. [48] investigated the tunable vibration filtering properties of a one-dimensional diatomic granular crystal

composed of periodic arrays of three-particle unit cells which were assembled with elastic beads and cylinders that interact via Hertzian contact. The measured transfer functions of the crystals using state-space analysis and experiments were in good agreement with the theoretical dispersion relation analysis. Ngo et al. [49] studied the propagation of HNSWs in a one-dimensional chain of ellipsoidal particles. The experimental results of the propagation properties were found in good agreement with the theoretical prediction by long wavelength approximation, the numerical simulation with discrete particle model, and the finite element simulation. Spadoni et al. [50] experimentally studied the dynamic response of a nonlinear phononic crystal composed of alternating steel disks and PTFE rings under precompression. Finite element model was used to confirm the existence of a significant band gap and to reveal that some wave modes are insensitive to precompression. Yang et al. [51] studied the interaction of HNSWs propagating in granular crystals with adjacent linear elastic media. The characteristics of the reflected HNSWs such as time-of-flight, amplitude ratio were correlated to the mechanical properties and geometry of the linear media. The experimental results agreed with theoretical analysis based on the long wavelength approximation and numerical simulation based on discrete particle model.

1.2 MOTIVATION AND OBJECTIVE

The overall objective of this project is to develop a new NDE/ SHM paradigm based on the use of HNSWs, able to detect defects at early stages and/or characterize the mechanical properties of materials. On a fundamental level, the study aims at characterizing the coupling between a highly

nonlinear oscillator and linear structures. From a purely applied perspective, the project will be devoted to the validation of the fundamental studies and to the assembling of a new family of actuators and sensors, their proof-of-principle testing on fundamental NDE/SHM problems, and numerical validation.

1.3 STRUCTURE OF THE DISSERTATION

This dissertation is organized as follows. The theoretical background about HNSWs is presented in Chapter 2. The fundamental research, which includes the laser generation of HNSWs and tuning the HNSW by electromagnetical precompression, carried out in this study is presented in Chapter 3. The development of a remotely and automatically controlled HNSW-based transducer is described in Chapter 4. Then, the applications of HNSW in NDE and SHM including curing monitoring of cement, concrete, and two ton epoxy, assessment of bond condition of aluminum lap-joints, and damage detection in composite plate are presented in Chapter 5. Chapter 6 presents the preliminary study on acoustic lenses consisting of granular materials. Finally, Chapter 7 discusses some directions for future studies on applications of HNSWs.

2.0 BACKGROUND ON HIGHLY NONLINEAR SOLITARY WAVES

HNSWs are compact waves characterized by unique tunable dynamic properties. For a system consisting of a chain of spherical particles, solitary pulses can be excited by impacting one side of the chain with a particle identical (or of equal mass) to the particles composing the chain.

The theoretical prediction of stress wave propagation in a chain of identical elastic beads is given by Nesterenko [3] and has been demonstrated through quantitative experiments [5,7]. One peculiar characteristic of HNSWs is that their spatial wavelength is fixed and independent of their amplitude. In a chain of particles, the wavelength of the pulse is about five particle diameters. The amplitude and frequency, as well as the number of pulses generated in the nonlinear systems can be tuned, for example, by changing the diameter of the bead, adding static precompression to the chain of beads, changing the impact velocity and/or changing the shape of the beads.

2.1 HERTZ INTERACTION LAW

The interaction between two adjacent beads in one-dimensional chains is governed by Hertz law which was demonstrated by theoretical and experimental studies in [3-5,7]. Thus, the Hertz interaction law is first introduced.

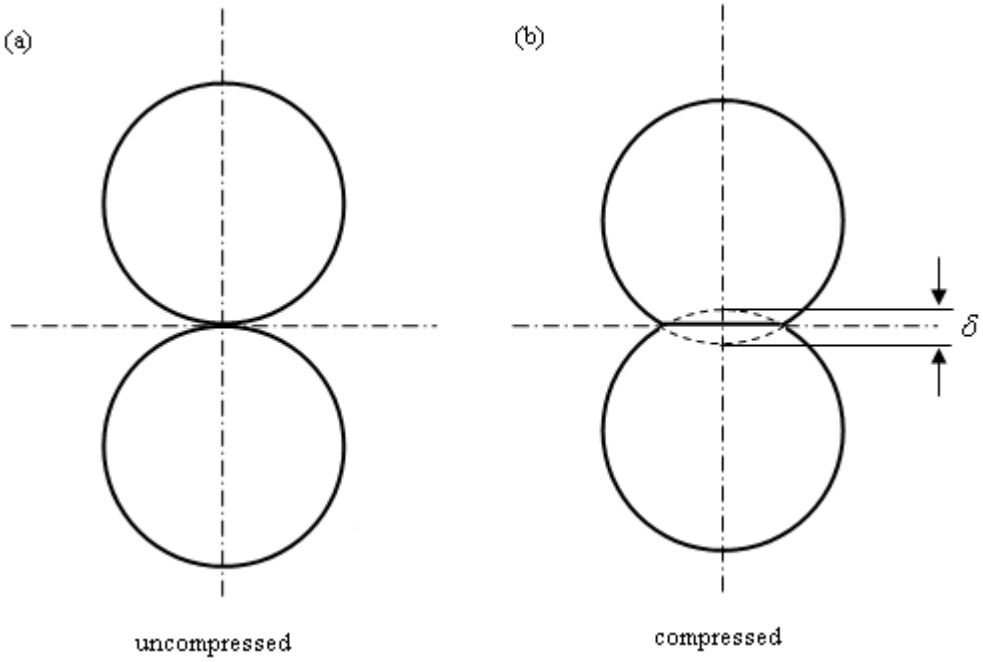

Figure 2.1. Cross-section of two spheres in contact (a) uncompressed, (b) compressed. δ is the approach of two spheres' centers

When two spheres are compressed together by a static force F, they are in contact at a small region which is not a singular point on either surface. Figure 2.1 shows the cross-section of the surfaces of two spheres near the contact region. According to the theory of elasticity [52], the radius of the contact region r is

$$r = F^{1/3}\left(\frac{DR_1R_2}{R_1+R_2}\right)^{1/3} \tag{2.1}$$

where

$$D = \frac{3}{4}\left(\frac{1-\nu_1^2}{E_1}+\frac{1-\nu_2^2}{E_2}\right) \tag{2.2}$$

and R_1, R_2, E_1, E_2, and ν_1, ν_2 are the radii, the Young's moduli, and the Poisson's ratios of the two spheres.

During the compression of between tow beads, the stress is much greater in the vicinity of the contact region than throughout the rest of the beads. The bulk of the beads act as almost undeformable bodies whereas the material in the neighborhood of the contact region acts as a nonlinear spring. The relation between the static force F exerted on the spheres and the distance of approach of their center δ is governed by Hertz's interaction law [52]:

$$F = \frac{1}{D}\left(\frac{R_1R_2}{R_1+R_2}\right)^{1/2}\delta^{3/2} \tag{2.3}$$

And the potential energy (Hertz potential) V is

$$V = \frac{2}{5D}\left(\frac{R_1R_2}{R_1+R_2}\right)^{1/2}\delta^{5/2} \tag{2.4}$$

For a chain composed of identical beads, Equation (2.3) becomes

$$F = A_1\delta^{3/2} \tag{2.5}$$

The material dependant constant

$$A_1 = \frac{E\sqrt{2R}}{3(1-\nu^2)} \tag{2.6}$$

where R is the radius of the beads in the chain, E and ν are the Young's modulus and the Poisson's ratio of the material.

It should be pointed out that the Hertz law is formulated for static problems, in order to use it for solving dynamic problems, the following conditions need to be satisfied. (1) the maximum stress achieved in the vicinity of the contact must be less than the elastic limit; (2) the sizes of the contact surface must be much smaller than the radii of curvature of each particle; (3) the characteristic times of the problem τ are much longer than the oscillation period of the basic shape for the elastic sphere T [3-4]:

$$\tau >> T \approx 2.5\frac{R}{c_1} \tag{2.7}$$

where c_1 is the velocity of bulk wave in the material of the interacting bead.

2.2 LONG WAVELENGTH APPROXIMATION

In this section, part of long wavelength approximation theory developed by Nesterenko [3-4], which is related to the studies in this dissertation, is reviewed and summarized.

Let consider a one-dimensional chain of N identical beads with radius R and mass m (Figure 2.2). Taking the precompression into account, let us assume that the chain is subject to a constant precompression force F_0, which is applied to the chain's both ends and securing the

initial approach between the centers of adjacent beads δ_0. As a result of Newton's laws of motion,

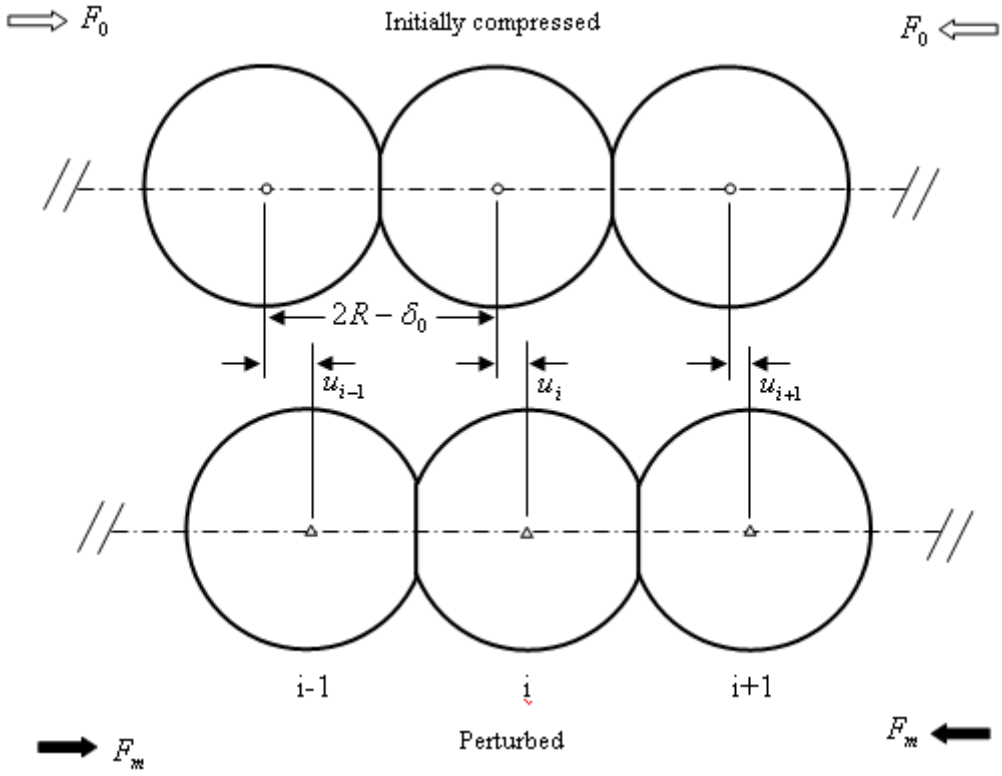

Figure 2.2. One-dimensional chain initially compressed by a static force F_0, small circles are the initial positions of beads and small triangles are the beads' positions after perturbation, F_m denotes dynamic contact force

$$\ddot{u}_i = A(\delta_0 - u_i + u_{i-1})^{3/2} - A(\delta_0 - u_{i+1} + u_i)^{3/2} \quad , \quad 2 \le i \le N-1 \tag{2.8}$$

where u_i denotes the displacement of i[th] particle from its equilibrium position in the initially compressed chain. For convenience, the coefficient A_1 in Equation (2.6) is normalized by the mass of beads m to get the constant A in Equation (2.8), $A = A_1 / m$. For the beads at both ends, when $i=1$, $\ddot{u}_i = A\delta_0^{3/2} - A(\delta_0 - u_{i+1} + u_1)^{3/2}$, when $i = N$, $\ddot{u}_i = A(\delta_0 - u_i + u_{i-1})^{3/2} - A\delta_0^{3/2}$.

When the chain is initially “strongly” compressed, the dynamic deformation is much smaller than the initial deformation:

$$\frac{|u_{i-1} - u_i|}{\delta_0} << 1 \tag{2.9}$$

In the anharmonic approximation, Equation (2.8) can be written as follows:

$$\ddot{u}_i = \alpha(u_{i+1} - 2u_i + u_{i-1}) + \beta(u_{i+1} - 2u_i + u_{i-1})(u_{i-1} - u_{i+1}) \quad for \quad 2 \le i \le N-1 \tag{2.10}$$

where

$$\alpha = \frac{3}{2} A\delta_0^{1/2} \quad , \quad \beta = \frac{3}{8} A\delta_0^{-1/2} \tag{2.11}$$

In the long wavelength approximation (L > a = 2R, where a is the diameter of the beads and L is a characteristic spatial wavelength of the wave), the following equation can be obtained from Equation (2.10):

$$u_{tt} = c_0^2 u_{xx} + 2c_0\gamma u_{xxxx} - \sigma u_x u_{xx} \tag{2.12}$$

in which,

$$c_0^2 = A\delta_0^{1/2} 6R^2 \quad , \quad \gamma = \frac{c_0 R^2}{6} \quad , \quad \sigma = \frac{c_0^2 R}{\delta_0} \tag{2.13}$$

All terms of the order $\frac{c_0^2}{L^2}\left[\left(\frac{a}{L}\right)^4 + \left(\frac{a}{L}\right)^3\left(\frac{u}{\delta_0}\right)\right]$ and higher were omitted in deriving Equation (2.12). The solution of Equation (2.12) satisfies the Korteweg-de Vries (KdV) equation and it will not be discussed here because it is beyond the scope of this study. When the chain is initially “weakly” compressed,

$$\frac{|u_{i+1}-u_i|}{\delta_0} \geq 1 \tag{2.14}$$

only one equation corresponding to the long wavelength approximation can be obtained from Equation (2.8) for the discrete chain. The Equation (2.8) can be replaced by Taylor series expansions according to the small parameter *a/L*. The wave equation in this case is

$$u_{tt} = c^2\left\{\frac{3}{2}(-u_x)^{1/2}u_{xx} + \frac{a^2}{8}(-u_x)^{1/2}u_{xxxx} - \frac{a^2}{8}\frac{u_{xx}u_{xxxx}}{(-u_x)^{1/2}} - \frac{a^2}{64}\frac{(u_{xx})^3}{(-u_x)^{3/2}}\right\} \tag{2.15}$$

where

$$-u_x > 0 \quad , \quad c^2 = \frac{2E}{\pi\rho(1-\nu^2)} \tag{2.16}$$

and ρ is the density of particle material. The wave equation can be written in divergent form:

$$u_{tt} = -c^2\left\{(-u_x)^{3/2} + \frac{a^2}{10}\left[(-u_x)^{1/4}\left((-u_x)^{5/4}\right)_{xx}\right]\right\}_x \tag{2.17}$$

$$\xi_{tt} = c^2\left\{\xi^{3/2} + \frac{a^2}{10}\left[\xi^{1/4}(\xi^{5/4})_{xx}\right]\right\}_{xx} \tag{2.18}$$

where the strains $\xi = -u_x > 0$.

The stationary solutions for Equations (2.17) and (2.18) are summarized as follows:

The speed of solitary wave is

$$V_s = \frac{c}{\xi_m - \xi_0}\left[\frac{2}{5}(3\xi_0^{5/2} + 2\xi_m^{5/2} - 5\xi_0^{3/2}\xi_m\right]^{1/2}$$
$$= \frac{c_0}{\xi_r - 1}\left[\frac{4}{15}(3 + 2\xi_r^{5/2} - 5\xi_r)\right]^{1/2} \tag{2.19}$$
$$= 0.9314\left[\frac{4E^2F_0}{a^2\rho^3(1-\nu^2)^2}\right]^{1/6}\frac{1}{(f_r^{2/3}-1)}\left[\frac{4}{15}(3 + 2\xi_r^{5/2} - 5\xi_r)\right]^{1/2}$$

where ξ_m is the maximum strain, ξ_0 is the initial strain caused by precompression F_0, F_m is the maximum dynamic contact force, f_r is the force ratio, $f_r = F_m / F_0$. c_0 is the sound speed in a chain with precompression F_0 and force ratio $f_r = 1$:

$$c_0 = \left(\frac{3}{2}\right)^{1/2} c\xi_0^{1/4} = 0.9314\left[\frac{2E}{a\rho^{3/2}(1-\nu^2)}\right]^{1/3} F_0^{1/6} \tag{2.20}$$

When $F_0 = 0$, called "sonic vacuum", f_r or ξ_r is infinite, Equation (2.19) reduces to

$$V_s = \frac{2}{\sqrt{5}} c\xi_m^{1/4} = 0.6802\left[\frac{2E}{a\rho^{3/2}(1-\nu^2)}\right]^{1/3} F_m^{1/6} \tag{2.21}$$

The concept "sonic vacuum" is used for strongly nonlinear systems without a linear part in the force displacement relation between particles and this type of systems do not support the propagation of classical sound waves without initial precompression. The strain in this case is:

$$\xi = \left(\frac{5V_s^2}{4c^2}\right)\cos^4\left(\frac{\sqrt{10}}{5a}x\right) \tag{2.22}$$

The solitary wave in sonic vacuum can be approximated by one hump of cos^4 function. The finite wavelength of stationary solution of solitary wave is

$$L = \frac{5\pi}{\sqrt{10}} a \approx 5a \tag{2.23}$$

3.0 FUNDAMENTAL RESEARCH ON HNSWS

In this chapter the results from some fundamental researches carried out in this study are presented. In particular, the capability to generate HNSWs by means of laser pulses is demonstrated for the first time. In addition, by devising an electromagnet we show the tunability of HNSWs by varying static precompression in a chain of particles made of low-carbon steel beads.

3.1 LASER-BASED EXCITATION OF HNSWS

Single HNSWs are commonly induced in one-dimensional granular crystals by mechanically impacting the first bead of the chain with a striker having the same mass of the particles composing the chain. In this study we experimentally investigated the use of short duration (~ 8 nanoseconds) laser pulses to induce HNSWs in a one-dimensional chain of stainless steel spheres. We analyzed the formation and propagation properties of the solitary pulses using sensors placed in selected particles of the chain. The results were compared with the theoretical prediction obtained from the long wavelength approximation [3-4,25,29].

3.1.1 Mechanism of laser generation of HNSWs

Laser generation of ultrasound was first demonstrated by White [53], since then lasers were widely used to generate ultrasound in solids, liquids, and gases [54-55]. In this study, the laser pulse was used to generate HNSWs in a chain of stainless steel beads. The mechanism of the laser generation of HNSWs in a chain of stainless steel beads is briefly described here. The transfer of energy from a nanosecond optical pulse to a mechanical wave can occur by thermoelastic transduction or by ablation, depending on the intensity of the laser pulses and the surface properties of the illuminated targets. A thermoelastic stress is created when the laser energy density is low, such that there is no material ablation or plasma formation on the surface of the object. In this regime, shear mechanical stresses are generated by the thermal expansion due to the sharp increase of the surface's temperature. Laser ablation is generated when the laser's power density is high, or when the surface of the illuminated medium is covered with a film of water or gel. In this case the rapid vaporization (ablation) of the film at the surface, or the melting of a small portion of the medium's surface, induces high reaction pressures that can be considered similar to normal stress loading [56-59]. Picosecond light pulses have also been used to generate very short stress waves in films of different materials via thermal expansion [60].

The use of pulsed-laser excitations to trigger the formation of HNSWs has practical advantages such as non-contact coupling between the laser and the chain of particles. This non-contact excitation could be useful in applications where a remote placement of equipment or a complex geometrical arrangement of the chains is required (e.g. in NDE of materials), or for triggering multiple solitary waves in parallel chains (e.g. to generate sound bullets [45]).

In our experiments, we rely on the ablation of a controlled amount of water deposited with a syringe on the surface of the first bead to generate mechanical stresses in the chain of particles. In order to estimate the amount of mechanical stress transferred from the laser to the chain, we assume that the energy transfer occurs only though the ablation of the water droplet deposited on the first particle of the chain, and we describe the energy transfer using the equations that govern the ablation of water on a flat metallic surface [55]. The incident power density I of the pulsed laser is given by:

$$I = \frac{E_L}{A\Delta t} \tag{3.1}$$

where E_L is the energy of the laser, Δt is the pulse duration, and A is the area of the pulse. The ablation of material from the surface produces a net stress in reaction against the sample [55], in the direction of the chain's axis. This stress can be calculated from the rate of change of momentum, i.e:

$$\sigma = \frac{I_a^2}{\rho_w [L + C(T_v - T_0)]^2} \tag{3.2}$$

In Equation (3.2), I_a is the absorbed power density, ρ_w is the density of water, L is the water's latent heat of vaporization, C is the thermal capacity of water, T_v is the vaporization temperature of water, and T_0 is the ambient temperature (293 K) at which the experiment was conducted. For a polished mild steel irradiated by a 1064 nm laser pulse, the reflectivity coefficient R is equal to 0.63 [55], the absorbed power density is equal to:

$$I_a = I(1-R) \tag{3.3}$$

The effective force F generated by ablating the water droplet on the metallic surface is equal to:

$$F = \sigma \cdot A \tag{3.4}$$

This force is analogous to the dynamic contact force generated by a striker impacting the top particle of the chain. If we assume that the amplitude of the pulse energy is constant over its 8 ns duration, then mechanical impulse J transferred to the chain of particle is given by:

$$J = F \cdot \Delta t \tag{3.5}$$

Table 3.1. Parameters used to compute the net stress force generated by the ablation of a drop of water on the flat surface of polished mild steel.

Parameter	Value	Unit
E_L	150×10^{-3}	J
Pulse diameter	0.5×10^{-3}	m
Δt	8×10^{-9}	Sec
ρ_w	1000	Kg / m^3
L	2260×10^3	J / kg
C	4200	J / kg K
T_v	373	K

The impulse J is equivalent to the impulse generated by a striker bead having same mass of the particle chains and falling from an effective height h_{eq}. If we assume the values shown in Table 3.1, the impulse of the laser is equivalent to a falling mass of 0.45 g from an effective height h_{eq}= *21* mm. This estimate is in agreement with experimental measurements performed on the same chain of particles excited by a mechanical striker released from different heights, which will be described in Section 3.2. In the experiment in Section 3.2, it was found that the average maximum dynamic contact force measured between the 7^{th} and 12^{th} sensor beads when the striker was released from 20 mm was equal to 21.44 N. As it will be shown in the Subsection 3.1.3, in the present study the average maximum dynamic contact force measured between the 9^{th} and 14^{th} sensor beads was equal 10.54 N when the laser pulse energy was 150 mJ. It is important to mention that the estimate of the effective drop height does not take into account the presence of losses and attenuation in the system, and it is assumed that the laser pulse intensity is constant in time (a better approximation would be obtained considering a Gaussian-like pulse). In addition, the diameter of the laser pulse plays an important role: for example, a 1 mm pulse diameter yields a h_{eq} = 1.4 mm.

3.1.2 Experimental setup

In our experiments, one-dimensional granular crystals were assembled by aligning twenty stainless steel balls (Mc-Master Carr - Multipurpose Stainless Steel, Type 302) inside a vertical Teflon tube having inner diameter equal to 4.8 mm. The diameter of each sphere was equal to 4.76 mm and the mass was 0.45 g. Two piezo-gauges made from lead zirconate titanate (square

plates 0.27 mm thick and 2 mm side) with nickel-plated electrodes and custom micro-miniature wiring were embedded inside two of the steel particles. The assembling and calibration of the instrumented particles was similar to that described in [3,25,29], and the calibration procedures

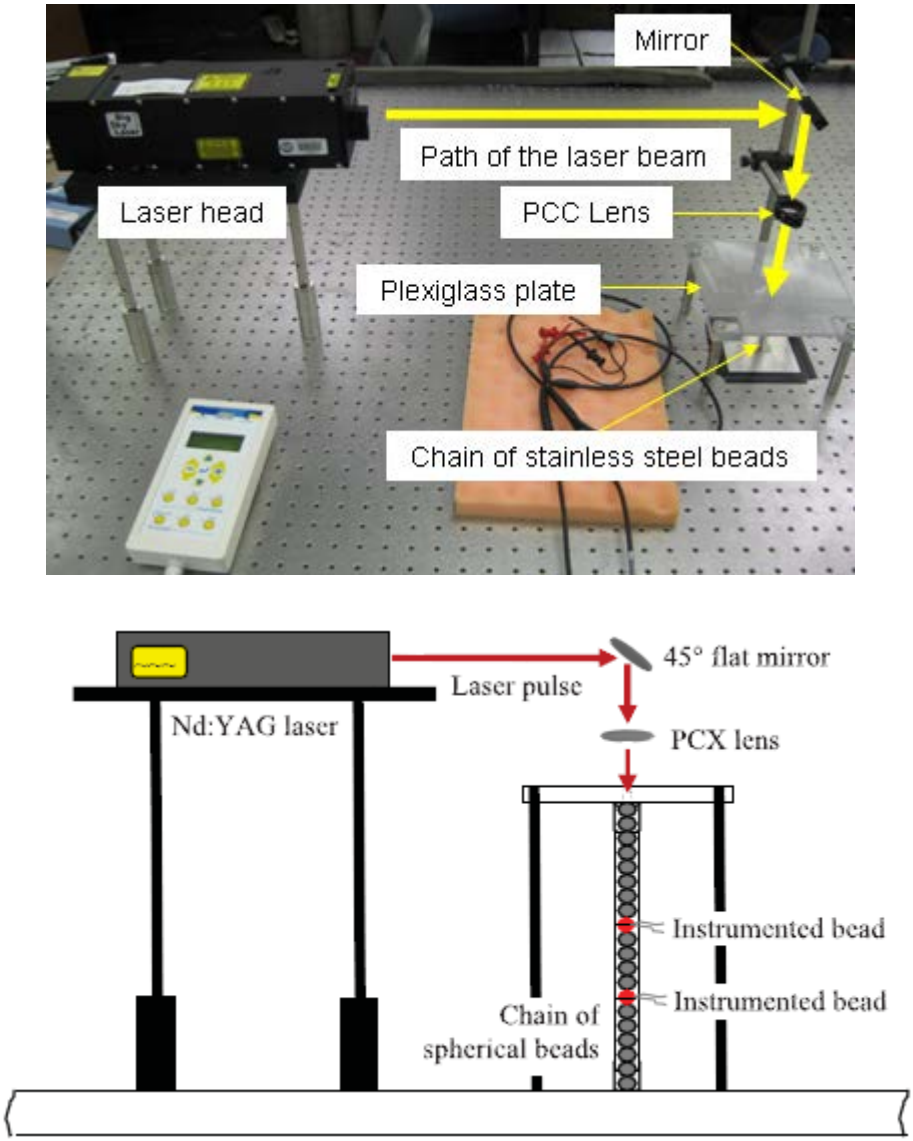

Figure 3.1. Experiment setup of observation of HNSWs propagating in a chain of steel beads (Actuator) excited by the laser pulse

will be described in Appendix A. The sensor beads were positioned along the chain at the 9th and 14th position from the top, and connected to an oscilloscope. Signals were sampled at 10 MHz. To compare the experimental results with the theoretical predictions, the forces measured by the instrumented bead ($F_{m,e}$) were related to the dynamic contact forces (F_m) as described in [25].

A 10 Hz repetition rate Nd:YAG pulse laser operating at 1064 nm wavelength was used to excite stress waves in the chain of particles. The laser beam output diameter was equal to 7 mm. Through conventional optics (a 45 degrees high energy Nd:YAG mirror and a plano-convex (PCX) UV fused silica lens, 25.4 mm diameter, and 100 mm focal length), a ~1 mm diameter beam, as measured using a laser alignment paper, was directed on the surface of the first particle of the chain. The laser was operated in single-shot mode. To apply variable amounts of static precompression on the chain of particles, we placed above the chain a polycarbonate sheet, loaded with variable balanced masses. To allow direct interaction of the laser beam with the first particle in the chain, a 3 mm diameter hole was drilled in the center of the sheet. The photo and schematic diagram of the experimental setup are presented in Figure 3.1.

3.1.3 Results and discussion

We investigated the effects of the beam intensity and of the precompression on the characteristics of the solitary waves. To determine the effects of the energy we varied the laser's energy output between 120 mJ and 190 mJ with 10 mJ increments. As the diameter of the beam impinging the top particle of the chain was equal to 1 mm the energies can be straightforwardly related to the laser intensities expressed in 15.28 J/cm^2 to 24.17 J/cm^2 with 1.27 J/cm^2

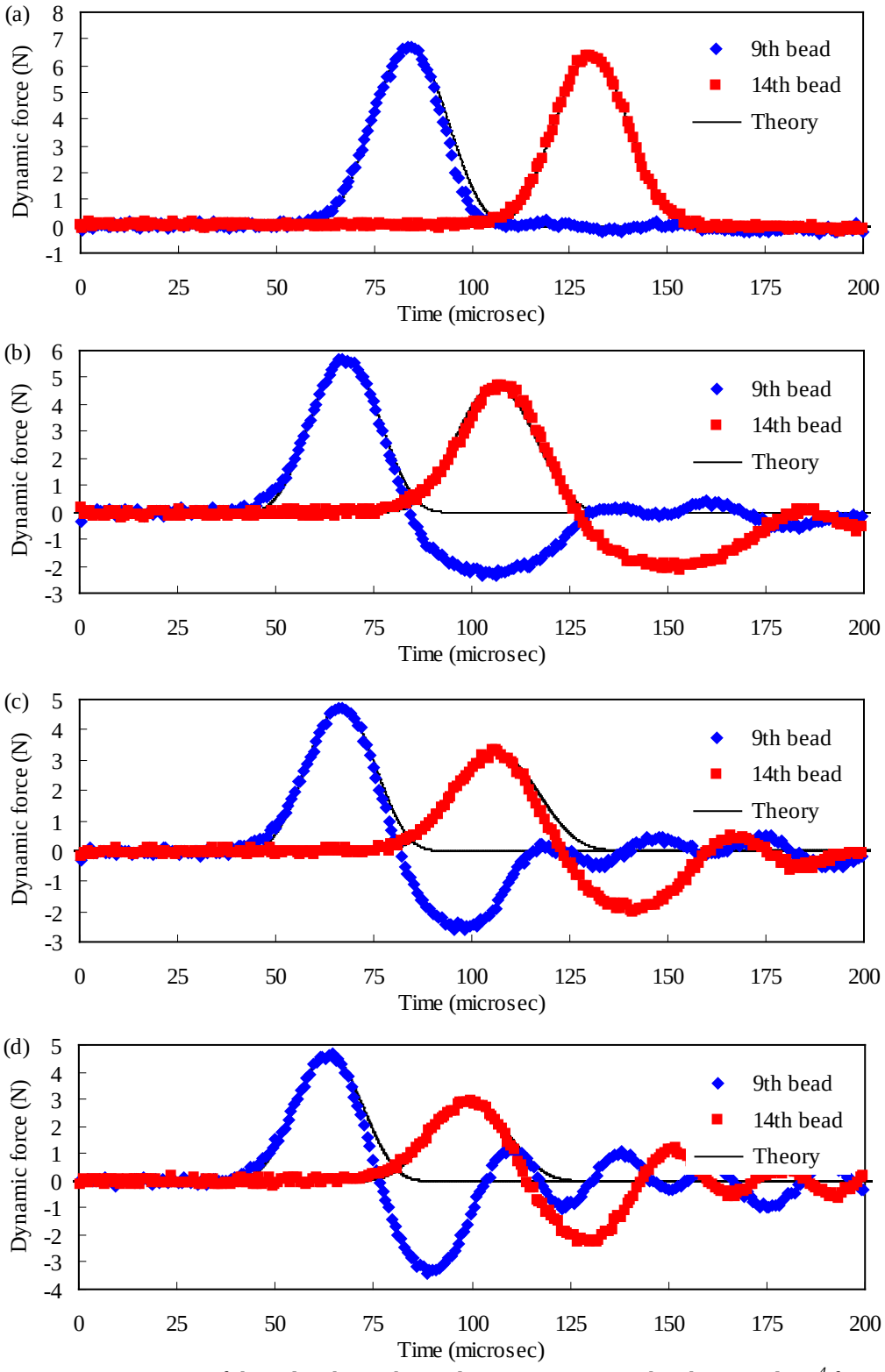

Figure 3.2. Comparison of the pulse shape obtained in experiments with a theoretical cos^4 function

increments. To study the effect of precompression, we used four different values of precompressive force: 0.049 N, 2.305 N, 3.384 N, and 5.150 N. These static preloads were applied placing balanced masses on the polycarbonate sheet. The values include the self-weight of the top eleven beads.

Typical time waveforms recorded by the two instrumented particles in the chain at four different values of precompression and 160 mJ laser energy (equivalent to an energy density of 20.37 J/cm^2) are shown in Figure 3.2. For comparison, a cos^4 function (Equation. (2.22)) [3] was superimposed to the measured waveforms. As expected, at low values of precompressive force (Figure 3.2(a)) the shape of the experimental pulse is in excellent agreement with predictions from the highly nonlinear theory. However, with increasing amount of precompression with respect to the amplitude of the dynamic force $F_{m,e}$, the response of the chain shifts from the highly nonlinear regime towards the weakly nonlinear and linear response. This is evident from the appearance of an increasingly large tensile part of the pulse in Figure 3.2(b,c,d) and from the presence of additional oscillations following the leading pulse.

The speed of the HNSW was calculated by detecting the arrival time of the pulse's peak in the instrumented beads and knowing their relative distance in the chain. We compared this speed with the amplitude of the traveling pulses. Figure 3.3 shows the HNSW's speed as a function of the dynamic contact force. The experimental values are shown by solid dots and the theoretical curves are represented by solid lines. In Figure 3.3(a), the vertical error bars are the results of possible inaccuracy on the estimation of the peak's arrival time and on the measurement of the travel distance between the two piezosensors. In Figure 3.3(b), the horizontal error bars are the results of accuracy of the sensors' calibration coefficients. To ensure

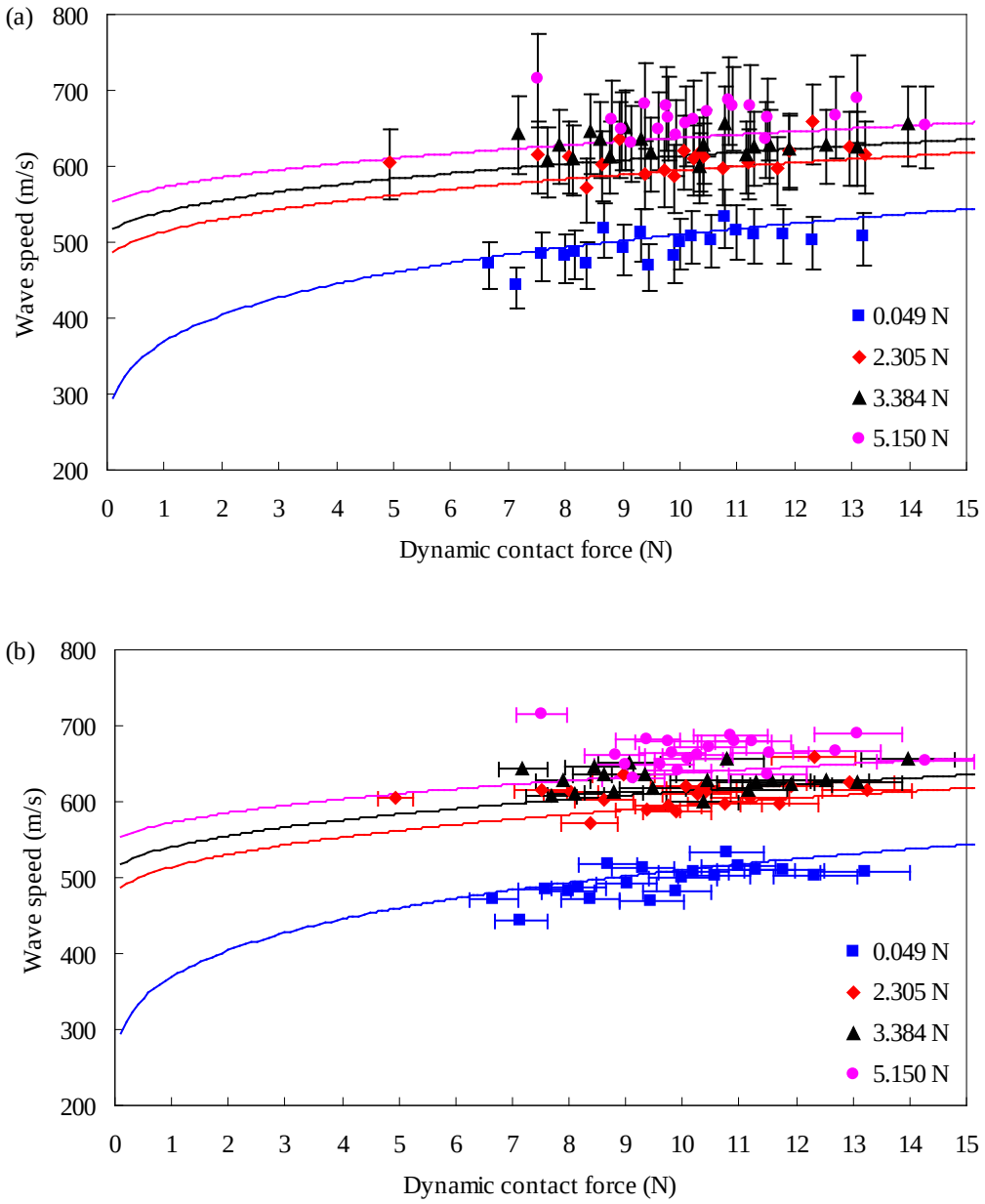

Figure 3.3. Wave speed as a function of the dynamic contact force at different amounts of static precompression

repeatability of the results, each measurement at a given laser pulse energy was repeated ten times, for a total of 320 data points collected. For the sake of clarity only a random subset of data

out of 320 measurements is presented. The experimental wave velocities associated with the four levels of precompression were compared to the corresponding theoretical curves obtained from Equation (2.19). The agreement between the experimental data and the theoretical prediction confirms that short duration laser pulses can generate HNSWs.

The effect of the laser intensity on the characteristics of the propagating waves is shown in Figure 3.4. Variations in the dynamic force amplitude as a function of the laser energy used to excite the pulses are shown in Figure 3.4, for a value of static preload equal to 0.049 N. It is evident that the solitary wave amplitude increases non-monotonically with increased laser energy. For example, a decrease of the contact force is evident between 19.10 J/cm^2 and 20.37 J/cm^2 for all four pre-compression forces tested. This suggests that the characteristics of the beam are nonlinearly proportional to the laser energy output. The vertical error bars reported in Figure 3.4 represent the standard deviation associated with the ten measurements taken at each energy level. The scatter of the data is likely associated with the variable impulse generated during the water ablation. Although great care was taken in depositing the same amount of water at each measurement, variation in the liquid coating thickness on the particle might have occurred.

We also examined variations of the solitary wave length as a function of the applied precompression and the amplitude of the traveling pulses. Experimental data, in agreement with theoretical prediction from the long wavelength approximation [3], showed that the solitary wave length does not change significantly (with a constant spatial duration of the leading pulses always measured ~5 particles diameters).

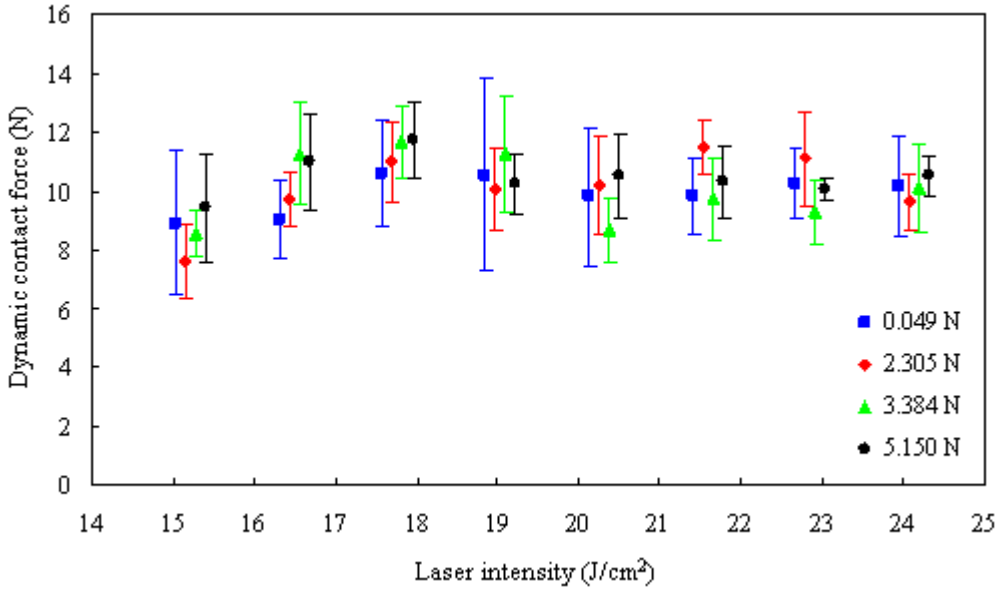

Figure 3.4. The variation of the dynamic contact force as a function of the laser energy magnitude for four different levels of static precompression

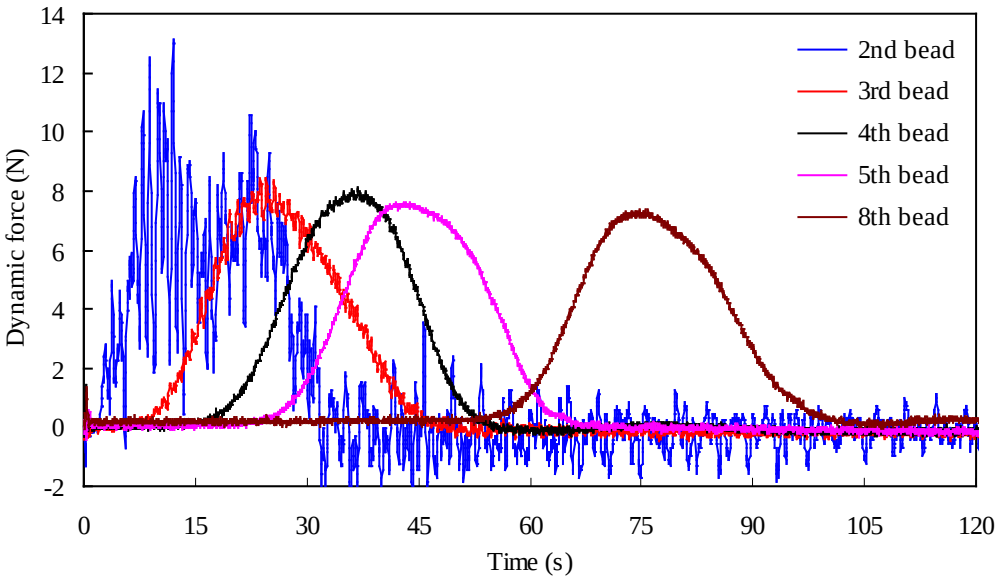

Figure 3.5. Evolution of the traveling wave in the chain of stainless-steel beads excited by the laser pulse

Then, we studied the initial formation and propagation of the solitary waves in the vicinity of the laser excitation. For these experiments, the position of the instrumented beads in the chain was changed systematically, to allow the visualization of the pulse shape evolution in the vicinity of the excitation site. Figure 3.5 shows the signals recorded by the sensor bead placed in the 2^{nd} - 5^{th} and 8^{th} position from the top. The shape of the signals varied dramatically in the immediate vicinity of the excitation source, and the formation of the solitary wave becomes evident after ~4 particles from the excitation point. The high frequency components visible at the 2^{nd} and 3^{rd} bead are related to the ultrasonic bulk waves confined inside the particles, traveling at ~5.8 km/s.

Finally, we compared the stress waves in a single steel bead excited by another identical steel bead striker and by the laser pulse. The sensor beads are put on top of an Aluminum plate which is big enough to avoid the reflection at boundaries of the plate rather than the interface between the sensor bead and the plate. Both the mechanical striker and the laser pulse were used to generate stress waves in the sensor bead. The wave propagating in the steel sensor bead by two different excitation methods are shown in Figure 3.6.

Because the mechanisms of excitation of stress waves are different, the waveforms, as shown in Figure 3.6(a) and Figure 3.6(c), are completely different. The duration of the laser pulse is only 8 ns, which is much shorter than the contact time between two beads which is on the order of tens of microseconds. Furthermore, because the duration of the laser pulse is much smaller than the time needed by a bulk longitudinal acoustic wave to travel across the diameter of the sensor bead, which is around 1 μs for the steel bead with a diameter of 4.76 mm, the largest peak occurred at the time when the stress wave arrived at the middle of the sensor; but for

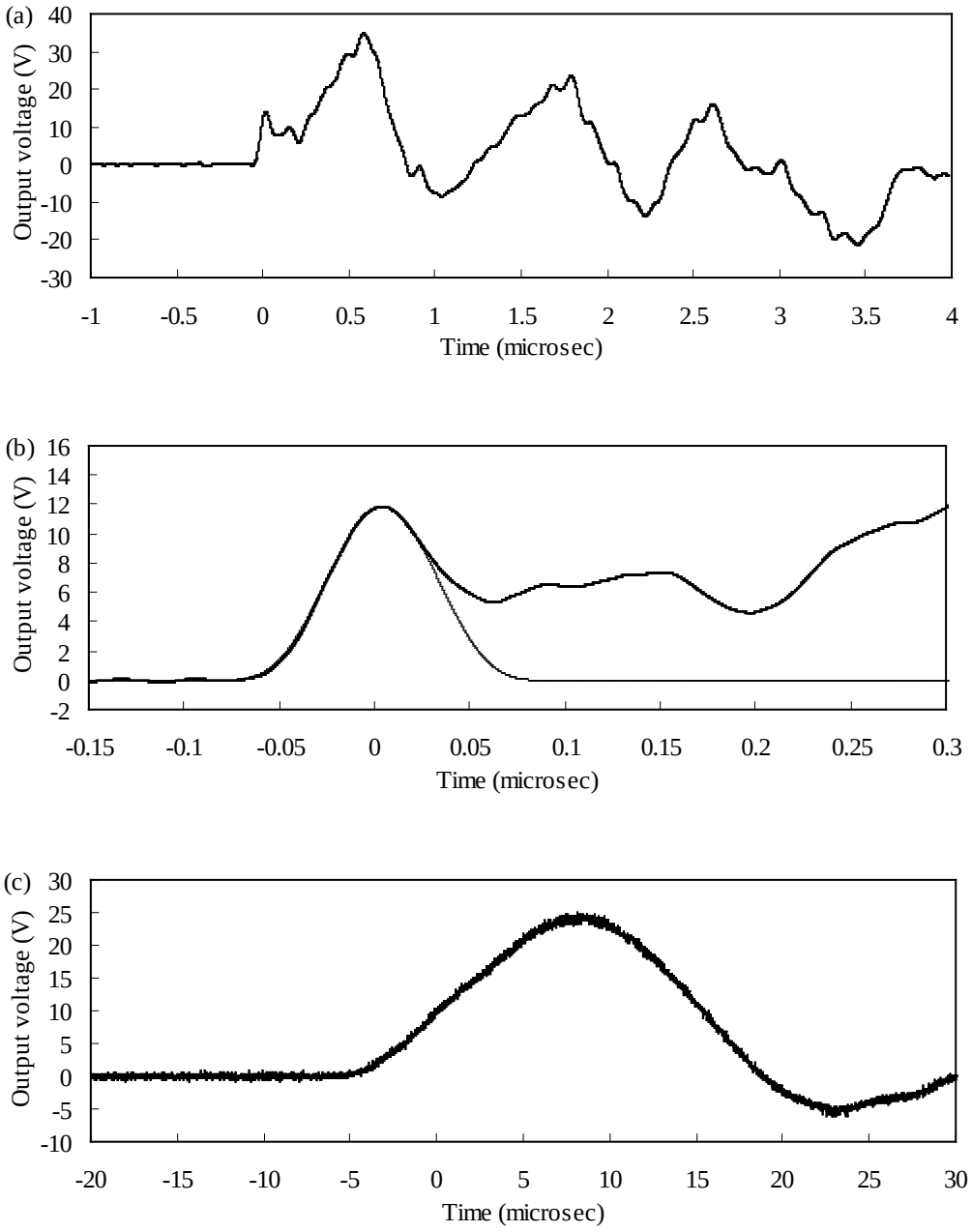

Figure 3.6. Comparison of the wave propagation in the first bead excited by (a) laser pulse, (b) laser pulse, zoom-in, (c) mechanical striker

the mechanical striker, the contact time between two beads is much greater than 1 μs, the time when the largest peak is reached mainly depends on the contact time between the striker and the sensor bead. It is interesting that as shown in Figure 3.6(b) the first peak generated by the laser pulse can be also fitted very well by a curve with the form of $V = \cos^4(\omega t + \varphi)$.

3.1.4 Conclusions

In this section we demonstrated that short duration pulsed laser beams could be used for the remote generation of highly nonlinear solitary waves and oscillatory signals in chains of spherical particles with variable precompression. The evolution of the excited pulse shape within the chain was studied experimentally, showing a rapid formation of a stationary wave after the 4^{th} particle from the excitation site. The experimentally measured dependence of the solitary wave velocity on the pulse amplitude was found in excellent agreement with the theoretical predictions for all precompression levels tested. The paper also presents a simplified model that predicts the amount of dynamical contact force that can be generated in a chain of particle using a pulsed laser. This model can be used to estimate the mechanical pulse transferred to the granular system. This laser-based non-contact method for nonlinear solitary waves generation could be employed in different engineering applications.

3.2 EFFECT OF ELECTROMAGNETIC PRECOMPRESSION

The tunability of the HNSWs in one-dimensional granular systems was reported earlier experimentally by means of a contact static force against a chain of particles, which had the disadvantage of changing the boundary conditions [7] and a permanent circular magnet to induce a single predefined static force [29].

In this section, the results of an experimental study on the effect of electromagnetically induced precompressive force on the amplitude, speed, and duration of HNSWs are presented. Changing the electrical current passing through a solenoid wrapped around the chain varies the static precompression applied to the chain. The dynamic force magnitude is adjusted by changing the velocity of a striker impinging the top bead of the chain. The experiment results agree well with the theory derived from the long wavelength approximation. The ability to use an electromagnet to tune the solitary wave propagating in a chain of ferromagnetic beads is demonstrated. This configuration allows the creation of controlled electromagnetical static precompression force spanning from 0 to 2 N that can be used to tune some of the HNSW's properties and doesn't change the boundary conditions used in the numerical model.

3.2.1 Mechanisim

Here we present a study on the formation and propagation of HNSWs in a chain of general purpose low-carbon steel beads tuned by electromagnetically induced forces. We design and utilize an electromagnet composed of a metallic wire wrapped around our highly nonlinear

granular chain to generate a magnetic field capable of applying a variable precompressive force. As it is well known, the strength of the magnetic field generated by an electromagnet is proportional to the amount of current passed through the conductive wire [61]:

$$B = \frac{NI\mu}{L} \tag{3.6}$$

where N is the number of turns of wire on the electromagnet; I is the current in the winding wire; μ is the permeability of the electromagnet core material; and L is the total length of the magnetic field path.

3.2.2 Experimental setup

One-dimensional granular crystals were assembled by filling a PTFE tube (inner diameter 5 mm) with a chain of 20 general-purpose low-carbon steel beads having a diameter a=4.76 mm and mass m=0.45 g. Two sensor beads with embedded piezogauges (same as ones used in Subsection 3.1.2) were positioned inside the chain at the 7^{th} and 12^{th} position from the top.

To apply an electromagnetically induced pre-compressive force, part of the PTFE tube was enwound with 132 m long AWG24 magnetic wire. This coil has an electric resistance of 11.1 ohm. The length of the coil was L=23.8 mm, which is 5 times the diameter of the steel beads. Another steel bead, identical to the beads in the chain, was used as the striker.

A BK PRECISION Model 1672 Triple Output Power Supply was used to apply DC Voltage/Current to the coil. The power supply has two variable outputs (0-32V/0-3A), which can work independently, in series tracking, or in parallel mode. In this experiment, only one output

was used. Depending on the load condition, the power supply can work either in Control Voltage (CV) or in Control Current (CC) mode. Because the electrical resistance of the coil depends on the coil temperature, the CC mode was used to keep the current constant for each precompression value.

The PZTs were connected to an oscilloscope (LeCroy WaveRunner 44Xi). Signals were sampled at 10MHz rate. The beads between the two sensor beads were placed in the center of the coil. Figure 3.7 shows the experimental setup adopted in this study.

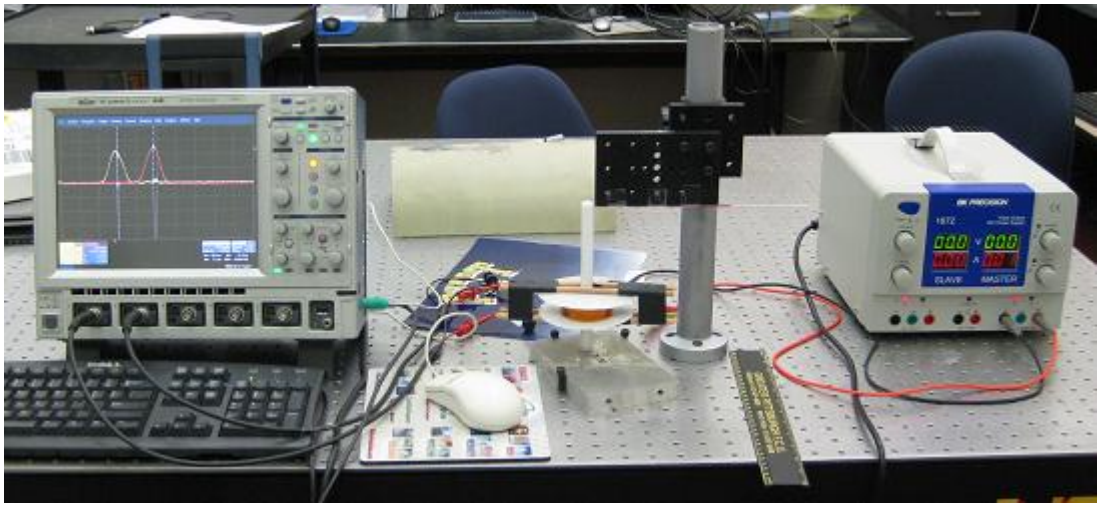

Figure 3.7. Experimental setup for testing the HNSWs in a one-dimensional chain with the addition of an electromagnetically induced precompression

Dropping a striker particle from different heights on the top particle of the chain excited solitary waves with different amplitudes. Experiments were conducted by selecting four different heights of striker drops: namely 10 mm, 20 mm, 35 mm, and 60 mm.

The electromagnetically induced precompression between the two PZTs is considered to be uniform. As such, Equation (2.19) and Equation (2.21) can be used as a benchmark

comparison. To relate the maximum value of the dynamic force $F_{m,e}$, measured by the embedded PZT, and the value of the maximum contact force between neighboring beads F_m, present in the Equation (2.19) and Equation (2.21) for solitary wave speed, the coefficient β found numerically in reference [29] was used:

$$F_m = \beta F_{m,e} + F_0 \tag{3.7}$$

3.2.3 Results and discussion

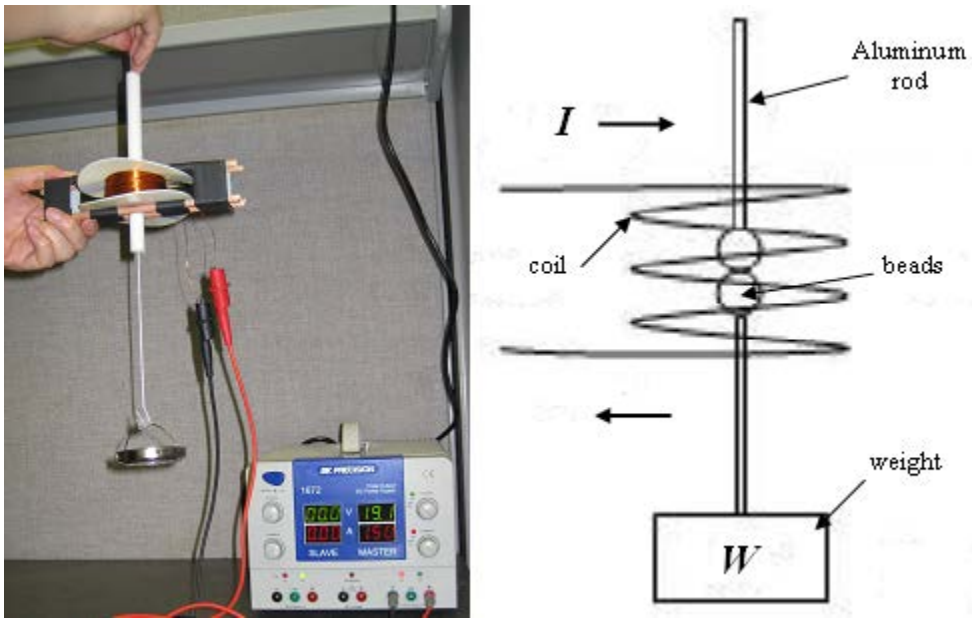

Figure 3.8. Photo and schematic diagram of the setup for measuring the precompression induced by the electromagnet

To apply a variable static precompression to the system we varied the current passing through the solenoid wrapped around the chain from 0 to 2 A, in incremental steps of 0.25 A. This relation was empirically obtained by measuring the weight that the electromagnet was able to lift

at a given value of the current. The setup for measuring the pre-compressive force generated by the electromagnet is shown in Figure 3.8.

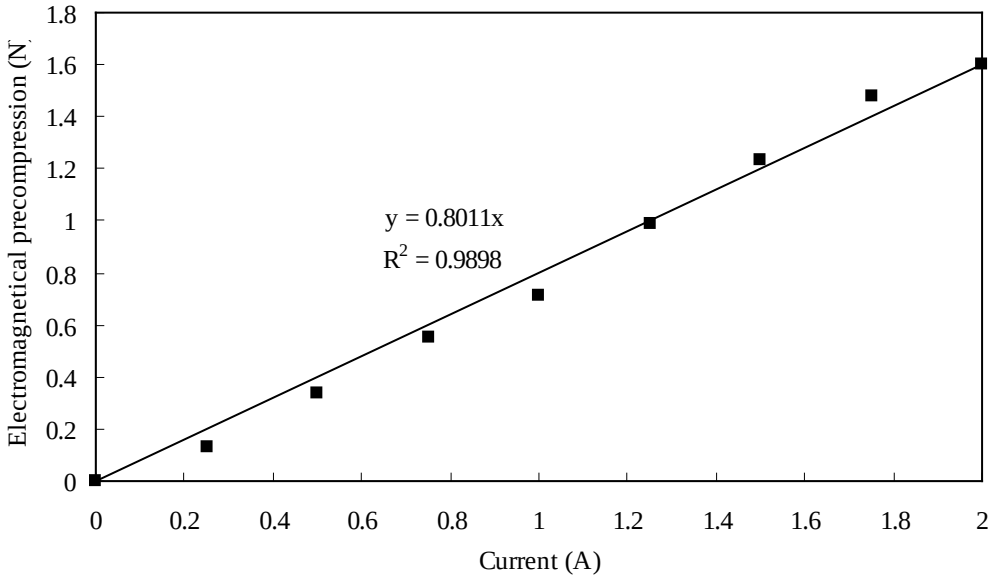

Figure 3.9. Electromagnetically induced pre-compression force as a function of the applied current

After applying electric current, the electromagnetic force was used to lift a plate which carried several weights and the sum of the weights was increased gradually. The maximum value of the sum of weights that can be lifted was recorded for each value of current and it equals to the electromagnetically induced precompression. The relation between the current and the induced precompression is shown in Figure 3.9.

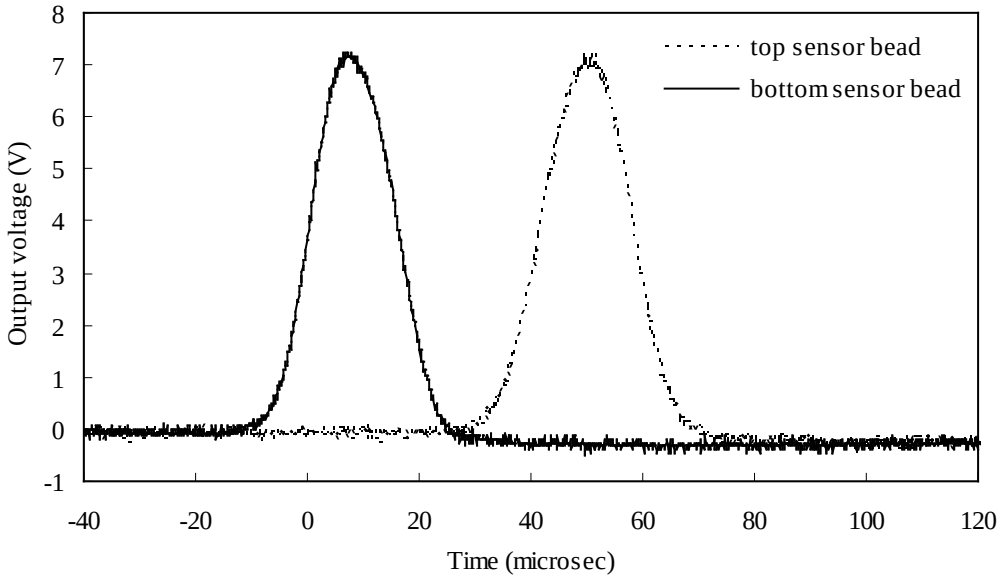

Figure 3.10. Typical HNSWs pulses obtained in the experiment

A typical waveform obtained in this experiment is shown in Figure 3.10 (the precompression is 0.04 N and the height from which the striker was released is 10 mm). Note that the signals are reported in volts, before the sensors' calibration, and present therefore no visible amplitude difference.

The solitary wave speed of the pulses traveling through the chain was easily determined by dividing the physical distance between the two PZTs (five particles' diameters) for the temporal distance between the two pulses' peaks.

When the current applied was 0 A the precompression in the chain was the result of the gravitational preload of the beads (since the chain was oriented vertically). In this study we estimated the gravitational static precompression value to be 0.04 N. Such a value was obtained by summing the weight of the top nine beads in the chain. When an electrical current was added

to the solenoid, the total pre-compressive force included the contribution of the magnetic attraction generated by the electromagnet.

For instance, the total compressive force at 1 A and 2 A resulted equal to 0.75 N and 1.64 N, respectively. These values were obtained by adding the value of 0.04 N to the value of the electromagnetically induced precompression plotted in Figure 3.9.

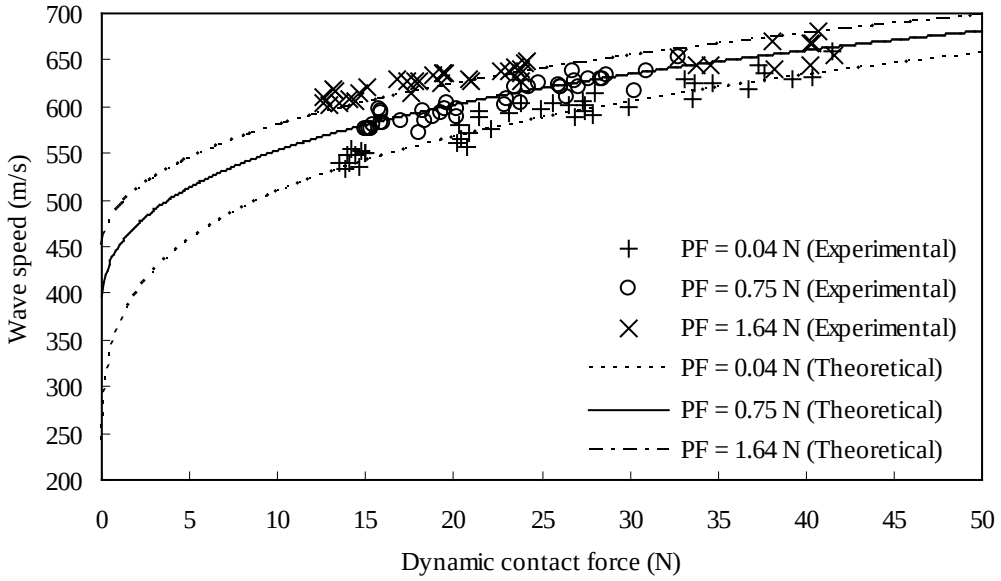

Figure 3.11. Dependence of the velocity of HNSWs on the magnitude of the dynamic contact force for both gravitationally and electromagnetically precompressed chain (PF denotes precompression)

Equation (2.19) reveals that the speed V_s of a HNSW depends on the pre-compressive force F_0. Figure 3.11 shows the theoretical prediction of the wave speed when the pre-compressive force (PF) is equal to 0.04 N, 0.75 N, and 1.64 N. Experimental data obtained in this study is overlapped to the theoretical predictions. For each measurement, the maximum value of the dynamic force $F_{m,e}$, measured by the embedded PZT, was converted to the

maximum contact force between neighboring beads F_m using Equation (3.7). The coefficient β was obtained from Figure 2 of reference [29].

The relationship between the velocity of the solitary wave and the applied current was investigated for the four different heights from which the striker was released. For each height and applied precompression, 10 acquisitions were obtained.

Even the striker was released from the same height, the dynamic force amplitude changes as the applied current changes. Such behavior is expected since there exists a change in the current/magnetic field results in a change of the striker's velocity as it approaches the top bead due to the magnetic force between the striker and the chain of beads. Furthermore, the coefficient β in Equation (3.7) also changes as the ratio of $F_{m,e}/F_0$ changes. Taking this into consideration, theoretical wave speeds for all acquisitions were calculated.

Table 3.2. The maximum and average errors of wave speeds

Height (mm)	Maximum error (%)			Average error (%)		
	I=0A	I=1A	I=2A	I=0A	I=1A	I=2A
10	3.02	2.19	3.70	1.48	1.07	1.99
20	3.77	3.62	2.98	1.80	1.26	1.81
35	2.55	2.18	1.53	1.36	1.08	0.82
60	3.46	2.95	5.07	1.56	0.87	2.47

The maximum and average errors for each height and current are listed in Table 3.2. The good agreement between the theoretical prediction and the experimental results is visible. Because the solitary waves observed in the experiments may have tails [7,25,29], it is difficult to decide where the beginning and end of each pulse are. Instead, the time interval, *t*, between instants in which the pulse reaches half of its amplitude for the first time and the crest, is considered. From the geometry of the solitary wave, theoretically $A*\cos^4(\omega t)$, the duration of the solitary wave, *T*, can be calculated as:

$$T = \frac{2\pi}{\pi - 2\sin^{-1}(2^{-1/4})} t \approx 5.49t \tag{3.8}$$

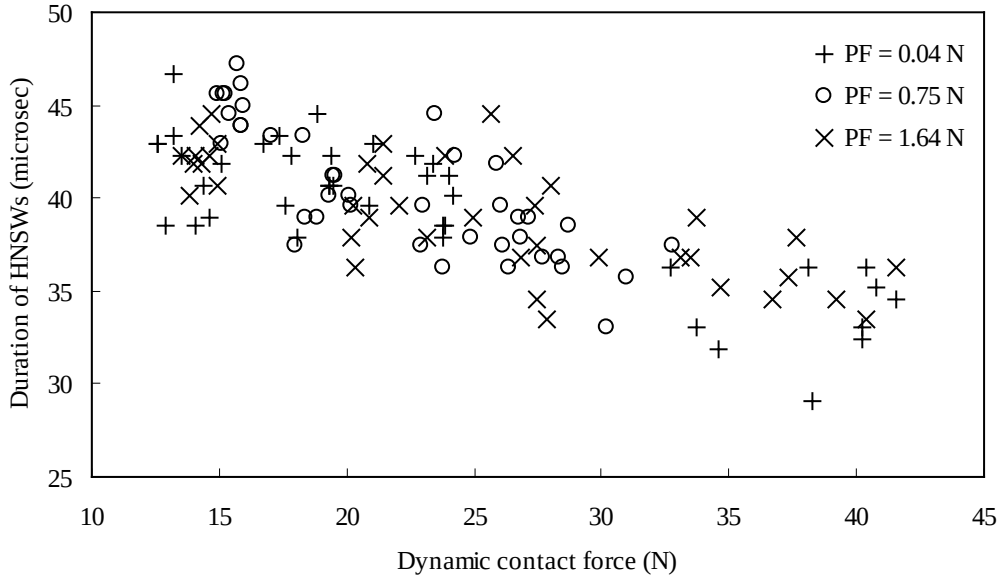

Figure 3.12. Relationship between the duration of solitary wave and the dynamic contact force

The relationship between the duration of the solitary wave, *T*, and the dynamic force magnitude, F_m, is shown in Figure 3.12. It can be seen that the duration of the pulse increases as the dynamic force magnitude decreases. This implies that the increase of the dynamic contact force increases the frequency of the HNSWs. When the dynamic contact force stays constant, the pre-compression has little effect on the duration/frequency of the solitary pulse; however, the pre-compression force applied in this experiment is relatively small.

The products of wave speeds V_s and durations *T*, which are equal to the wavelength of the HNSWs, were calculated and the results are shown in Table 3.3. The products which represent the spatial wavelengths are expected to be equal to five bead diameters, i.e. long, 23.8 mm in this case.

Table 3.3. The products of wave speeds and durations

Height (mm)	Average of product of wave speed and duration (mm)			Relative standard deviation (%)		
	I=0A	I=1A	I=2A	I=0A	I=1A	I=2A
10	23.0	26.3	25.4	4.07	3.70	6.83
20	23.1	23.9	26.1	7.08	5.57	5.15
35	23.1	24.2	25.8	9.65	7.98	4.54
60	22.7	23.3	22.2	5.11	5.44	8.48

3.2.4 Conclusions

In this section an electromagnetically induced precompression was applied to a one-dimensional chain of 20 general purpose low-carbon steel beads. The ability of using an electromagnet to tune solitary waves propagating in the chain of ferromagnetic beads is demonstrated experimentally.

The wave speed, amplitude and duration were measured for three different electric currents and four different heights from which the striker was released. These tests vary the value of the static precompression applied to the chain and the dynamic contact force. The experimental results agree very well with the theory derived from the long wavelength approximation.

The following conclusions can be drawn: (1) A wire wound into a coil can generate an electromagnetic field that can be used to apply a variable static precompression to a chain of general purpose low-carbon steel beads; (2) When the precompression is constant, the wave speed increases as the dynamic contact force increases. When the dynamic contact force is constant, the wave speeds increases as the precompression increases. This concept was demonstrated experimentally by using an electromagnet to adjust precompression and by changing the height from which the striker was released, thereby changing the velocity of the striker; (3) The product of wave speed and duration witnessed little change, indicating very little change in the spatial wavelength, as well.

The method presented in this section provides an easy way to tune the HNSWs propagating in a one-dimensional chain of ferromagnetic or weakly magnetic beads.

4.0 DESIGN OF A HNSW TRANSDUCER

This chapter introducers a HNSW-based transducer (hereafter referred as HNSW transducer) designed and built during this study. The effectiveness of the HNSW transducer to generate repeatable solitary waves was demonstrated through a simple experiment.

4.1 DESCRIPTION OF THE HNSW TRANSDUCER

A novel actuator was designed for the remote and automatic generation of HNSWs. Figure 4.1 shows a photo and the schematic of the HNSW transducer developed in this study. It consisted of a 4.8 mm diameter PTFE tube containing twenty stainless steel beads. Each bead was 4.76 mm in diameter and 0.45 g in weight. A low-carbon steel bead which has the same mass equal to 0.45 g was used as a striker. The pipe was surmounted by an electromagnet consisting of a coil of an AWG24 magnetic wire wrapped around an iron core. The iron core was a 13 mm diameter and 33 mm long rod. The electric resistance of the coil was equal to 7.4 Ω. The electromagnet was collocated inside a PTFE pipe with internal diameter equal to 39 mm, designed to accommodate also the tube containing the chain of particles. Once activated, the electromagnet was able to lift the striker up to 10 mm. For this actuator, the particles used to assemble the chain were made of

a non-ferromagnetic material to avoid undesired interactions between the beads in the chain and the electromagnet.

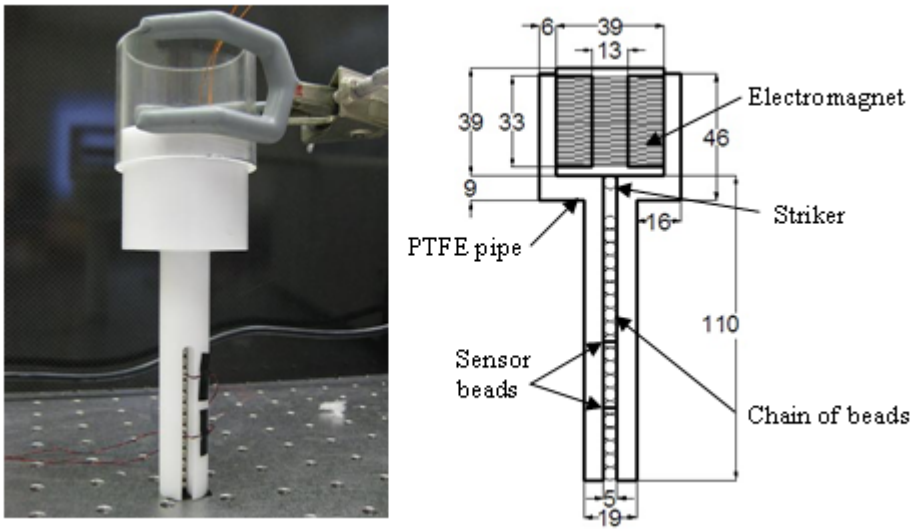

Figure 4.1. Photo and sketch of the HNSW transducer for the remote and automatic generation of HNSWs (dimensions are expressed in mm)

In order to further increase the range of impact velocities achievable with this actuator design, the direct current flowing in the electromagnet can be increased or the design of the coil can be modified by increasing the number of turns per unit length.

4.2 VALIDATION OF THE HNSW TRANSDUCER

To evaluate the capability of the transducer to generate HNSWs, the chain was instrumented with two sensors beads, positioned along the chain at the 10^{th} and 15^{th} position from the top and

connected to an oscilloscope. For this experiment the falling distance of the striker was set equal to 8.5 mm. In order to assess the repeatability of the generated pulses, fifty measurements were taken.

Typical force profiles generated by the HNSW transducer and recorded by the sensor beads are presented in Figure 4.2, where the experimental time histories are overlapped to a cos^4 function, which represents the shape of the pulse predicted by the long wavelength analysis [3]. The agreement between the experimental and the ideal pulses is evident.

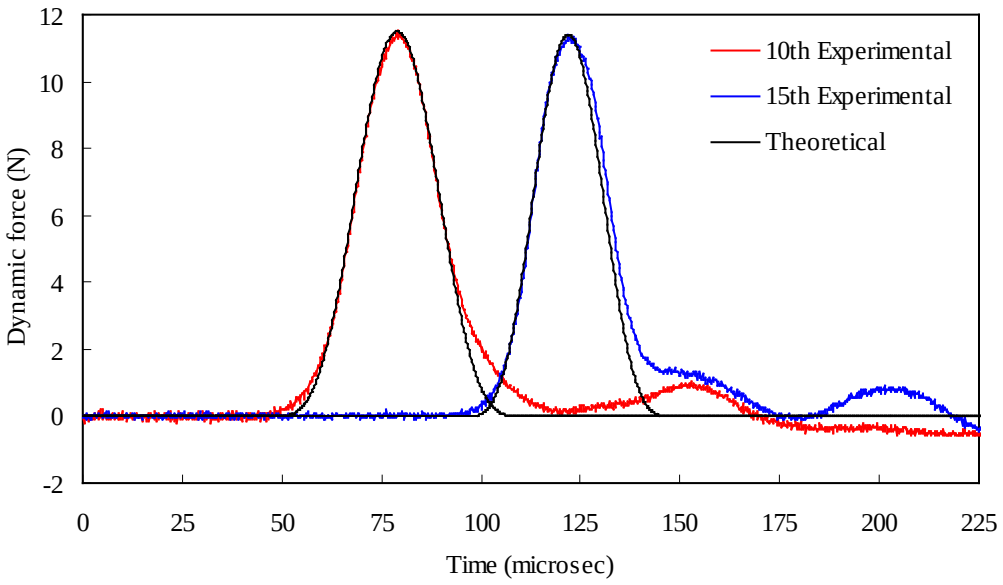

Figure 4.2. Typical waveforms generated by the HNSW actuator

Figure 4.3 shows the maximum dynamic force obtained in all fifty measurements extracted from the 10^{th} and 15^{th} bead. The mean value of the dynamic force measured at the 10^{th} particle was equal to 11.51 N with a standard deviation equal to 0.34 N, which is only 2.98% of

the mean value. The average value recorded by the 15th particle was equal to 11.38 ± 0.36 N. In this case, the standard deviation was equal to 3.17% of the mean value. The small standard deviations indicate the high repeatability of the signal generated with this transducer. It should be noted that the average dynamic force measured by the top sensor bead is only 1.17% greater than that measured by the bottom sensor bead. This indicates that the pulse's attenuation in the actuator was very small.

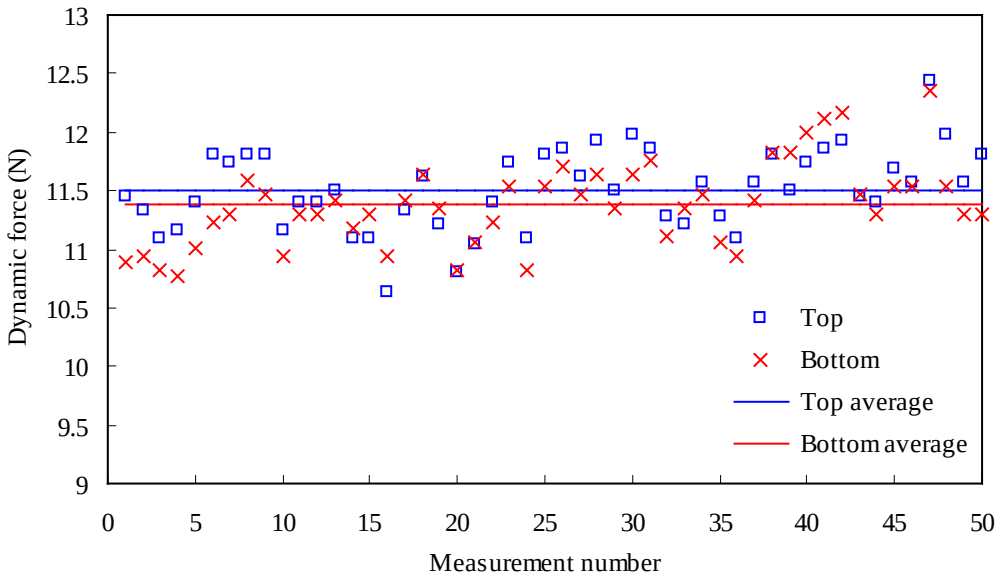

Figure 4.3. Values of the dynamic force measured by both sensor beads

The speed of the HNSW was calculated by detecting the arrival time of the pulse's peak in the instrumented beads and knowing their relative distance in the chain. Figure 4.4 shows the experimentally calculated wave speed as a function of the dynamic contact force. The theoretical prediction obtained from the long wave approximation is overlapped. The agreement between

experimental data and theoretical prediction is very good and it confirms the ability of the actuator to generate HNSWs.

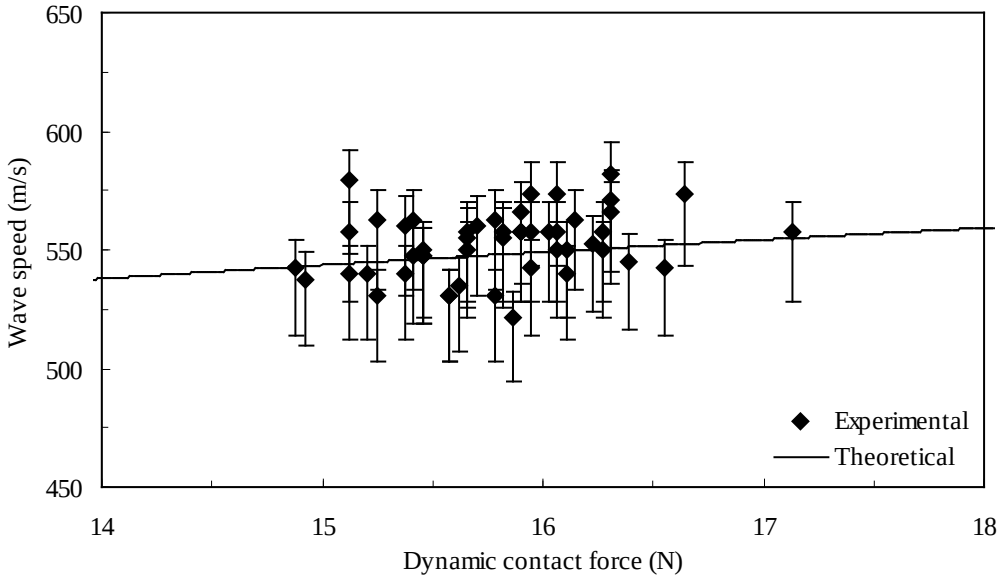

Figure 4.4. Wave speed as a function of the dynamic contact force at precompression equal to 0.053 N

The designed HNSW transducer is compact, low cost and easy-to-control. It has good repeatability, tunability and doesn't need couplant and the use of electrical arbitrary function generator. The actuator consists of a one-dimensional chain of particles surmounted by an electromagnet that lifts and releases the striker from a certain height. By remotely activating the electromagnet the movement of the striker can be guaranteed with high level of repeatability. This automatic excitation of HNSWs could be useful in applications where a remote placement of equipment or a complex geometrical arrangement of the chains is required. This design also allows increasing the repetition rate of the generated pulses which, in turn, can be useful in certain

applications such as nondestructive testing. Two piezo-gauges made from lead zirconate titanate with nickel-plated electrodes and custom micro-miniature wiring were embedded inside two of the steel particles to measure the incident and reflected HNSWs.

5.0 APPLICATIONS OF HNSW-BASED METHODS FOR NDE

In this chapter the applications of HNSW-based methods in the area of NDE and SHM are presented. The first section of this chapter illustrates general principle of the HNSW-based methods. Then, the rest of this chapter presents curing monitoring of cement, concrete, and two ton epoxy, assessment of bond condition of aluminum lap-joints, damage detection in composite plate by HNSW-based methods.

5.1 GENERAL PRINCIPLES OF HNSW-BASED METHODS FOR NDE

The interaction between HNSWs and linear materials at the interface between a chain of particles and a bulk material has been investigated by few researchers [8,19,23]. Falcon et al. [8] studied the bouncing behaviors of the impact at the interface between a chain of beads and a fixed wall. The solitary wave reflection at a rigid wall boundary has been studied by Xu and Hong [19]. Job et al. [23] investigated the collision of a single solitary wave with elastic walls with different hardness. The interaction of HNSWs with linear elastic media and the formation and propagation of reflected solitary waves were studied both theoretically, numerically and experimentally [51]. It shows that the formation and propagation of reflected solitary waves are highly dependent on

the elastic modulus and geometry of the adjacent linear medium. Furthermore, the observed sensitivity of reflected solitary waves to elastic modulus and geometry of both the adjacent materials and underlying layers, and it is important for monitoring the hydration process of cementitious materials because the specimen can't afford the weight of the actuator at the early stage of curing without putting an additional layer to enlarge the area of the interface.

In general, it has been observed that when the incident wave interacts with a "soft" neighboring media the formation of a primary reflected solitary wave (PSW) and a secondary reflected solitary wave (SSW) are formed. The transit time at a sensor particle between the incident and the reflected waves are referred as time-of-flight (TOF). The ratio of the PSW's amplitude to the amplitude of the incident solitary wave is referred as amplitude ratio of primary reflected solitary wave (ARP) and the ratio of the SSW's amplitude to the amplitude of the incident solitary wave is referred as amplitude ratio of secondary reflected solitary wave (ARS). The interaction with the "soft" interface results in a delayed formation of the PSW and SSW.

Here, the theoretical analysis by Yang et al. [51] is reviewed. For a chain of elastic beads interacts with a semi-infinite wall, assuming the kinetic energy of the striker is split between the Hertzian potential and the kinetic energy of the last bead against the bouncing wall, the contact time between last bead and the wall can be estimated as:

$$T_c \approx 3.218 m^{2/5} V_k^{-1/5} A\big|_w^{-2/5} \tag{5.1}$$

where V_k is the velocity of the striker, and the bead-wall contact stiffness $A\big|_w$ is given as:

$$A\big|_w = \frac{4\sqrt{R}}{3}\left(\frac{1-\nu^2}{E}+\frac{1-\nu_w^2}{E_w}\right)^{-1} \tag{5.2}$$

where E_w and ν_w are the Young's modulus and Poisson's ratio of the wall material.

$$A\big|_w = \frac{4\sqrt{R}}{3}\left(\frac{1-\nu^2}{E}+\frac{1-\nu_w^2}{E_w}\right)^{-1} \tag{5.3}$$

From the Nesterenko's long wavelength approximation [3-4], the speed of the incident solitary wave V_i is given as:

$$V_i = \left(\frac{16}{25}\right)^{1/5}(2R)\left(\frac{v_i A\big|_c^2}{m^2}\right)^{1/5} \tag{5.4}$$

where v_i is the bead incident velocity which was found $v_i \approx 0.682V_k$ by Chatterjee [10], and the bead-bead contact stiffness $A\big|_c$ is given as:

$$A\big|_c = \frac{E\sqrt{2R}}{3(1-\nu^2)} \tag{5.5}$$

Assuming the difference between the speed of the incident solitary wave and that of the reflected solitary wave can be ignored, the traveling time of solitary wave in the chain is

$$T_t = \frac{4N_1R}{V_i} \tag{5.6}$$

where N_1 is the number of beads between the sensor bead and the wall.

Replacing V_b in Equation (5.4) and substituting Equation (5.4) into Equation (5.6), we get the traveling time of in the chain

$$T_t \approx 2.361 N_1 m^{2/5} V_k^{-1/5} A\Big|_c^{-2/5} \tag{5.7}$$

The TOF and PSW can be expressed as

$$TOF\Big|_{PSW} = T_c + T_t \approx (3.218 A\Big|_w^{-2/5} + 2.361 N_1 A\Big|_c^{-2/5}) \left(\frac{m^2}{V_k}\right)^{1/5} \tag{5.8}$$

When the chain is in contact with two-layer composite media, based on the momentum and energy conservation, the ratio of the last bead reflection velocity v_r to the incident velocity v_i can be approximated as:

$$\frac{v_r}{v_i} = \frac{m - M_u}{m + M_u} \tag{5.9}$$

where M_u is the mass of the layer which is in direct contact with the chain.

Based on Equation (5.4),

$$\frac{V_r}{V_i} = \left(\frac{v_r}{v_i}\right)^{1/5} \tag{5.10}$$

where V_r is the speed of the reflected solitary wave. Then the traveling time T_t' in this case is

$$T_t' = 2 N_1 R \left(\frac{1}{V_i} + \frac{1}{V_r}\right) \tag{5.11}$$

Substituting Equations (5.6) and (5.10) into Equation (5.11), we can get

$$T_t' = \frac{T_t}{2}\left[1+\left(\frac{m-M_u}{m+M_u}\right)^{-1/5}\right] \tag{5.12}$$

The TOF of PSW for the chain in contact with two-layer composite is

$$\begin{aligned} TOF\big|_{PSW} &= T_c + T_t' \\ &\approx \left\{3.218A\big|_w^{-2/5} + 1.181N_1 A\big|_c^{-2/5}\left[1+\left(\frac{m-M_u}{m+M_u}\right)^{-1/5}\right]\right\}\left(\frac{m^2}{V_k}\right)^{1/5} \end{aligned} \tag{5.13}$$

The contact delay T_l between two layers of composite is

$$T_l = \pi\sqrt{\frac{M_u}{k_d}} \tag{5.14}$$

where k_d is the stiffness of the second layer of the composite.

Then, the TOF of PSW can be expressed as the sum of the TOF of PSW and the linear medium contact delay:

$$\begin{aligned} TOF\big|_{SSW} &= TOF\big|_{PSW} + T_l \\ &\approx \left\{3.218A\big|_w^{-2/5} + 1.181N_1 A\big|_c^{-2/5}\left[1+\left(\frac{m-M_u}{m+M_u}\right)^{-1/5}\right]\right\}\left(\frac{m^2}{V_k}\right)^{1/5} \\ &+ \pi\sqrt{\frac{M_u}{k_d}} \end{aligned} \tag{5.15}$$

To estimate the ARP and ARS or to get more accurate estimation of TOFs, numerical simulation or finite element analysis can be used and the dissipation and restitution loss need to be considered in these models.

5.2 SETTING MONITORING OF PLASTER OF PARIS BY HNSW

In this section we present a nondestructive technique based on the propagation of HNSWs to monitor the hydration of cement. The HNSW transducer was used to inject HNSWs into a sample of fresh gypsum cement and to detect the waves reflected from the cement's surface. We assessed the hydration process of the cement specimen by analyzing the time-of-flight and the amplitude of the reflected HNSWs. We found that the wave's properties were dependent on the mechanical properties of the cement paste. We compared the experimental results with numerical simulations (done by colleagues J. Yang, D. Kathri and C. Daraio from Caltech) based on a simplified finite element model, and compared the Young's modulus and ultimate compressive strength obtained nondestructively with the same quantities obtained from destructive tests. We observed good agreement between experiments and numerical simulations for all cases considered.

5.2.1 Introduction

The quality and the durability of cement-based products are influenced by early stages of hydration [62-63]. The observation of the hydration process in cement-based materials permits to predict their long-term behavior, and to accurately estimate their setting time [64-65]. In the past 20 years, several NDE techniques have been proposed to monitor the hydration of cement. These methods correlate certain mechanical, electrical, or acoustical parameters with the cement or concrete properties by using empirical relationships [66]. The most widely used NDE technique

is based on the propagation of ultrasounds [64-65,67-80]. Other methodologies make use of electromagnetic waves [81-82], electrical resistivity [79], and X-ray diffraction [75]. In ultrasonic-based methods, cement samples are typically inspected by commercial transducers that generate longitudinal [65,68-71,75-77,79-80] or longitudinal and shear [64,72-73] bulk waves. Parameters such as wave speed and attenuation are then measured and empirically correlated to the cement material properties. This approach is usually referred to as the ultrasonic pulse velocity (UPV) method [83]. To obtain good signal-to-noise ratio, longitudinal wave transducers cannot be used to generate transverse waves and vice versa. Thus, to use both shear and longitudinal waves, at least four transducers are necessary. If the access to the back wall of the sample is not practical, the wave reflection method can be adopted. In this approach, the reflection loss of ultrasonic shear [67,74] or longitudinal [65,77,82] waves at an interface between a buffer material, typically a steel plate, and the cementitious material is monitored over time. The amount of wave attenuation depends on the reflection coefficient, which in turn is a function of the acoustical properties of the materials that form the interface [66].

In this section, we propose a novel NDE paradigm to monitor cement hydration at early age based on the use of HNSWs. The HNSW transducer described in Chapter 4 was used. We injected a single pulse of HNSW into a cement specimen using a granular crystal and propose to monitor the hydration process by measuring the reflected waves formed at the actuator/cement interface.

The experimental results are compared to a simplified finite element model (using ABAQUS), and to the ultimate compressive strength and Young's modulus of cement cubes obtained following the ASTM C109 [84]. The experimental results from the proposed HNSW-

based method are in good agreement with numerical data, and they show strong correlation with the measured mechanical properties obtained from destructive tests of the cement specimens. With respect to previous works, the novelty and the advantage of this HNSW-based NDE technique is multifold: 1) it exploits the propagation of HNSWs in granular systems; 2) it employs a cost-effective actuator/sensor in a combined form; 3) it measures several waves' parameters that can be used to correlate multiple cement variables; 4) it does not require, unlike UPV method, the exact knowledge of the distance between a transmitter and a receiver and does not require the access to the sample back-wall.

5.2.2 Experimental setup

To evaluate the proposed NDE methodology, we prepared one conical frustum sample of fast setting USG® Ultracal 30 gypsum cement. This material is low expansion rapid-setting gypsum cement used in the building industry as a surface finish of interior walls and in the production of drywall products for interior lining and partitioning. In our experiment we prepared a paste with water and cement in a ratio of 0.38 in weight, as recommended by the manufacturer. The paste was poured into a plastic mold after 5 minutes of mixing. The conical frustum sample obtained from the mold was 77 mm high, with top and bottom diameters equal to 62 mm and 42 mm, respectively. A 40 × 40 × 0.254 mm aluminum sheet was placed on top of the specimen 30 minutes after pouring the paste in the mold, and the granular chain actuator was placed on top of the sheet 7 minutes later. The experimental setup is shown in Figure 5.1. A DC power supply provided current to activate the electromagnet located on the top of the granular chain.

Instrumented sensor particles inserted in the 11th and 16th particle positions measured the incident and reflected HNSWs, which were recorded by an oscilloscope. The signals were digitized at 5 MHz sampling rate. Five measurements were taken every three minutes during the first 90 minutes of the cement age. Then, five measurements were recorded every six minutes until cement age was 180 minutes. Monitoring was stopped three hours after mixing, in accordance to the manufacturer's nominal setting time.

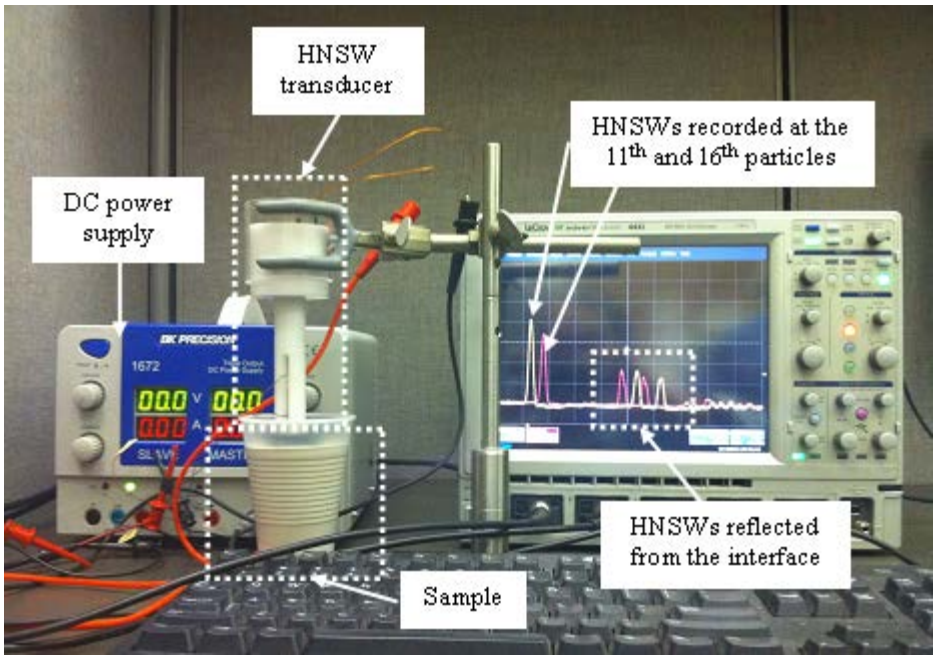

Figure 5.1. Photo of the experimental setup for cement setting monitoring test

5.2.3 Experimental results

5.2.3.1 HNSW measurements

Figure 5.2 shows the time history of the force measured by the 11th particle in the chain, at five different times of the hydration process. The top plot represents the HNSW profile after 45 minutes of curing process, while the bottom plot shows the force signal measured after 120 minutes of cement age. In this figure, the incident pulse and the primary and secondary reflected waves are clearly visible. We also observe that the shape, amplitude, and travel time of the reflected waves changed with time. It is notable that Figure 5.2 is very similar to Figure 5.3, implying a close relationship between cement's curing time and its elastic modulus. The variation of elastic modulus as a function of the curing time will be addressed in subsection 5.2.3.3.

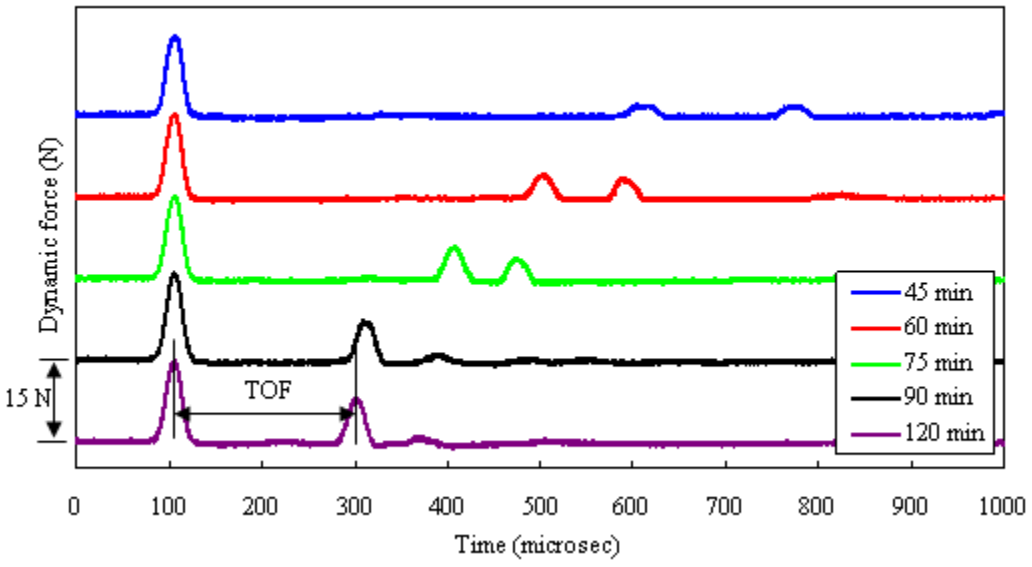

Figure 5.2. The force profiles measured from the 11th bead at different cement ages

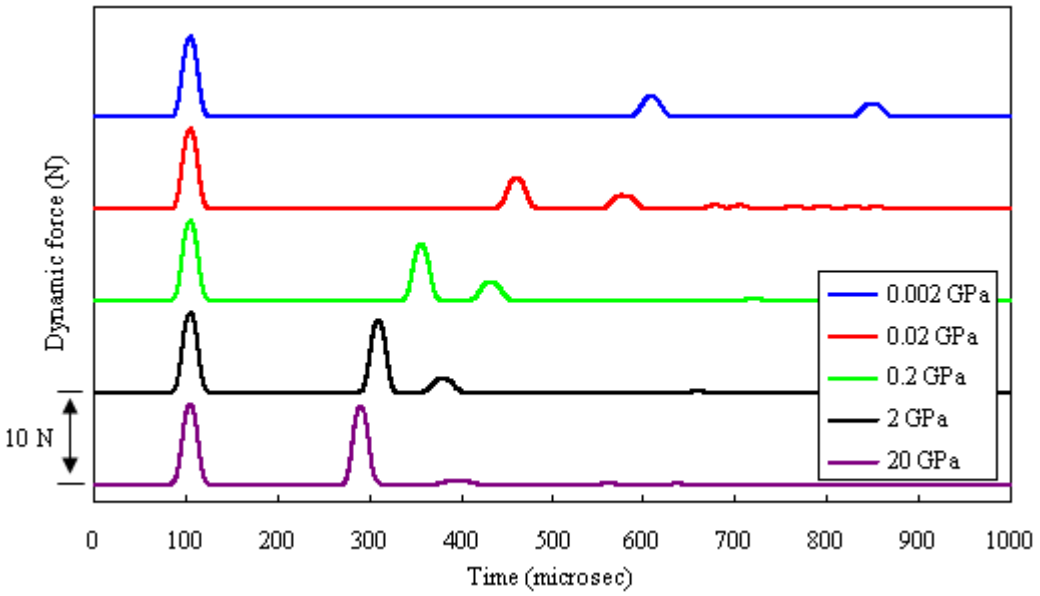

Figure 5.3. FEM simulation of HNSW interaction with gypsum cement samples in various elastic condition (done by J. Yang, D. Kathri and C. Daraio)

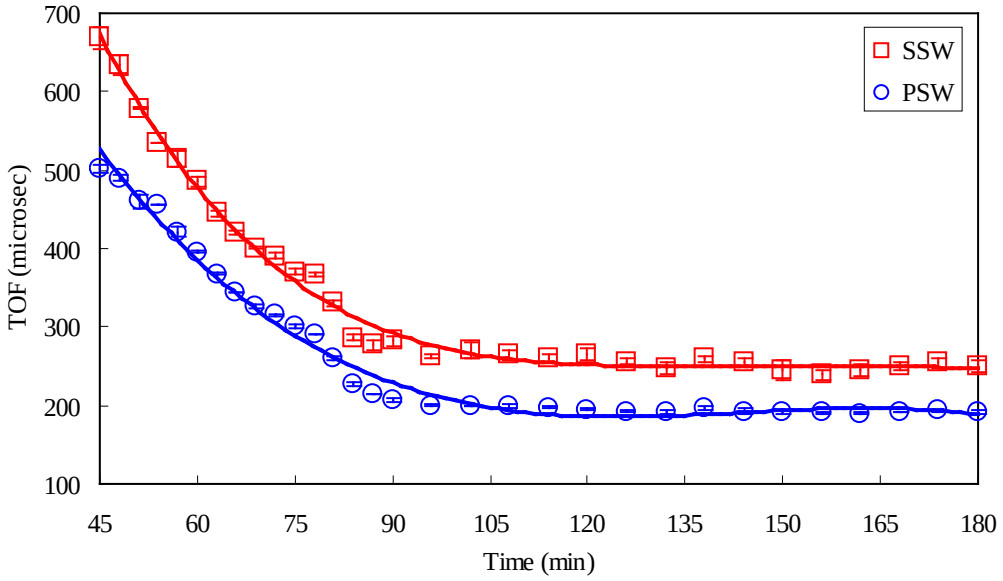

Figure 5.4. TOF of the PSW and SSW as functions of cement age

Figure 5.4 shows the measured TOFs of both primary (blue line with circles) and secondary (red line with squares) reflected waves as a function of the hydration time. Each dot indicates the mean value of the five experimental measurements, and the vertical error bars represent the 95.5% (2σ) confidence interval. The barely visible error bars demonstrate the repeatability of the proposed methodology. The trend evident in Figure 5.4 clearly denotes the presence of a two-stage evolution. In the first stage, lasting between 45 and 90 minutes, the TOF values of PSW and SSW decrease approximately exponentially. After 90 minutes the variation of the TOF plateaus, changing only slightly with increasing cement age. The trends observed in these results are well captured by the numerical data in Figure 5.5. Discrepancies between numerical data and Figure 5.4 stem from the different physical parameters used in the horizontal axis and from the approximations used in the numerical model. Figure 5.6 shows the wave speed of the incident solitary wave (blue line with circles) and of PSW (red line with squares) as a function of curing time. Similarly to the analysis of the TOF, we find that the speed of the primary reflected waves becomes less sensitive to the materials properties of the cement, as the curing time progresses. We also observe that the incident wave velocity remains almost constant in all tests performed.

The variations of the ARP and the ARS as a function of the cement age are shown in Fig. 10. While the amplitude ratio of the primary wave shows increases with cement age (blue line with circles), the ARS exhibits a relatively complex behavior during the curing process (square red line). It is worth noting that the amplitude of the primary reflected wave has a six-fold increase with respect to the fresh cement.

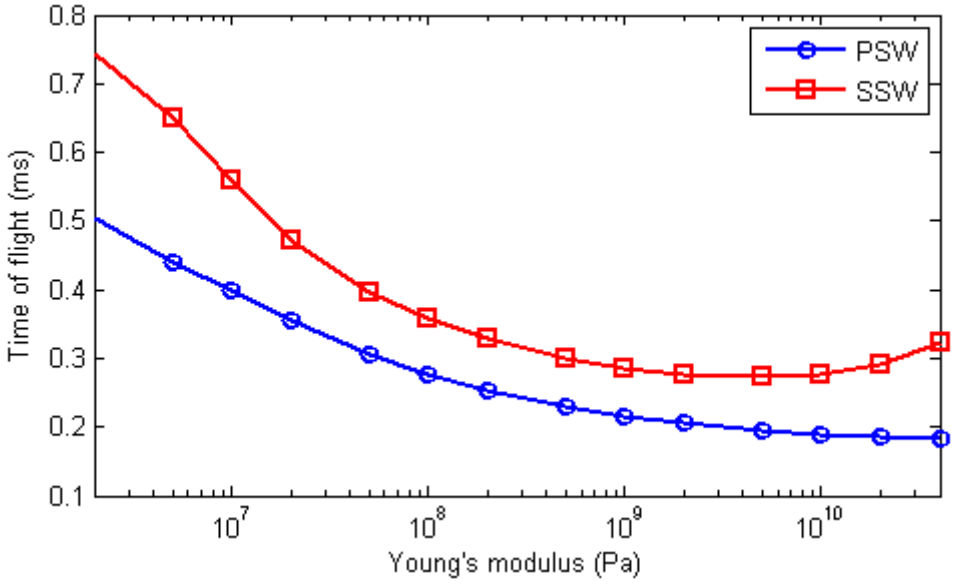

Figure 5.5. Numerical results showing time of flight and propagating speed of HNSWs (done by J. Yang, D. Kathri and C. Daraio)

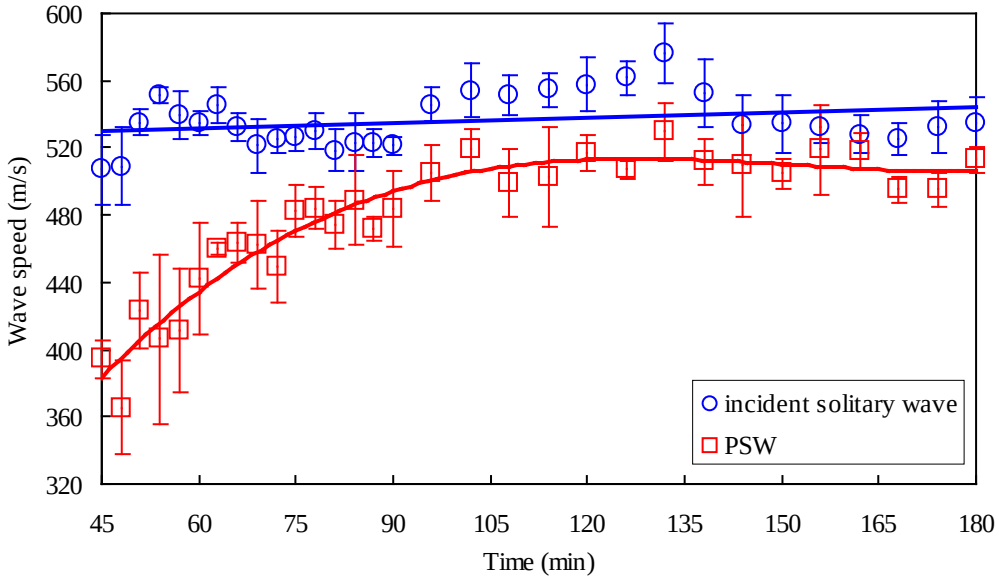

Figure 5.6. The speed of the incident solitary wave and PSW as functions of cement age

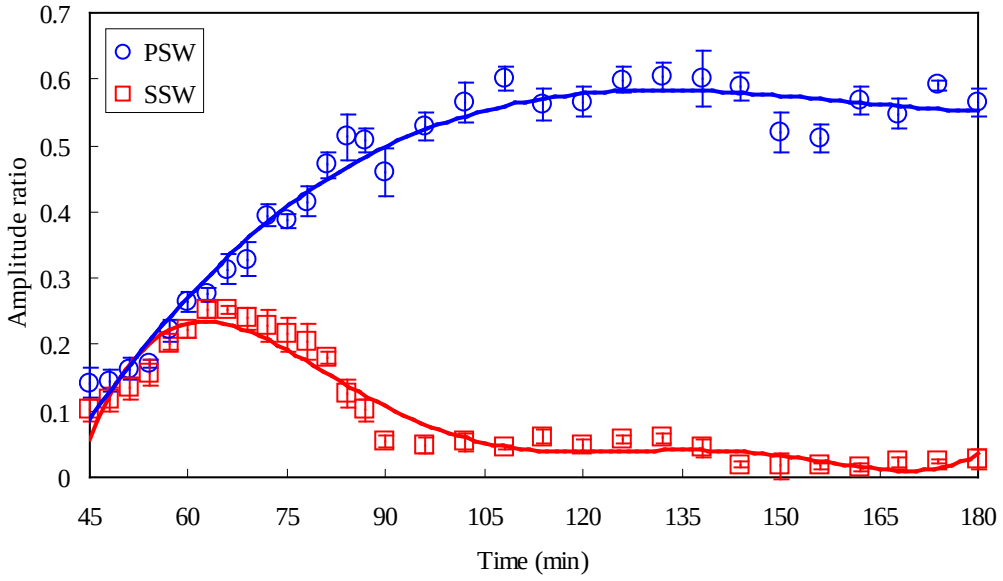

Figure 5.7. Amplitude ratios of PSW and SSW as functions of cement age

5.2.3.2 Compressive strength test

Uniaxial compression tests were performed according to ASTM C109 [84] using a Test Mark machine operated in displacement control. Eighteen 50-mm cubes were prepared using the water-to-cement ratio (0.38 in weight) suggested by the manufacturer. The paste mixture was blended three minutes prior to pouring into the molds. Each sample was removed from the mold before testing. Figure 5.8 shows the measured compressive strength as a function of the hydration time superimposed to the TOF variation of the PSW as recorded by the 11^{th} bead. We observe that the cement strength increases drastically up to the cement age of 90 minutes and becomes approximately identical afterwards. This is in agreement with the behavior of extracted features from HNSWs, as observed in Figure 5.4.

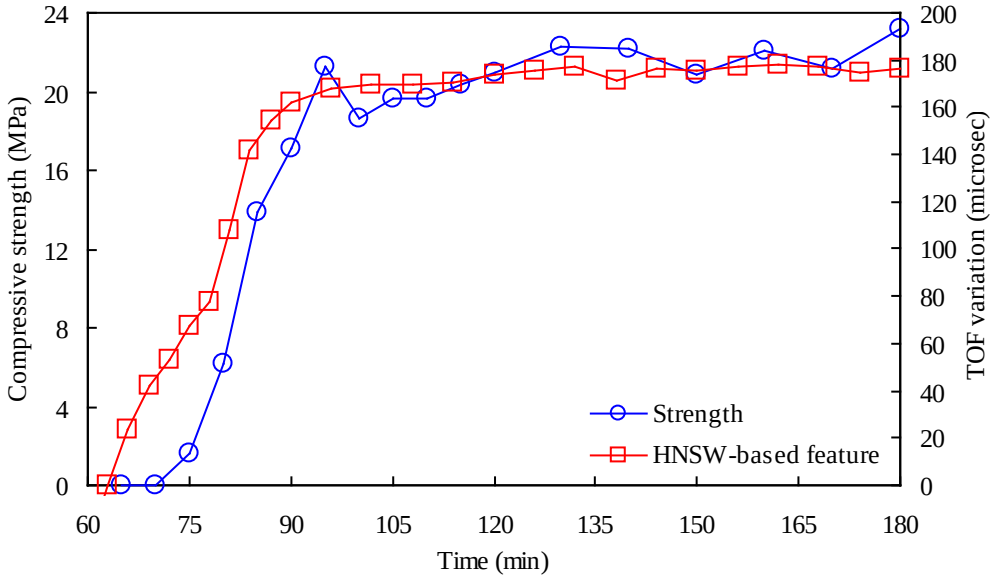

Figure 5.8. Measurements of cement compressive strength as a function of the cement age superimposed to the TOF variation of the PSW as recorded by the 11th bead

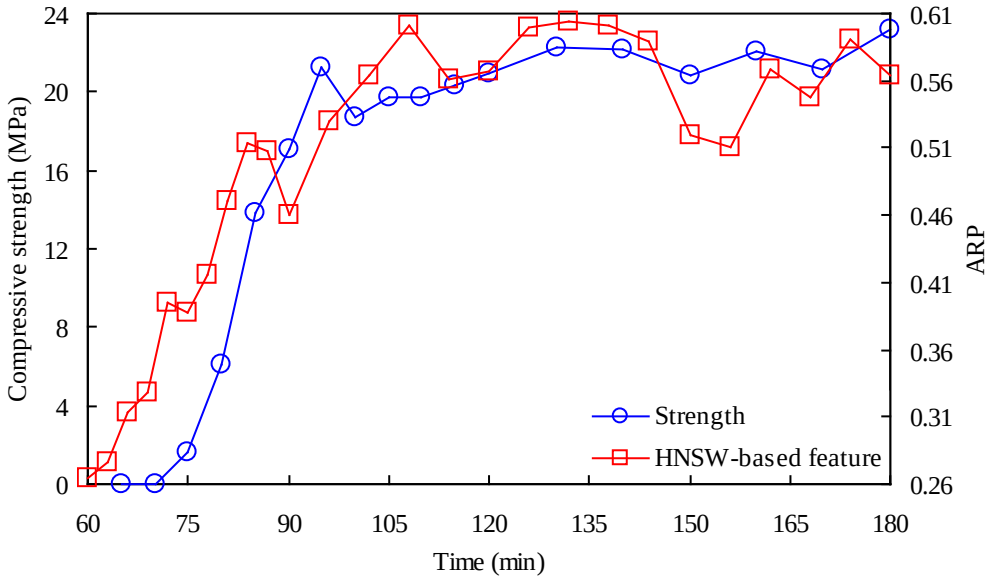

Figure 5.9. Measurements of cement compressive strength as a function of the cement age superimposed to the ARP as recorded by the 11th bead

To compare the measured strength with the HNSW responses, we superimpose the plots of TOF and ARP on the top of the strength curve as shown in Figure 5.8 and Figure 5.9 respectively. For the sake of comparison, we used "TOF variation" in Figure 5.8, which represent the deviation of the measured TOF values from the TOF recorded at 65 minutes. As demonstrated in both Figure 5.8 and Figure 5.9, the behavior reflected HNSWs match well with the measured strength of cement specimens. This implies the ability of the novel HNSW-based NDE approach to capture the variation of the cement's compressive strength.

5.2.3.3 Young's modulus test

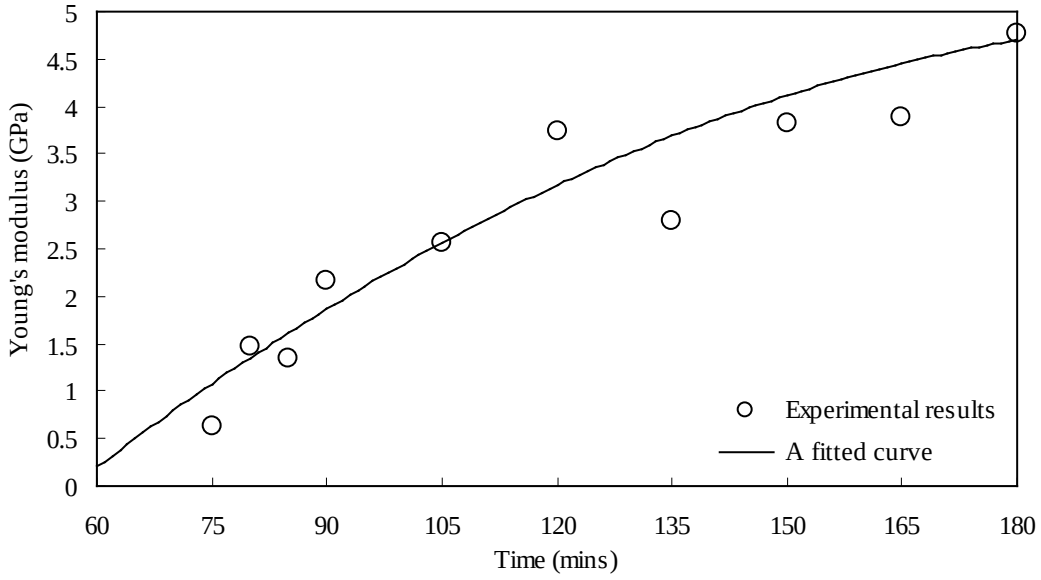

Figure 5.10. Young's modulus of 50-mm cubic cement samples as a function of cement age

To measure the elastic modulus of the cement paste, ten 50-mm cubes were tested with a load frame (MTS Systems Corporation, frame number 810, load cell number 661.21) operated in

displacement control. Both compressive force and displacement were recorded. The Young's moduli were extracted from the stress-strain curves and are shown in Figure 5.10 as a function of the paste's age. We observe an increase of the measured Young's moduli for samples with higher cement age.

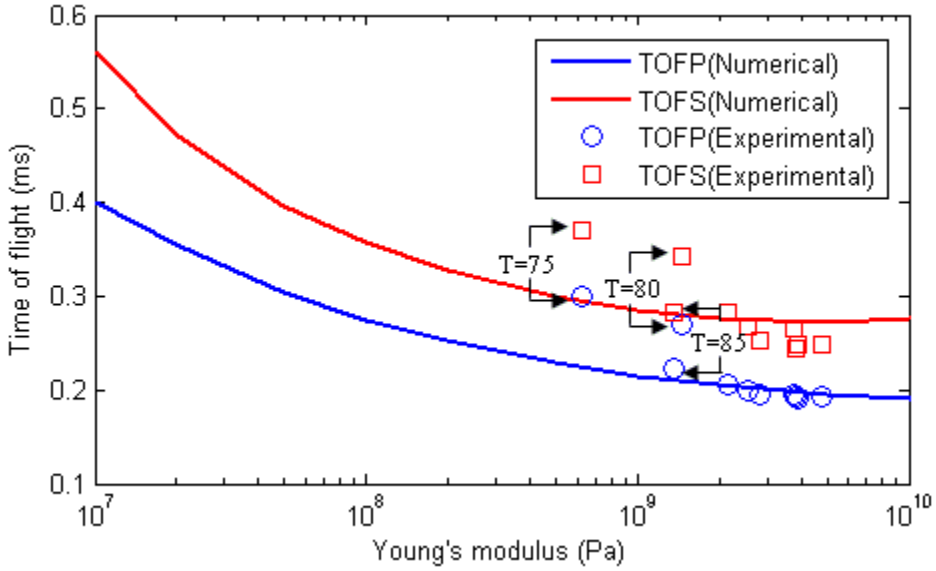

Figure 5.11. Time-of-flight as a function of the Young's modulus of 50-mm cubic cement samples

Based on the experimental relationship between the cement ages and their corresponding elastic moduli presented in Figure 5.10, we can now describe the responses of HNSWs as a function of cement's elastic modulus. We first obtained the relation between the measured TOF and the Young's modulus as shown in Figure 5.11. The numerical predictions in Figure 5.5 are superimposed to the experimental values (blue curve for PSW and red curve for SSW). For the sake of clarity the results of the first three stiffness measurements (at 75, 80, and 85 minutes) are

highlighted. It can be seen that the first two measurements show significant deviations from the numerical results. This is due to the fact that the numerical simulation models the cement as an elastic material despite the fact that the cement, particularly at early age, presents soft, inelastic characteristics. Once the cement becomes stiffer, there is an excellent agreement between the experimental and the numerical results. This demonstrates that our HNSW-based method is highly sensitive to the mechanical property of cement specimens as long as the local properties close to the actuator are identical to the bulk properties of the material.

The behavior of the amplitude ratio of the reflected solitary waves as a function of the Young's modulus presents similar trends. However, in this case the experimental results present smaller amplitudes than the numerical results because of the presence of dissipation (not accounted for in the numerical model). In the future, we expect that taking the dissipation into account and using more sophisticated numerical models [66] will enable a more detailed description of the HNSW attenuation during the hydration of cement-based materials.

5.2.4 Discussion and conclusions

This section describes a novel nondestructive testing method based on the propagation of HNSWs as acoustic information carriers to monitor the hydration of quick-setting cement. A cost-effective actuator/sensor made of a chain of spherical particles (i.e., a granular crystal) and an electromagnet was used for the generation and detection of the HNSWs. An experimental study was conducted and compared to the numerical and the result of a standard compression test. It was found that a single pulse perpendicularly incident to the actuator/cement interface

results in a series of reflected pulses, categorized into a primary solitary wave (PSW) and a secondary solitary wave (SSW). The amplitudes and the time-of-flight (TOF) of these two reflected waves are strongly dependent on the stiffness of the cement. The experimental findings from the HNSW measurements were supported by a simplified finite element model that captured the sensitivity of the proposed HNSW-based method to the change of cement's elastic modulus. The experimental results obtained using HNSWs were also in agreement with experimental data obtained using conventional mechanical tests performed according to the ASTM C109 [84].

The nondestructive approach proposed here can provide unique advantages over conventional methods based on linear ultrasonic bulk waves. With respect to the ultrasonic pulse velocity (UPV) method, the present approach requires only one transducer (instead of at least two), and therefore, it allows simpler access to the test specimen. With respect to the wave reflection method, where only the reflection coefficient is affected by the cement age, the present approach can virtually exploit three parameters: 1) the time-of-flight (TOF) of the primary reflected waves, 2) the TOF of the secondary reflected waves, and 3) the amplitude of the reflected waves. Moreover the HNSW-based method does not require the use of electronics for the generation of high-voltage input signals, contrary to piezoelectric transducers.

5.3 CURING MONITORING OF CONCRETE BY HNSW

In the rest of this chapter we present the study relative to the use of the HNSW transducer to monitor the development of strength in hydrating concrete. The TOF and the amplitude of the HNSWs reflected at the interface are measured and analyzed with respect to hydration time, and correlated to the initial and final set times established by the penetration test (ASTM C 403 [85]). It is concluded that the TOF of the reflected waves can be used to characterize the initial and final set time for the mixture.

5.3.1 Introduction

The early stage of hydration influences the quality and the durability of cement-based products. For instance, as a result of the chemical reactions between water and the cement during hydration of the concrete, the mixture progressively develops mechanical properties. Final set for the mixture is defined as the time that the fresh concrete transforms from plastic into a rigid state. According to ASTM C403 [85] the times of initial and final set correlate to two resistance pressure levels of 3.4 and 24.6 MPa, respectively. These pressures characterize the resistance of the mortar sample, obtained through wet sieving of the mixture, against the penetration of multi-sectional metal needles.

The correct estimate of the hydration progress and of the final set in freshly-constructed concrete pavements are crucial to determine when to open the section to traffic or when to sawcut the joints in jointed plain concrete pavements (JPCPs). A time period between 7 and 14

days has traditionally been required by construction specifications before a newly-placed section can be opened to traffic [86]. Shortening this period maximizes productivity rates while minimizing traffic delays. Special care needs to be taken in determining the earliest time that the joints can be cut in JPCPs. Late sawcutting can result in undesirable cracking of the concrete due to temperature-induced volumetric changes and drying shrinkage deformations.

Curing temperature is one of the key factors that affect the hydration rate and therefore the development of strength in fresh Portland cement concrete (PCC). In the field, concrete slabs most likely experience a temperature history other than that in the isothermal conditions. As such, the effects of temperature on the time-dependent mechanical properties need to be considered. A simple index that has been widely used for this purpose for freshly-placed concrete slabs is maturity. Maturity-strength relationships can be used to predict the strength evolution based on the temperature history of the mixture. Maturity, though, is very specific to the concrete mixture proportions and source of the constituents within the mixture. Among drawbacks of the maturity method is that it needs to be re-established anytime the source or quantity of a particular constituent in the concrete mixture is changed. It is also known that slight changes in the mixing, delivery, and proportioning may result in a different temperature history in the concrete. For this reason, direct but simple nondestructive measurements are needed to monitor the development of the mechanical properties in newly-placed concrete pavements.

NDE techniques have been widely adopted over the past two decades for monitoring the development of strength in fresh concrete. Most of these techniques are based on the measurement of the velocity of linear bulk ultrasonic waves propagating through a concrete sample. Traditionally, commercial transducers are used to generate longitudinal [76,87-93], or

both longitudinal and shear waves [94]. Parameters, such as wave speed and attenuation are measured and empirically correlated to the material properties. This approach is usually referred to as the ultrasonic pulse velocity (UPV) method. To obtain an acceptable signal-to-noise ratio, longitudinal wave transducers cannot be used to generate transverse waves and vice versa. Thus, to use both shear and longitudinal waves, at least four transducers are required. If the access to the back wall of the sample is practical, the wave reflection method can be adopted. In this approach, the amplitude of the shear waves [66,94-100] or the longitudinal waves [77,101], or both [102] at an interface between a buffer material, typically a steel plate, and the concrete is monitored over time. The amount of wave reflection depends on the reflection coefficient, which in turn is a function of the acoustical properties of the materials that form the interface [94].

Besides the use of bulk waves, other NDE technologies proposed to observe the growth of mechanical properties in concrete are based on guided ultrasonic waves [103], surface wave [104-105], fiber optics [106] and acoustic emission [107].

In this study we proposed a novel NDE paradigm to monitor the strength development in hydrating concrete. The method was based on the use of HNSWs. The HNSW transducer was used to generate solitary waves and detect their reflection at the transducer/concrete interface.

With respect to previous works on ultrasonic-based NDE for concrete, the novelty and the advantage of the proposed approach is multifold: 1) it exploits the propagation of HNSWs in granular systems; 2) it employs a cost-effective actuator/sensor in a combined form; 3) it measures several waves' parameters that can be eventually used to correlate few concrete variables; 4) it does not require, unlike UPV method, the exact knowledge of the distance between a transmitter and a receiver and does not require the access to the sample back-wall.

This section presents discussions of the preliminary results of an initiative laboratory experiment using this NDE technique.

5.3.2 Experimental setup

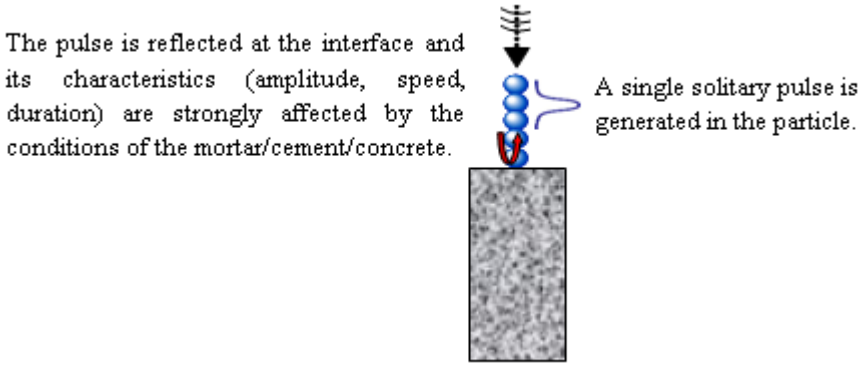

Figure 5.12. Schematics of the HNSWs-based NDE approach for monitoring concerte curing

Figure 5.12 illustrates the general principles of the proposed NDE technique. A HNSW-based transducer, here schematized with a chain of spherical particles, is in contact with the surface of the concrete. A thin (< 1 mm thick) aluminum sheet is placed in between the transducer and the concrete to prevent the penetration of the bottom sphere into the fresh concrete. The impact of a striker, i.e. a particle of equal size and mass of the other particles composing the chain, generates a single pulse of HNSW that propagates through the chain and is partially reflected at the interface. When the material under the chain has high values of Young's modulus a single HNSW is reflected from the interface. However, when the material adjacent to the granular chain is "softer" multiple HNSW can be generated [8,51]. In the proposed NDE approach we

monitored the waves reflected from the transducer/concrete interface using instrumented particles, herein indicated as sensor beads, inserted in the chain. The characteristics of the reflected pulses in terms of their TOF, AR and wave speed were correlated to the progression of the hydration process.

The HNSW transducer shown in Figure 4.1 was used to generate and detect the HNSWs. In this test, the sensor beads were positioned along the chain at the 11^{th} and 16^{th} position from the top. To automatically control the HNSW transducer and improve its repeatability, the electromagnet of the HNSW transducer was controlled by a National Instrument – PXI unit running in LabView.

Table 5.1. Summary of the PCC mixture design used for the test

Materials	Batch weight (kg/m^3)
Cement (Type I)	345
Fly Ash (Class C)	12
Water	145
Fine aggregate	744
Coarse aggregate (#57 Gravel)	1008

An experiment was performed in the laboratory on a 15.24 cm by 30.5 cm cylindrical concrete specimen. The design mixture for the concrete is summarized in Table 5.1.

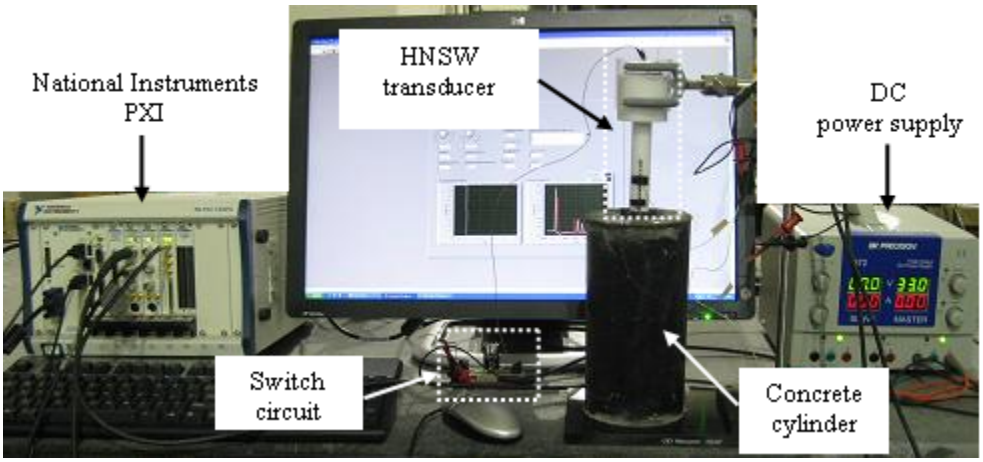

Figure 5.13. Photo of the experimental setup of concrete curing monitoring test

The concrete cylinder was cast at 8:30 AM in the laboratory. The concrete was mixed at a batch plant approximately 7 miles away from the laboratory. The time water contacted the cement was estimated to be around 8:00 AM. Therefore, one half hour was added to the duration of the test to account for the travel time from the batch plant to the laboratory. A 40 x 40 x 0.254 mm aluminum sheet and the actuator were placed on top of the specimen five minutes after the casting of the specimen. The NDE test procedure was started immediately after placing the sheet. Ten measurements were taken every 15 minutes for a duration of ten hours. A photo of the setup is shown in Figure 5.13. The initial and final set times were also established for the mixture by performing the ASTM C 403 [85] on a wet sieved mortar sample obtained from the mixture.

5.3.3 Experimental results and discussion

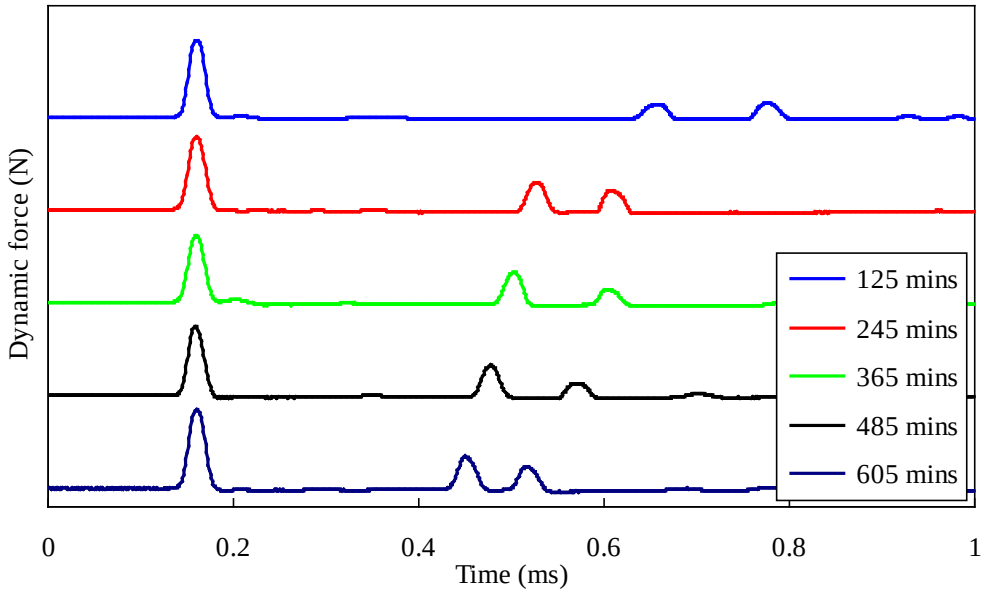

Figure 5.14. Force profile of the HNSWs waveforms recorded at different ages of concrete (The force profiles are measured from the 11th bead in the HNSW transducer)

Figure 5.14 shows the temporal force profiles computed at the 11th particle, when an incident solitary wave interacted with concrete at five different instances, namely 2-, 4-, 6-, 7.25-, and 10-hours. The signals obtained for each run are shifted vertically for better comparisons. Three pulses are visible for each instance. The first pulse represents the incoming solitary waves arriving at the sensor bead, while the second and third pulses are the PSW and SSW, respectively. It is noticeable in the figure that the TOFs of both the SSWs and PSWs are strongly dependent on the age of the sample. As the hydration progresses, the sample's stiffness increases and the TOF of the SSWs and PSWs decreases. Also as the sample ages, the amplitude of the PSW increases, while the TOF of the PSW decreases.

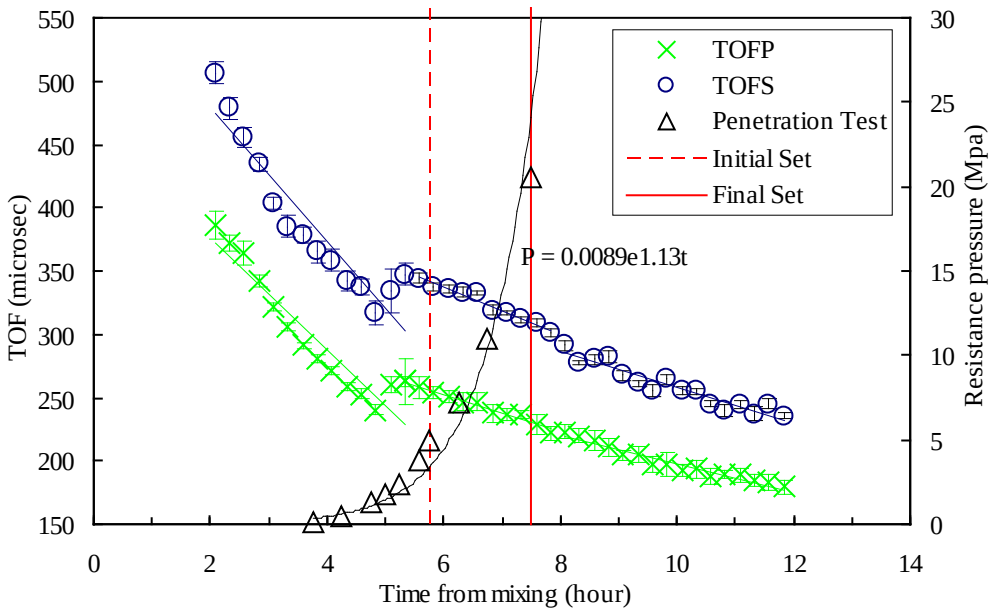

Figure 5.15. TOF of the PSW and SSW and penetration resistance as a function of time

Figure 5.15 shows the measured TOFs of both the SSW (green crosses) and the PSW (blue circles) as a function of the hydration time. Each data point in the figure indicates the mean value of the ten experimental measurements, and the vertical error bars represent the 95.5% confidence interval. The small value of the standard deviation demonstrates the repeatability of the experimental apparatus. The change in the penetration resistance over time as established by the ASTM C 403 is also superimposed in Figure 5.15 (black triangle). By observing the values of the TOF of both reflected waves, it can be seen the presence of two trends, i.e. the concrete denotes a two-stage behavior. In the first stage, lasting for about 300 minutes, the TOF values of both the PSW and SSW show a rapid drop. The transition between the two stages is consistent with the time of initial set, established by the penetration test. Proceeding this point, the decrease in the TOF continues with a considerably different rate (more gradual) between until minute 485.

At this time, the rate of decrease in the TOF with time changes again very slightly and maintains thereafter. The transition point identified at minute 485 is relatively consistent with the time of final set, 460 minutes, established by the penetration test.

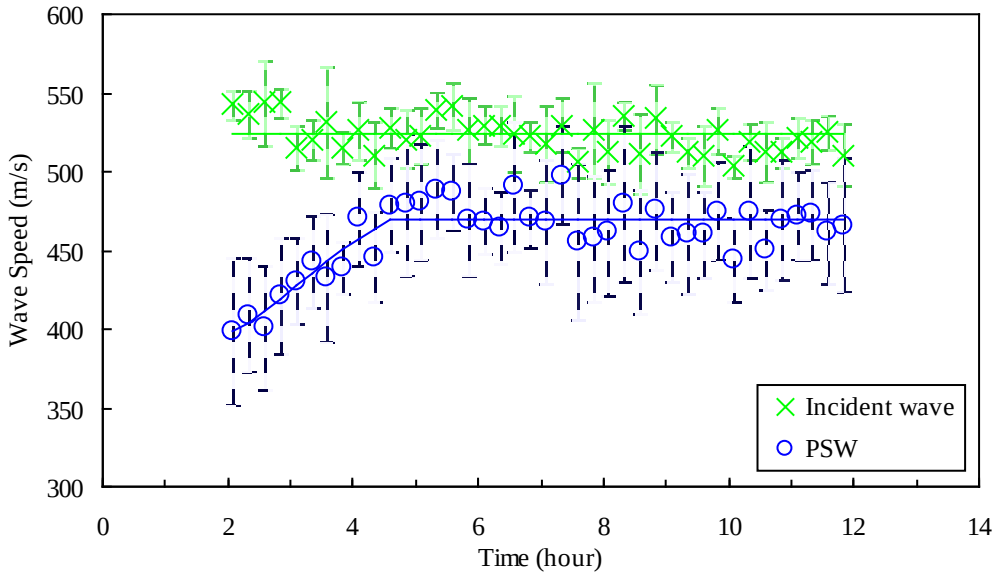

Figure 5.16. Experimentally measured speeds of incident HNSW and PSW

Figure 5.16 shows the wave speed of the incident solitary wave (green crosses) and of the PSW (blue circles) as a function of the concrete age. The speed is calculated by dividing the distance of the sensor beads by the measured time of arrival at these sensors beads. It can be observed that that, similar to the TOF, the speed of the PSW shows an increases by about 17% over the first 300 minutes and remain constant thereafter. As expected, the speed of the incident wave velocity remains constant during the experiment. The small variation in the speed of the incident wave can be attributed to the energy of the striker at the moment of the impact with the

chain. Variation in energy results in different momentum transferred to the chain which, in turn, affects the amplitude and speed of the generated solitary waves [4,7,29].

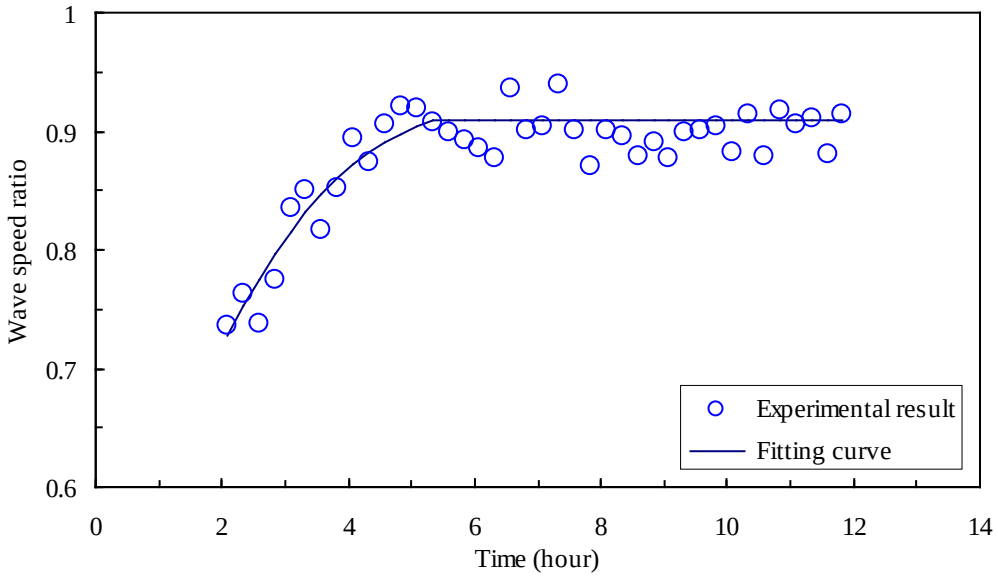

Figure 5.17. The speed ratio of the incident HNSW to PSW

In order to normalize any effect associated with the variation of the incident wave speed, we computed the ratio of the wave speed of the incident HNSW to that of the PSW. Such ration is shown in Figure 5.17 as a function of the concrete age. Based on the figure, the speed ratio increases by approximately 30% over the first 300 minutes and then remains constant as the hydration progresses.

The variations of the ARP and the ARS as a function of the cement age are shown in Fig. 10. While the amplitude ratio of the primary wave shows increases with concrete age (green crosses), the ARS exhibits a relatively complex behavior (blue circles). By comparing the results

shown in Figure 5.18 with the resistant pressure shown in Figure 5.15, it is worth noting that the amplitude of the primary reflected wave has a three-fold increase within the first 300 minutes and then it flats when the initial set occurred. As such, the amplitude of the reflected primary wave can also be used to determine the initial set of concrete.

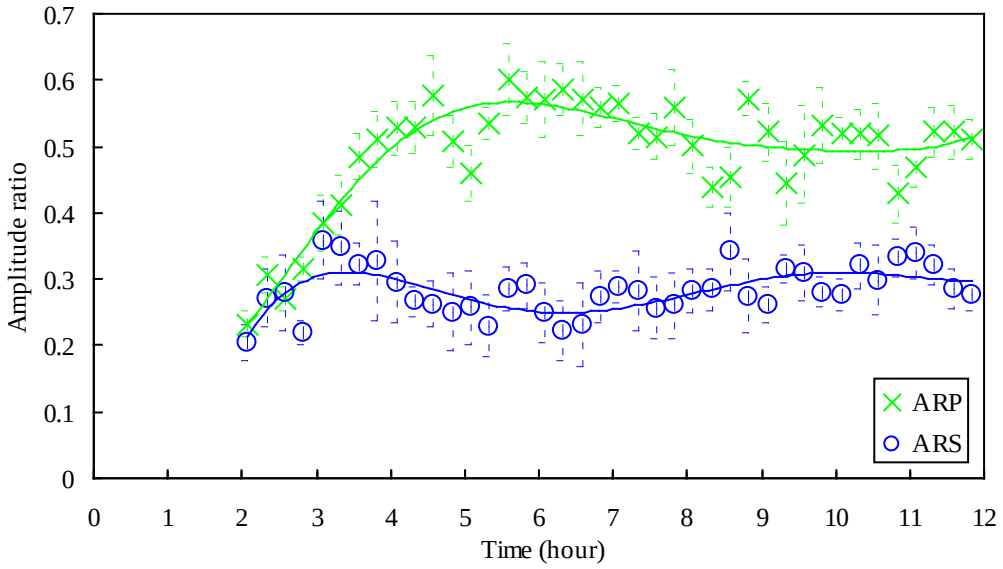

Figure 5.18. Experimentally measured ARP and ARS

5.3.4 Conclusions

This section describes a novel NDE method based on the propagation of HNSWs to estimate the initial and final set of fresh concrete. To prove the effectiveness of such methodology a concrete sample was monitored during hydration by using a cost-effective actuator/sensor made of a chain of spherical particles and an electromagnet was used for the generation and detection of the

HNSWs. and the reflected waves properties were used to predict the initial and final set of the concrete. It was found that a single pulse perpendicularly incident to the actuator/cement interface results in a series of reflected pulses, categorized into PSW and SSW. The amplitudes and TOFs of these two reflected waves are strongly dependent on the stiffness of the sample. The trend of the HNSWs characteristics were compared to the penetration resistance obtained from the ASTM C 403 [85] performed on mortar samples from the same mixture. As the concrete became stiffer, the TOF of both the PSW and SSW decreased continuously. Two transition points were observed in the trend for the TOF with time. These points approximately corresponded to the times of initial and final set established by the ASTM C 403 test [85].

The nondestructive approach proposed here can provide unique advantages over conventional methods based on linear ultrasonic bulk waves. In fact, the present approach requires only one transducer (instead of at least two) and it allows simpler access to the test specimen. With respect to the wave reflection method, where only the reflection coefficient is affected by the cement age, the present approach can virtually exploit three parameters: 1) the TOF of PSW, 2) the TOF of SSW, and 3) the ARP. Moreover the HNSW-based method does not require the use of electronics for the generation of high-voltage input signals, contrary to piezoelectric transducers. It is acknowledged that the method presented in this section implies that hydration is uniform in the whole material, by providing "effective" materials properties near the surface. If hydration conditions are such that the mechanical properties of the material in the near field, i.e. close to the actuator, are significantly different than in the far field, the HNSWs-based features may not be representative of the whole structure.

Overall, the initial work discussed in this section shows that the proposed technique has a promising potential in characterizing the time-dependent strength-development in hydrating concrete. Based on the results shown in this section, it appears that the NDE method is able to identify the initial and final set characterized by the ASTM C 403 [85].

5.4 CURING MONITORING OF TWO TON EPOXY BY HNSW

In this section we proposed the use of HNSWs to monitor the curing process of an adhesive layer utilized to bond two aluminum sheets. In the experiment a commercial 2 Ton Clear epoxy was used to bond two aluminum sheets. We monitored certain characteristics of the HNSWs such as time-of-flight and amplitude ratio of the reflected HNSWs and related them to the physical conditions of the adhesive layer.

5.4.1 Introduction

Adhesively-bonded components are widely used in a variety of modern industries and structures, including the automotive, aerospace, maritime, and civil [59,108-110]. These structures span from microchips to ships and large aircrafts, which are made of materials arranged in layers through adhesive bonding [110]. If there are manufacture defects in adhesively-bonded components (i.e. improper curing of adhesive, undesirable adhesive mixing), these defects may lower the strength of the components or shorten the service life under cyclic loadings. The NDE

methods able to assess the condition of adhesive for quality control are required. Here, we monitored the curing process of 2 Ton Clear epoxy used to bond aluminum sheets with several different mixing designs by HNSWs.

5.4.2 Experimental setup

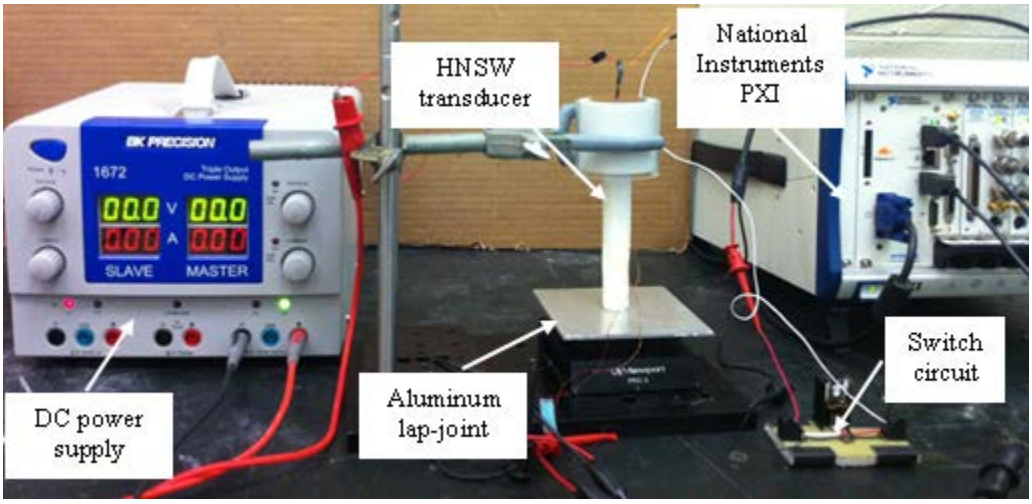

Figure 5.19. Experiment setup of the two ton epoxy curing monitoring test

To monitor epoxy curing, three specimens were prepared. Each specimen consisted of two 100 x 100 x 1.27 mm aluminum sheets bonded together using an ambient-cure Devcon "2 Ton Epoxy"© type. This was a two-part mixture with recommended resin/hardener volume ratio 1:1 and manufacturer's specified curing time of 16 hours. The resin/hardener ratios for the three specimens were 1:1, 2:1, and 4:1, respectively. Each plate was simply supported by four steel posts placed underneath the specimen 20 mm away from the specimen edges. For each monitoring the transducer was placed on the centroid of the aluminum joint immediately few

minutes after mixing the resin with the hardener. Ten measurements were taken every fifteen minutes for eight hours. Figure 5.19 shows the photo of the setup. The time history of the dynamic force measured by the sensor beads was sampled at 1 MHz.

5.4.3 Results and discussion

Typical waveforms obtained at 0 minute, 90 minutes, 180 minutes and 360 minutes are presented in Figure 5.20. It should be emphasized that *t=0* refers to the instant of the first measurement, which occurred circa five minutes after mixing manually the resin with the hardener. The first pulse is the arrival of the incident solitary wave generated by the impact, whereas the second pulse represents the wave reflected at the interface with the linear medium. Qualitatively, Figure 5.20 suggests that the TOF decreased and the ARP increased as the epoxy cured.

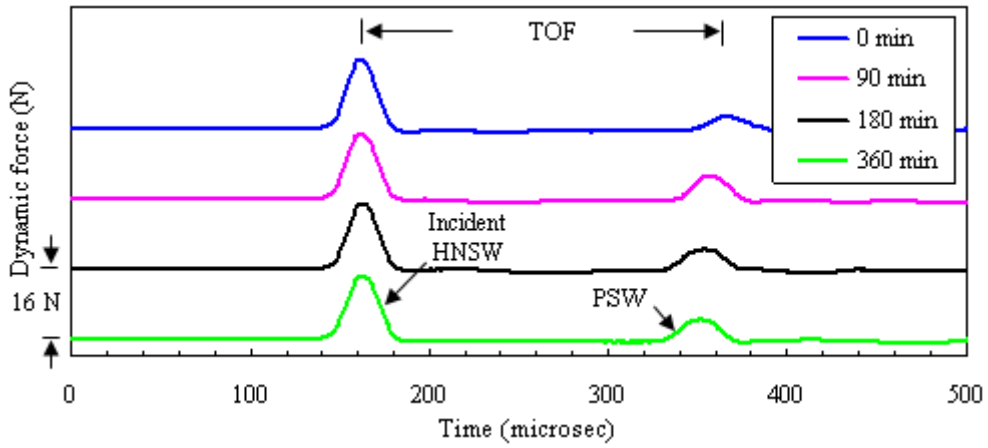

Figure 5.20. Typical waveforms at 0 minute, 90 minutes, 180 minutes, and 360 minutes

To quantify the effect of the curing process on the characteristics of the HNSWs, Figure 5.21 is presented. It shows the values of the TOF and AR as a function of the curing time. Both insets display the results from the three experiments. Each dot represents the average of the ten measurements taken at a given time. The TOFs for the mix ratios 1:1 (manufacturer's recommended value) and 2:1 decreased during the first three hours and then kept near constant. Instead, the TOF associated with the resin to hardener ratio 4:1 only decreased a little, which indicates the epoxy did not cured properly, at least not during the first 8 hours of the experiments. Overall, the value of the TOFs relative to the poor mix ratio are consistently higher than the values associated with the fair ratio which, in turn, were always higher than the TOFs of the 1:1 case.

By observing the data presented in Figure 5.21(b), the AR associated with the proper resin/hardener ratio increased from 0.16 to 0.32 during the first hour. Interestingly, the same two-fold increase was observed for the resin/hardener ratio 2:1. However, such an increase occurred over the first two hours, suggesting a slower kinetics of the curing. When the amount of resin was four times the amount of hardener, the amplitude of the reflected HNSW did not change significantly. This suggests that, within the monitoring window of 8 hours, the epoxy did not cure. Similar to what observed in Figure 5.21(a), the values of the ARs associated with the manufacturer's recommended ratio were always the largest, while the values of the 4:1 mix were always the smallest. This confirms that the characteristics of the HNSWs are dependent on the stiffness of the material underneath the HNSW transducer.

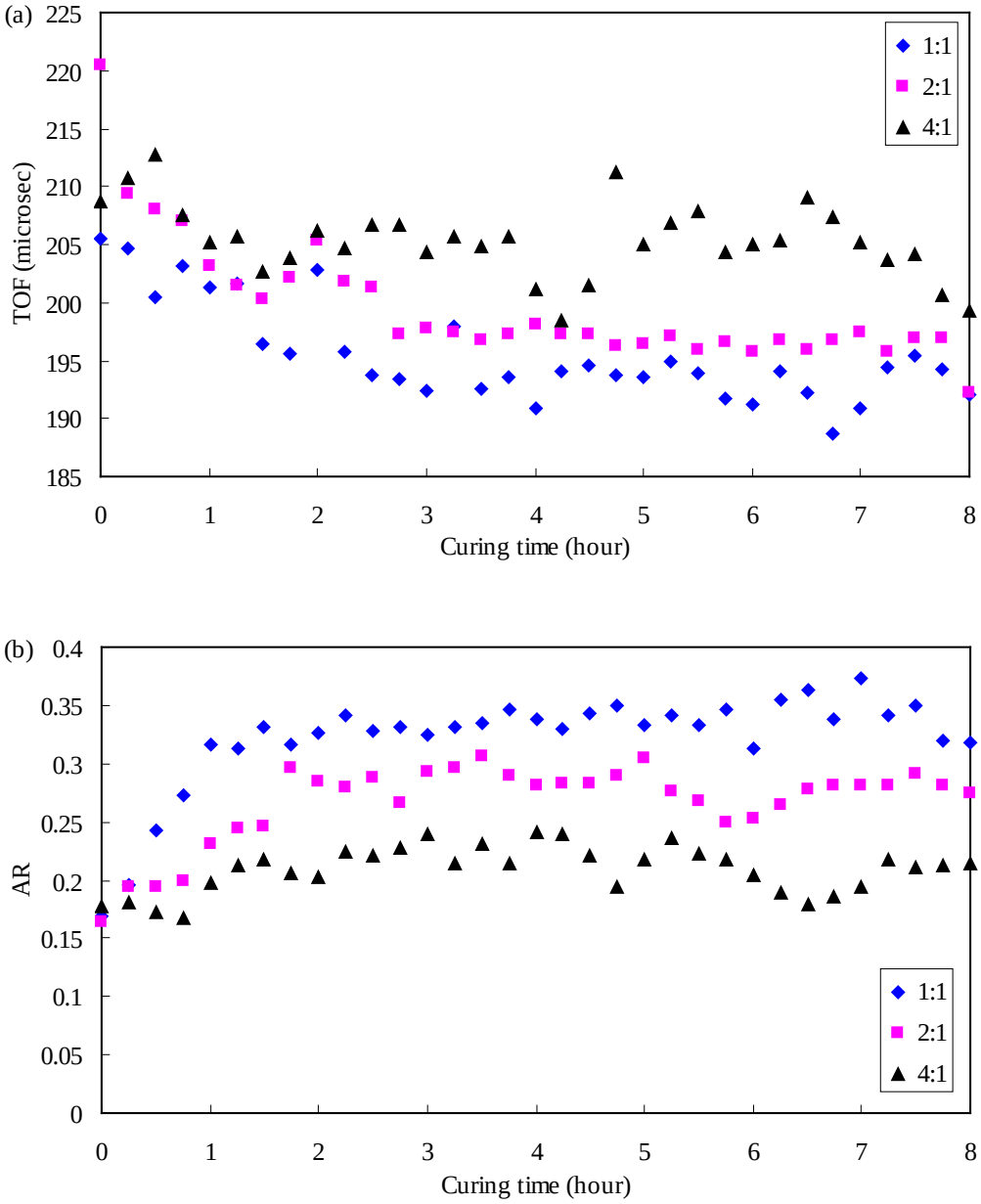

Figure 5.21. (a) TOF and (b) AR as functions of curing time

5.4.4 Conclusions

The HNSW transducer was used to monitor the curing process of tow ton epoxy consisting resin and hardener for different resin/hardener ratios. By observing the characteristics of the reflected pulse, we were able to monitor the change of the epoxy's strength and discriminate different resin/hardener ratios. In fact, the fastest and the slowest temporal variation of the HNSWs' characteristics were observed for the proper mix ratio (1:1) and the poor bond ratio (4:1), respectively.

5.5 ASSESSMENT OF BOND CONDITION BY HNSW

In this section, we assessed an aluminum lap-joint that possessed different bond conditions by the HNSW transducer.

5.5.1 Introduction

Adhesively-bonded components, if subjected to several cyclic loadings, may be prone to fatigue defects that may result in resin crazing, cracks, and disbond. Other defects that may be generated also during the assembling stage include voids, poor, adhesive strength, and poor cohesive strength. Due to the critical role of adhesively bonded joints, much effort has been devoted to the development of reliable, robust tools for the NDE and SHM of such structural elements. There are several methods for the NDE quality assessment of bonded structures [111]. These methods

include infrared thermography [112-114], radiography [115], acoustic emission [116], ultrasonic bulk and guided wave testing [59,117-121] and coin-tap method [122-129]. A brief review on adhesive bond strength determination has been presented by Lee Crane and Dillingham [130].

In the experiment, six types of bond quality were created on an aluminum lap-joint. The HNSW transducer was used to measure the time-of-flight and amplitude ratios of HNSWs to assess the bond condition.

5.5.2 Experimental setup

The capability of the HNSWs to assess the quality of adhesively-bonded components was evaluated by testing the aluminum lap joint schematized in Figure 5.22(a). The thickness of the Al T6061 adherents was 1.57 mm and their dimensions were 840 x 340 mm with a joint overlap of 80 mm. We adopted the same clear epoxy used in the experiment of precious section.

We engineered six different bond conditions distributed over twelve 80 x 60 mm regions. Zones 1 and 7 were bonded with a 1:1 resin/hardener volume ratio resulting in the "fully cured" (elastic) bond. Areas 2 and 8 were bonded using a mix ratio of 2:1 resulting in the "fairly cured" bond. In zones 3 and 9 we simulated slip interface by inserting a sheet of paper between the plates. Zones 4 and 10 were bonded with the resin/hardener ratio of 3:1, while zones 5 and 11 were bonded using a 4:1 ratio, resulting in a "poorly cured" bond, i.e. substantial degradation of the cohesive strength of the adhesive. Finally, in zones 6 and 12 we did not apply adhesive, resulting in a “no bond”.

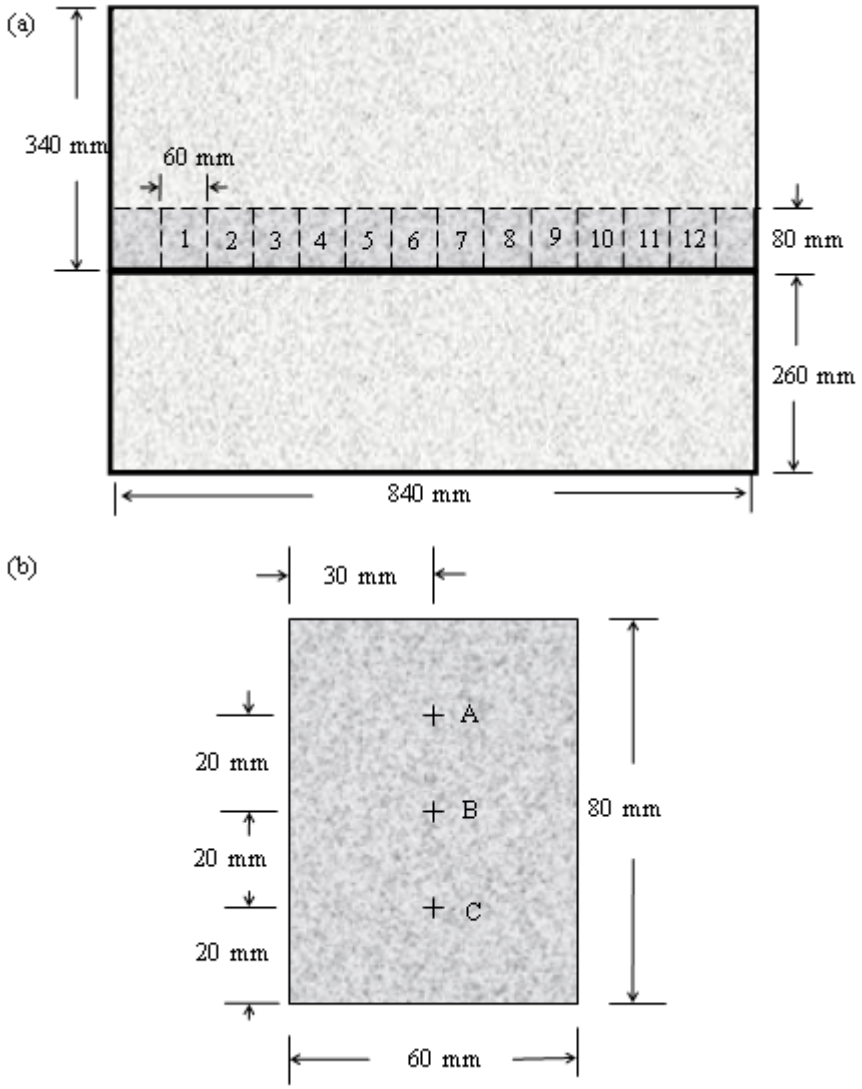

Figure 5.22. (a) Scheme of the tested aluminum lap joint with location and types of defects at the bondline. (b) Locations of the inspected points (A, B, and C) within each region

Each zone was inspected in three points, namely A, B, and C (Figure 5.22(b)). Ten measurements were taken at each inspection point, which are hereafter uniquely identified with a letter (A, B, or C) and a number (1 to 12). For instance, A6 denotes the test point located on the position A of zone 6. The measurements were taken 36 hours after the lap-joint was created.

5.5.3 Results and discussion

Figure 5.23 shows the force profiles measured at points B1 (fully cured bond) and B6 (no bond). Two pulses are visible. The first pulse is the incident HNSW generated by the impact of the striker and directed towards the joint. The second pulse is the primary wave reflected at the interface. The force profiles suggest that both the TOF and the amplitude of the reflected pulse are affected by the bond condition. In fact, the reflected HNSW is faster and stronger when the resin and hardener are properly mixed. Good bond should create a stiffer interface, which, in turn, induces stronger repulsions of the HNSW pulse at the interface, where the granular particle-based actuator interacts with the underlying system.

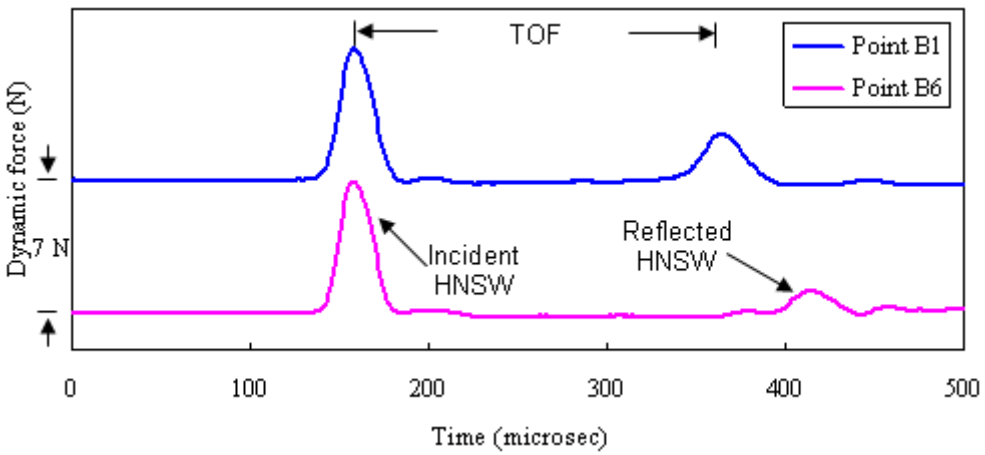

Figure 5.23. Typical waveforms obtained at zone 1 and zone 6

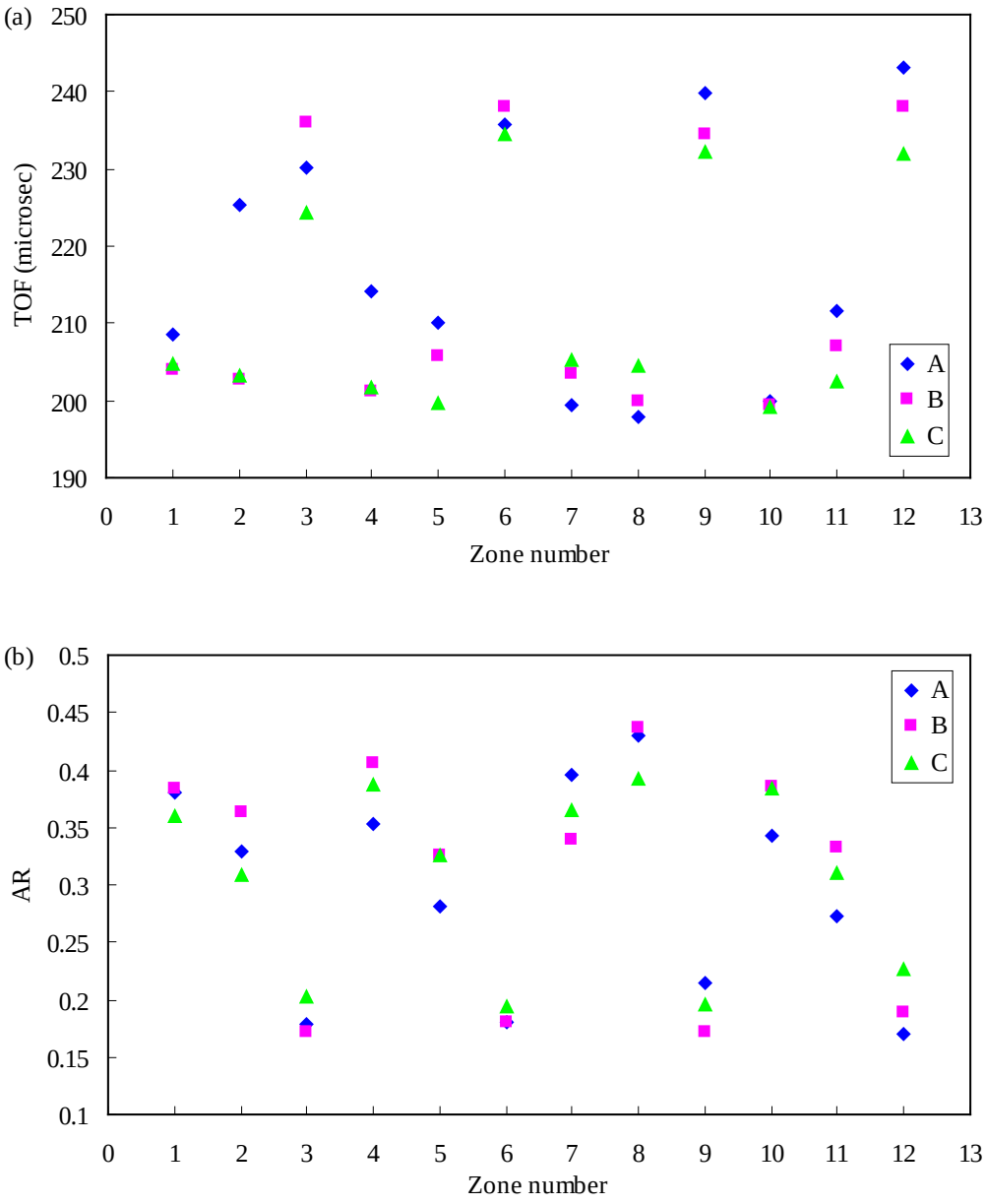

Figure 5.24. (a) average of TOF and (b) average of ARP for all data at 36 inspection points from 12 zones

Figure 5.24 shows the averages values of the ten testing data associated with the TOF and the AR taken from all 36 test points. Figure 5.24(a) demonstrates that the TOF is able to clearly

separate the adhesively bonded zones from non-adhesively bonded zones. On average, the TOF associated with the lack of adhesive is 15% higher that the values associated with good or fair bond conditions. Similar considerations can be made for the AR data presented in Figure 5.24(b). For this HNSW feature, the difference between adhesively bonded and lack of bonding area is larger and in the order of 50%. Unfortunately, the features selected here were unable to discriminate the fair and poor bond from the good bond.

To discriminate different bond conditions, we used an outlier analysis algorithm. This is the first time, to the best of the authors' knowledge that an outlier analysis is applied to HNSW-based data. An outlier is a datum that appears inconsistent with a set of data, the baseline that describes the normal condition of the structure under investigation. In the analysis of one-dimensional elements, the detection of outliers is a straightforward process based on the determination of the discordancy between the one-dimensional datum and the baseline. One of the most common discordancy tests is based on the deviation statistics, z_ζ, defined as

$$z_\zeta = \frac{x_\zeta - \bar{x}}{\sigma} \tag{5.16}$$

where x_ζ is the potential outlier, and $\bar{x}$ and σ are the mean and the standard deviation of the baseline, respectively [35]. The mean and standard deviation can be calculated with or without the potential outlier, depending upon whether inclusive or exclusive measures are preferred.

A set of *p*-dimensional (multivariate) data consists of *n* observations in *p* variables. The discordancy test equivalent to Equation (5.16) is expressed by the Mahalanobis squared distance (MSD), D_ζ, which is a non-negative scalar defined as

$$D_\zeta = (\{x_\zeta\} - \{\bar{x}\})^T \cdot [K]^{-1} \cdot (\{x_\zeta\} - \{\bar{x}\}) \quad (5.17)$$

where $\{x_\zeta\}$ is the potential outlier vector, $\{\bar{x}\}$ is the mean vector of the baseline, [*K*] is the covariance matrix of the baseline, and T symbolizes the transpose operation. Both vectors $\{x_\zeta\}$ and $\{\bar{x}\}$ are p-dimensional, whereas [*K*] is a square matrix of order *p*.

A datum is an outlier if the corresponding value of z_ζ or D_ζ falls above a set threshold. In the one-dimensional outlier analysis, there is a 98% probability that a sample x_ζ drawn from the same distribution of baseline data will lie in the range [-2.33, 2.33] when the baseline data are assumed to be normally distributed. In order to determine whether a new uni-dimensional or multi-dimensional datum is an outlier, the corresponding value of z_ζ or D_ζ has to be compared to a threshold. The threshold value can be taken as the upper value of $n\sigma$ equal to a certain Gaussian confidence limit [131-132] or a Monte Carlo simulation [133].

The results of the outlier analysis are presented in Figure 5.25(a) and Figure 5.25(b) refer to the univariate analysis and are associated to the TOF and the AR, respectively. Figure 5.25(c) reports on the multivariate analysis where a 2-D vector was considered. This vector contains the data from the two HNSW features shown in Figure 5.25(a) and Figure 5.25(b). The vertical dashed lines bound the regions with the different types of bond. Each region contains the 30 measurements from points A, B, and C. The horizontal line represents the threshold, which was

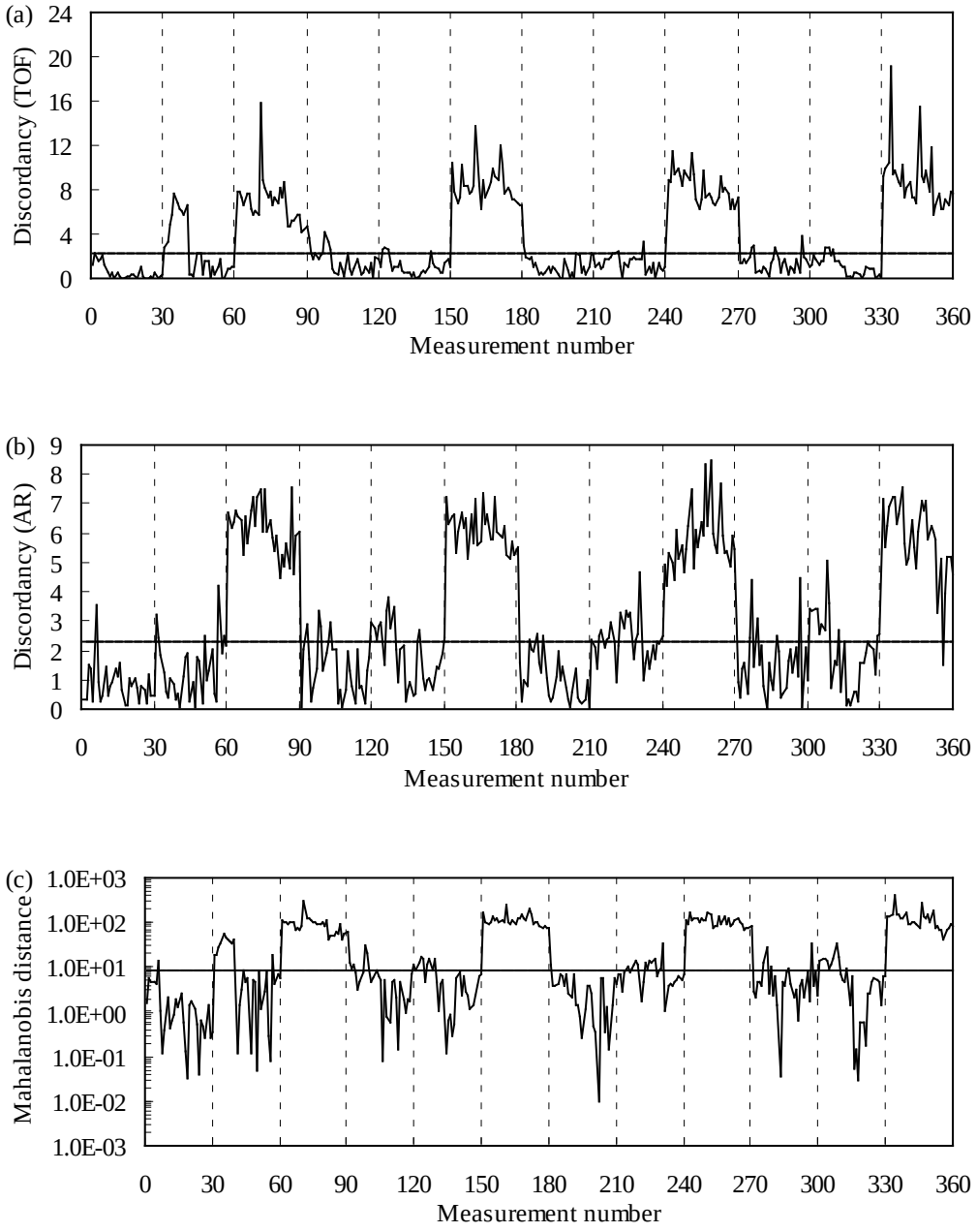

Figure 5.25. Outlier analysis. (a) Discordancy test for TOF; (b) Discordancy test for AR; (c) Mahalanobis squared distance for two-dimensional data (TOF and AR)

computed by applying the Monte Carlo method. Specifically, for the multivariate analysis we constructed n (=60) x p (=2) matrix with each element being a randomly generated number from

a zero mean and unity standard deviation Gaussian distribution. The MSD were calculated for all the elements, using equation (2) where $\{\bar{x}\}$ and $[K]$ are inclusive statistics. This process was repeated for 10,000 trials whereupon the array containing all the MSD was ordered in terms of magnitude. The 60 measurements from the mix ratio 1:1 regions represented the baseline. We choose the threshold as the 98% probability that a sample x_ζ is drawn from the same distribution of baseline data, which is assumed to be Gaussian distribution.

Anytime baseline samples exceed the threshold, they classify as outliers. In the context of the present framework, these values represent false indications of damage, i.e., false positives. Conversely, anytime a datum associated with a defect is below the threshold, it is classified as a false negative.

Table 5.2. Outlier analysis. Percentage of outliers detected by using 60 baseline data and Monte Carlo simulation

Zone	1	2	3	4	5	6	7	8	9	10	11	12
Bond condition	1:1	2:1	slip	3:1	4:1	no	1:1	2:1	slip	3:1	4:1	no
TOF	0	33	100	13	13	100	3.3	6.7	100	13	10	100
AR	3.3	17	100	17	33	100	10	50	100	17	40	97
MSD	0	33	100	13	13	100	3.3	6.7	100	13	10	100

The percentage of outliers identified for each region is summarized in Table 5.2. The analysis properly identified damage in the most critical regions, i.e. those that do not have any epoxy. Moreover, the difference among the mix ratios 2:1, 3:1, and 4:1 in terms of success rate seems marginal.

Table 5.3. Outlier analysis. Percentage of outliers detected by using 30 baseline data and Monte Carlo simulation

Zone	1	2	3	4	5	6	7	8	9	10	11	12
Bond condition	1:1	2:1	slip	3:1	4:1	no	1:1	2:1	slip	3:1	4:1	no
TOF	0	30	100	10	0	100	3.3	3.3	100	6.7	0	100
AR	3.3	20	100	17	40	100	3.3	27	100	13	50	97
MSD	3.3	37	100	10	30	100	0	30	100	13	33	100

As the outlier analysis can be conducted by using slightly different approaches, we computed the number of outliers by applying the same Monte Carlo simulation but considering 30 baseline data, instead of 60. These data were the first five measurements from points A1, B1, C1, A7, B7, and C7. The results are summarized in Table 5.3.

Table 5.4. Outlier analysis. Percentage of outliers detected by using 30 baseline data and threshold taken as the 98% of the Gaussian confidence limit

Zone	1	2	3	4	5	6	7	8	9	10	11	12
Bond condition	1:1	2:1	slip	3:1	4:1	no	1:1	2:1	slip	3:1	4:1	no
TOF	0	30	100	10	0	100	3.3	3.3	100	6.7	0	100
AR	3.3	20	100	17	40	100	3.3	27	100	13	50	97
MSD	3.3	37	100	10	30	100	0	30	100	13	33	100

Finally, once the values of z_ζ and D_ζ of the baseline distribution were determined, the threshold value was taken as the 2.33σ equal to 98% of the Gaussian confidence limit, i.e. the

threshold was computed as the average value + 2.33σ. The baseline data were the first five measurements from each inspection point at the region with 1:1 mix ratio. For this approach the percentage of detected outlier is summarized in Table 5.4. By comparing the overall results presented in Table 5.2 and Table 5.3, the latter approach seems to provide the best results in term of number of outliers properly identified.

In the attempt to operate a classification between zones with and without adhesive the Naïve-Bayes classifier was also used. We used the following procedure:

(1) The first five measurements, in terms of TOF and AR, taken at each inspection point of every zone were considered to train the classifier.

(2) Two classes were created: C_1 relative to adhesively-bonded zones; C_2, relative to either slip or no bond conditions. Given a testing datum X, the classifier calculate the highest posterior probability, conditional on X. That is the Naïve-Bayes classifier predicts that the sample X belongs to the class C_1 if and only if

$$P(C_1|X) > P(C_2|X) \tag{5.18}$$

where $P(C_1|X)$ is the conditional probability of sample belonging to class C_1 on X.

(3) Using the Bayes's theorem

$$P(C_i|X) = \frac{P(X|C_i)P(C_i)}{P(X)} \quad , \quad i = 1,2 \tag{5.19}$$

where $P(X)$ is constant for all classes, $P(C_i)$ can be estimated by

$$P(C_i) = \frac{num(C_{i,D})}{num(D)} \tag{5.20}$$

where $num(C_{i,D})$ is the number of samples of class C_i in the whole set D, and $num(D)$ is the total number of samples in the whole set D.

(4) Assuming the experimental results on TOF and AR are normally distributed, then maximize the conditional probability $P(C_i|X)$.

(5) The last five measurements, in terms of TOF and AR, taken at each inspection point of every zone were used as testing data to test the performance of the classifier.

The values of the five testing data of the TOF and the AR taken from all 36 test points are presented in Figure 5.26. Figure 5.26(a) demonstrates that the TOF is able to clearly separate the adhesively bonded zones from non-adhesively bonded zones. On average, the TOF associated with the lack of adhesive is 15% higher that the values associated with good or fair bond conditions. The value of the red lines in Figure 5.26(a) is around 219.85 μs which is the Naive-Bayes classifier [134]. If the TOF is less than 219.85 μs, the testing data will be classified as good or fair bond, if the TOF is greater than 219.85 μs, the testing data will be classified as slip or no bond. All 5 testing data from A2 were misclassified, the reason may be that during the test, the epoxy leaked from the boundary near A2, thus the real bond condition might be quite different from experimentally designed. Only 1 testing data from A4 out of all other 175 measurements were misclassified, the performance of the classifier is quite good.

Similar considerations can be driven for the Naïve-Bayes classifier applied to the AR data shown in Figure 5.26(b). For this HNSW feature, however the difference between adhesively bonded and lack of bonding area is larger and in the order of 50%. The value of the

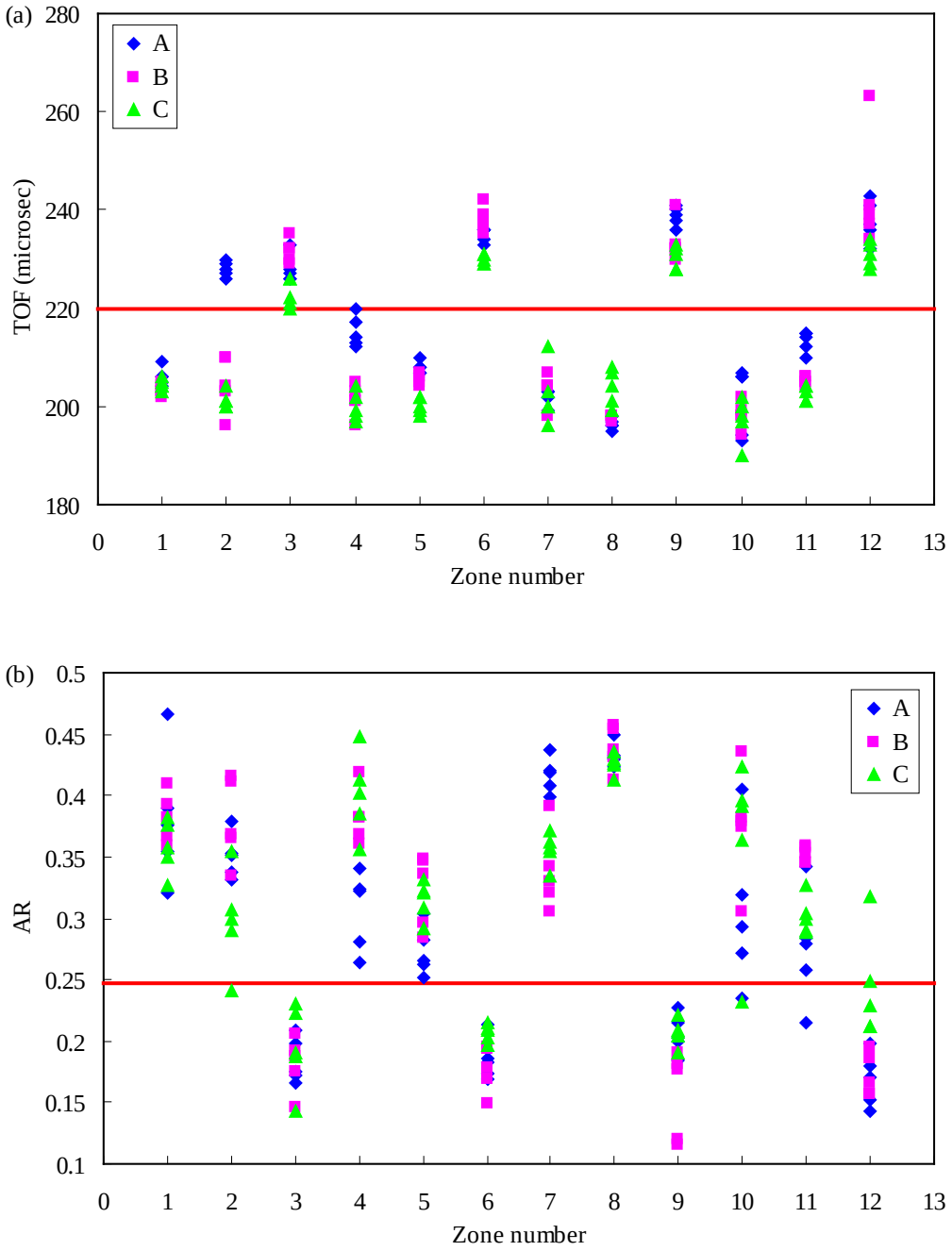

Figure 5.26. (a) TOF and (b) ARP for 180 testing data at 36 inspection points from 12 zones

red line in Figure 5.26(b) is equal to 0.2474. If the AR is greater than 0.2474, the testing data will be classified as associated with the adhesively bonded zones. If the AR is less than 0.2474, the testing data will be classified as associated with the non-adhesively bonded zones. Only 6 testing data from zone 2, zone 10, zone 11 and zone 12 out of 180 testing data were misclassified. Unlike the TOF, AR was able to classify the 5 testing data from A2 correctly even the real bond condition near A2 was different from the bond condition designed. Again, the performance of the classifier is quite good.

Assuming the experimental results of TOFs and ARs are normally distributed, the Naïve-Bayes classifiers give smallest classification error rate. We also tried to get the Naïve-Bayes classifier with 3 classes, namely good bond (1:1 resin/hardener ratio), poor bond (2:1, 3:1, 4:1 resin/hardener ratio), and slip/no bond. However, the difference between mean values of TOFs and ARs for good and poor bonds is much smaller compared to the standard deviations of TOFs and ARs for good and poor bonds, thus good bond condition could not be discriminated from poor bond conditions by Naive-Bayes classifier. Similarly, slip bond and no bond could not be distinguished if we used more classes. Moreover, the fact that the lap-joint was not simply supported but placed on a rigid structure might have made the overall mechanical impedance too high.

5.5.4 Conclusions

The same HNSW features were able to discriminate good bond and fair bond from slip and disbond conditions in the aluminum lap-joint. However, neither the amplitude of the reflected

wave nor the TOF were able to clearly discriminate good bond from fair and poor bonds. To enhance the capability to discriminate the different mix ratios used in this study, we applied an outlier analysis algorithm and Bayesian analysis. The results showed some improvement but not such that mix ratios other than that recommended by the manufacturer could be clearly discriminated.

The results of the present experiment seem to contradict the successful outcomes of the experiment described in the previous section. It is noteworthy that the structure inspected in this experiment was bulkier. Moreover the lap-joint laid on a rigid table. As such, future may analyze the effect of boundary conditions on the performance of the HNSW-based NDE method proposed here.

5.6 DEMAGE DETECTION IN COMPOSITE PLATES BY HNSW

5.6.1 Experimental setup

In the last experiment the composite plate shown in Figure 5.27 was inspected using the HNSW transducer. The composite plate is 600 mm long, 300 mm wide and 0.8 mm thick and made of carbon fiber (from McMASTER-CARR, part no. 8181K32). The plate was damaged by means of low and medium impact forces. A total of 12 points where inspected. Eight points where associated with pristine plate while four points were related to impact points 9 – 12. To create damage, some weights were attached to a stainless steel ball and they were released at certain

heights to impact the composite plate. Table 5.5 summarizes the weights and falling heights for creating impact damage at point 9 – 12.

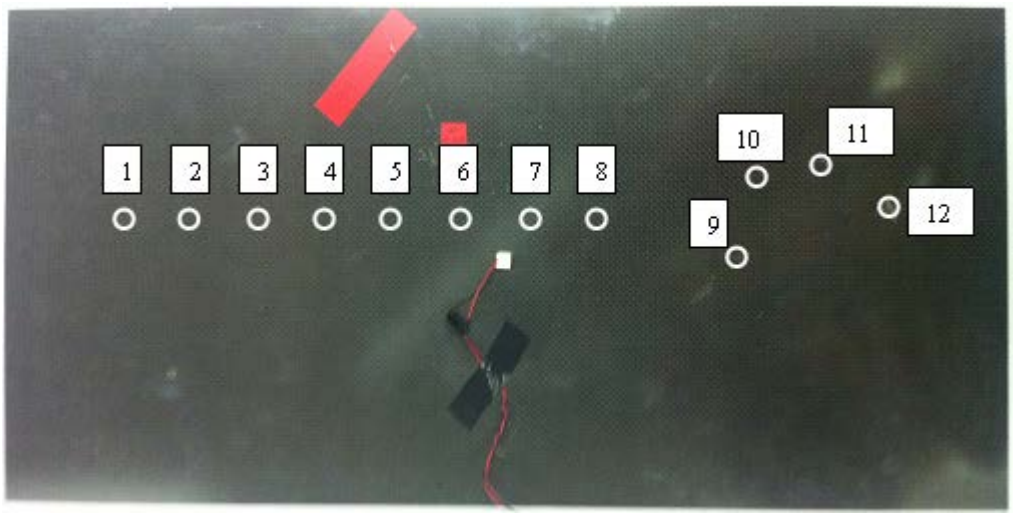

Figure 5.27. Composite plate with impact damage. The centers are the test points 1-12

Table 5.5. The weights and falling heights for creating impact damage

Impact point	9	10	11	12
Weight (kg)	0.528	0.528	0.528	1.028
Height (m)	1.8	2.1	2.1	2.23

Figure 5.28 shows the experimental setup of the detection of impact damage in composite plate test. For each test point, ten measurements were made, then TOFs and ARs were calculated from the recorded waveforms.

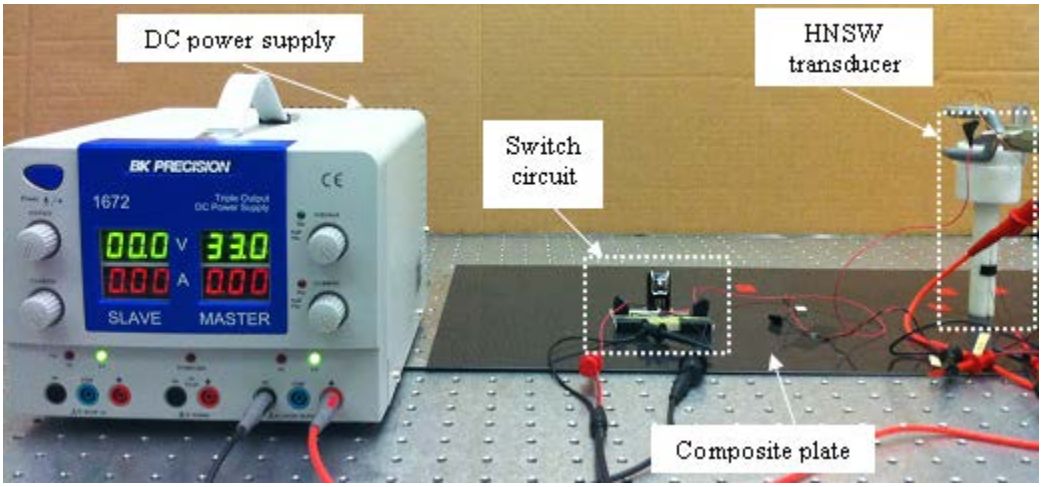

Figure 5.28. Photo of experimental setup for detecting impact damage in composite plate

5.6.2 Results and discussion

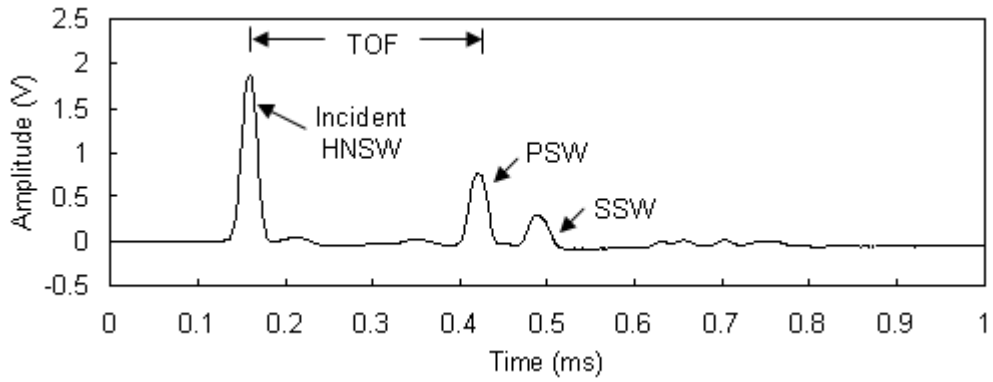

Figure 5.29. Typical waveform obtained from the pristine composite plate

Figure 5.29 shows the time waveform recorded by the top sensor bead when the actuator inspected a pristine zone. As for the concrete test, the presence of two reflected waves is visible. The values of the TOFs of PSW and SSW at the twelve points are presented in Figure 5.30. From

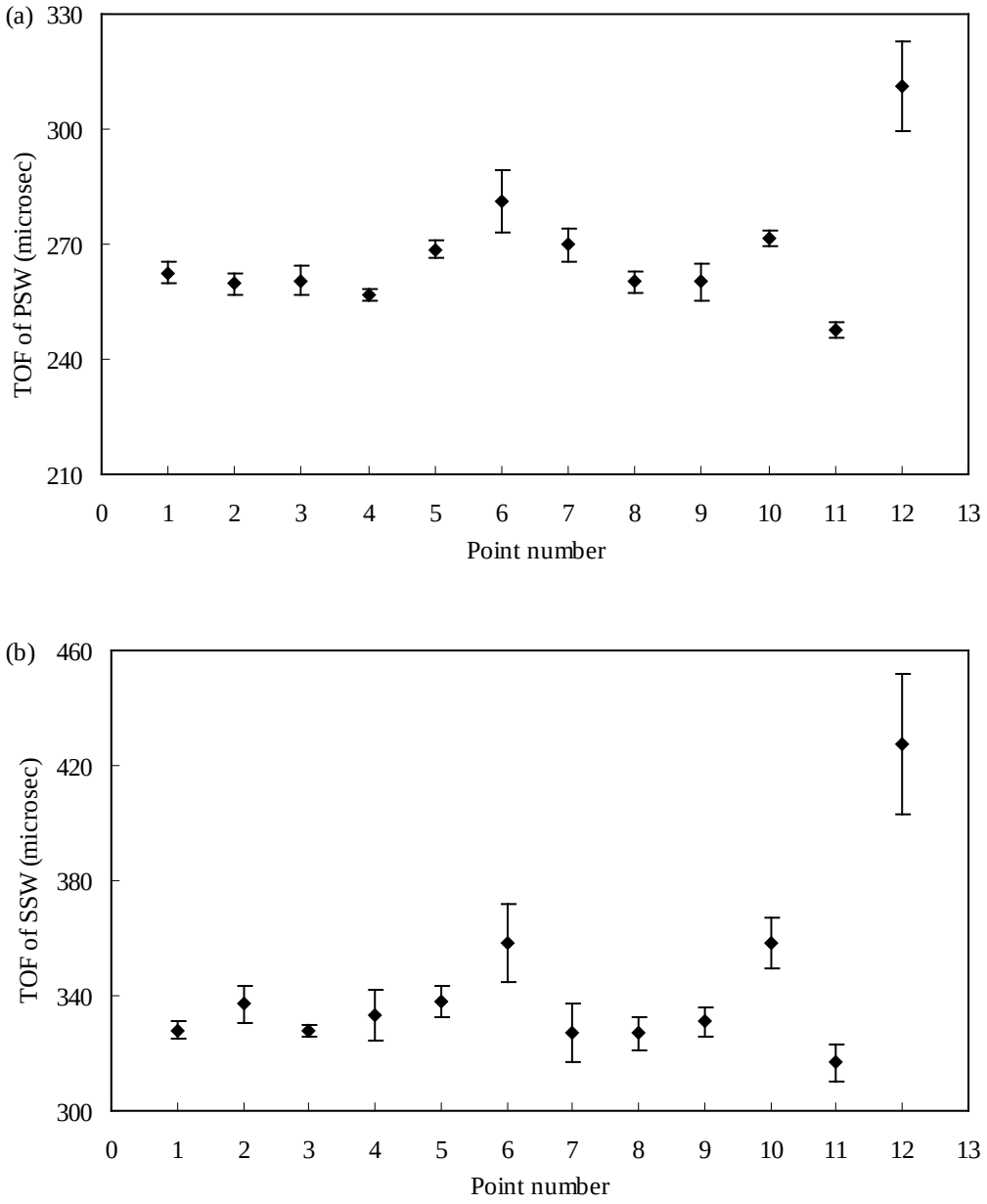

Figure 5.30. HNSW features for test points on the composite plate. (a) TOF of PSW (b) TOF of SSW

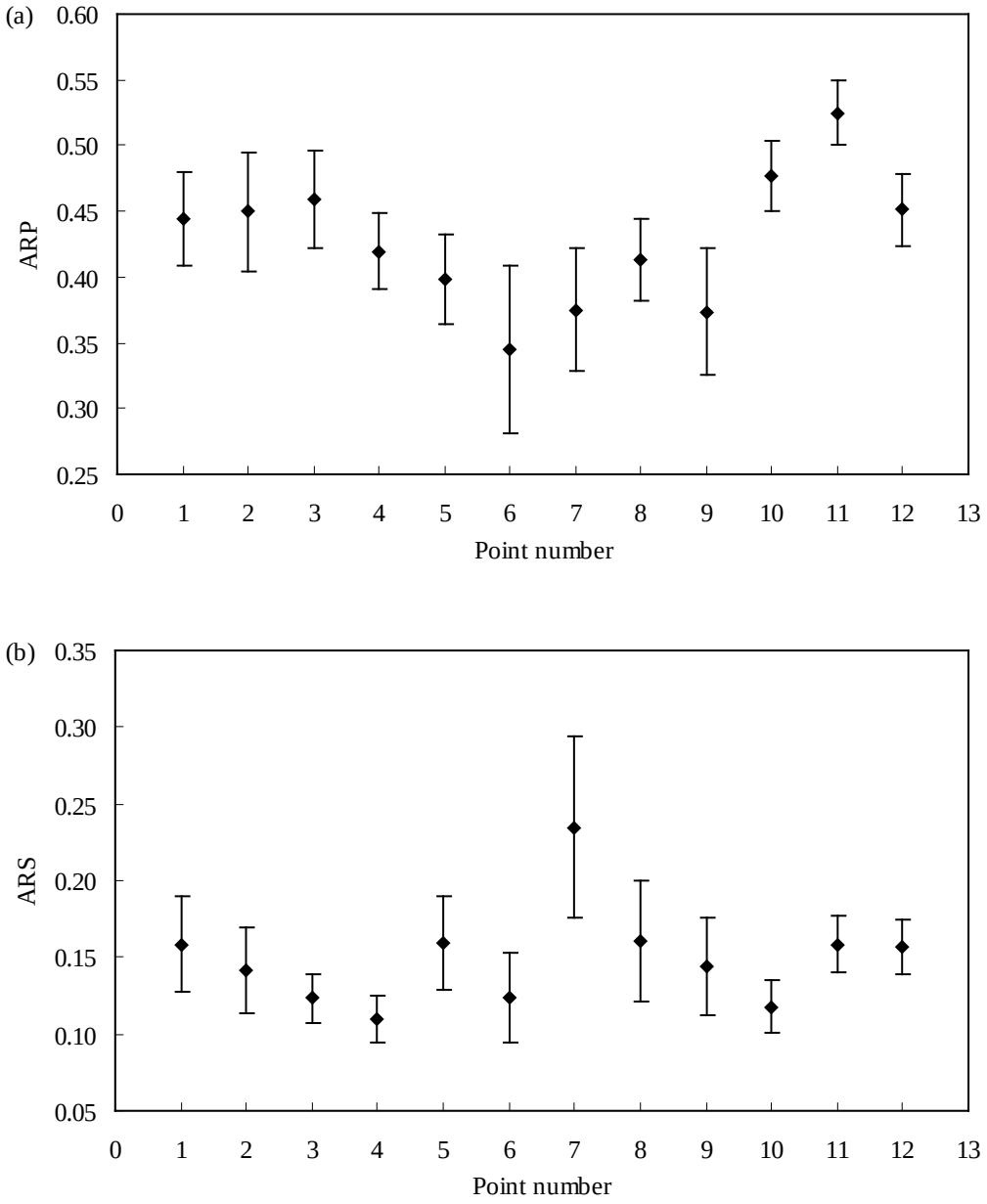

Figure 5.31. HNSW features for test points on the composite plate. (a) ARP (b) ARS

Figure 5.30, it can be seen that the TOFs of PSW and SSW of point 11 are slightly smaller than other points and the TOFs of PSW and SSW of point 11 are obviously larger than other points. For point 11, the test point was at the center of a round dent in which the surface is flat and smooth, the impact might result in a slight increase in stiffness in the small area. For point 12 which is the most severe damage, it can be clearly seen that there were visible cracks and the surface was rough and that might cause the stiffness of the composite plate surface decreased significantly. Therefore, the TOFs of PSW and SSW at point 12 are much larger than others. Other damaged areas were not discriminated, probably because the changes of stiffness caused by the damage were not sufficiently large. The values of the ARP and ARS at the twelve points are presented in Figure 5.31. From Figure 5.31, it can be seen that the ARP and ARS from damaged points and undamaged points do not have significant differences to be separated. Again, it is probably because the changes of stiffness caused by the damage were not sufficiently large.

5.6.3 Conclusions

The composite plate with impact damage was inspected by the HNSW transducer, the transducer was only able to detect some of the damage, the reason might be that some damage did not result in stiffness difference which is large enough to be detected or the results mainly depended on the surface condition.

6.0 APPLICATION OF HNSW FOR ACOUSTIC LENS

The acoustic lens is a device that can be used to focus sound. Currently, the performance of acoustic lenses is limited by their linear operational envelop, which results in relatively inaccurate focusing and low focal power [45]. Spadoni and Daraio [45] introduced a nonlinear acoustic lens which consists of ordered arrays of granular chains. The proposed nonlinear acoustic lens was studied both numerically and experimentally, and the results demonstrate the focusing effect. In this chapter, the pilot study on the design and development of a low-cost and easy-to-make nonlinear acoustic lens is presented.

6.1 PRINCIPLE OF NONLINEAR ACOUSTIC LENS

Let us consider a two-dimensional array of chains of elastic beads which can support the generation and propagation of HNSWs are in contact with a linear medium. It is possible that if the HNSWs in different chains impact the linear medium at different time, all the wavefronts arrive at certain location in linear medium at the same time, the stress waves are focused [50]. Generally, the bulk wave speeds in linear materials are considered as constants. The chains' locations and the instants when the HNSWs in different chains hit the linear medium can be

controlled. Figure 6.1 shows the schematic of the wave field in the linear medium when the waves generated by chains are focused at a focal point (x_0,y_0).

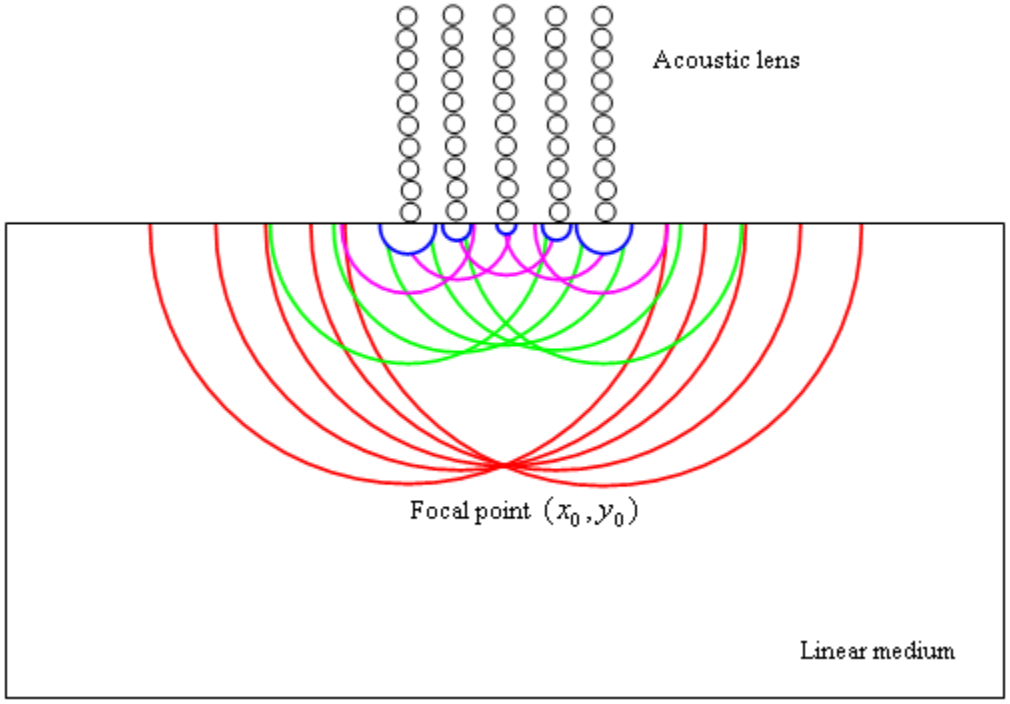

Figure 6.1. Schematic of the wave field in the linear medium shortly after the HNSWs impacts, color lines denote the wavefronts at different instants

For simplicity, assuming the chains of elastic particles are excited simultaneously, the focusing can be achieved by tuning the wave speeds and arranging the positions of chains properly. According to Equation (2.19), tunability of the speed of HNSWs can be achieved by changing the initial precompression and dynamic contact force or changing the size and material of the beads. In next Section 6.2, three different schemes will be used to tune the acoustic lens.

6.2 PILOT NUMERICAL STUDY

In this section, three numerical examples are given to show three possible ways to tune the acoustic lens.

6.2.1 Description of the problem

15 chains of elastic beads are vertically oriented and are in contact with a container filled with water, the dimension of the container is large enough such that no reflections from the boundaries need to be considered. The goal is to use the array of chains as an acoustic lens to focus the impacts on the chain at a focal point 0.1 m under the contact point between the middle chain and water. The diameter of the beads is 4.76 mm, and there are 20 beads in each chain.

6.2.2 Tuning acoustic lens by changing material of beads

6.2.2.1 Scheme I

In scheme I, the material of beads, the locations of the chains, and the dynamic contact forces on the chains are predefined, the focusing effect is achieved by tuning the initial precompression on the chains. For example, all the chains are equally spaced with the distance 9.52 mm, all the beads are made of stainless steel, the dynamic contact forces in all chains are equal to 10 N, and the middle chain is only subjected to gravity-induced precompression. The total traveling time along chains and paths in the linear medium should be the same. From the geometrical relation,

the speeds in each chain can be obtained. Then using Equation (2.19), the precompression in the each chain (except the middle chain in which the precompression has been already predefined) can be obtained by solving a high-order equation which has only one positive solution in this case. Table 6.1 shows the precompression applied on the chains. Chain 1 is the middle chain and only half of other chains are shown here because of the symmetry. Chain 2 is the nearest chain to the middle chain and Chain 8 is the farthest chain from the middle chain.

Table 6.1. Precompression applied on the chains and wave speed in the chain

Chain number	Precompression (N)	Wave speed (m/s)
1	0.045	514.8
2	0.047	515.1
3	0.055	516.3
4	0.069	518.2
5	0.092	520.8
6	0.125	524.2
7	0.172	528.3
8	0.236	533.1

6.2.2.2 Scheme II

Table 6.2. Mechanical properties of materials used in this numerical example

	Young's modulus (GPa)	Density (Kg/ m^3)	Poisson's ratio
Aluminum	70	2700	0.35
Titanium	116	4506	0.32
Iron	211	7874	0.29
Stainless steel	193	8000	0.3
Nickel	200	8908	0.31
Zinc	108	7140	0.25
Copper	120	8940	0.34
Silver	83	1049	0.37

In scheme II, the chains are subjected only to gravity-induced precomperssion, the dynamic contact forces on the chains are all the same, the focusing effect is achieved by changing the materials of beads and placing the chains properly. If the dynamic contact forces are known, the wave speeds in the chains can be obtained using Equation (2.19), then the distance between certain chain and the middle chain can be calculated using the condition the traveling times for the waves to arrive at the focal point are the same. For different dynamic contact forces, different distances can be obtained. The mechanical properties of the materials used here are summarized

in Table 6.2. Figure 6.2 shows the distances from chains of beads made of different materials from the middle chain as functions of the dynamic contact force. The black line in Figure 6.2 overlapped with the *x* axis denotes the middle chain. Only 8 chains are shown here because of the symmetry. As shown in Figure 6.2, the chains are not equally spaced in this example.

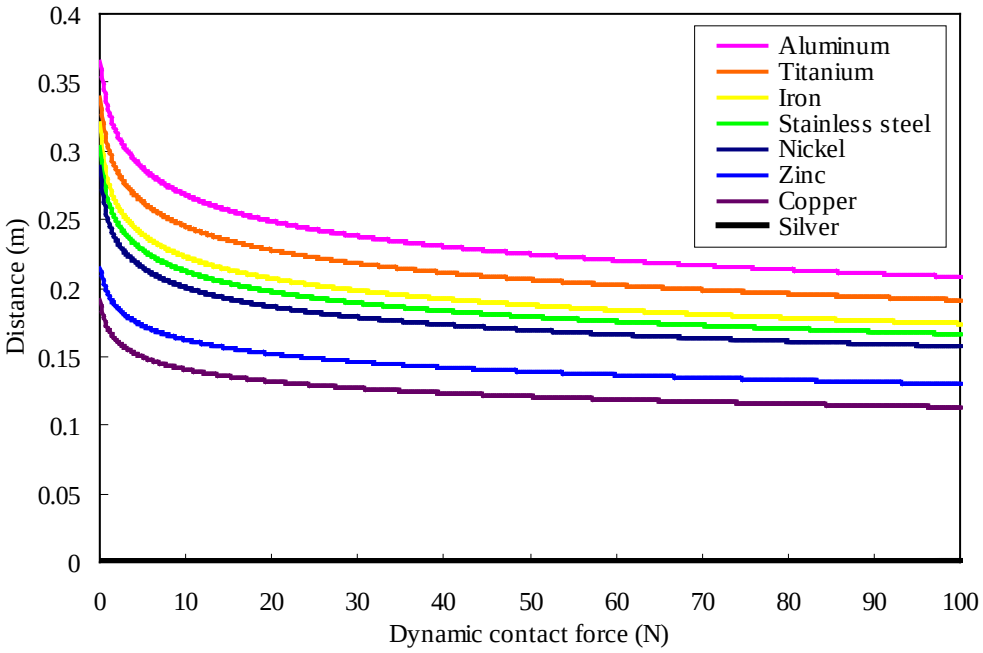

Figure 6.2. Distances from the chain made of certain material to the middle chain as functions of the dynamic contact force

6.2.2.3 Scheme III

In scheme III, the chains are still subjected only to gravity-induced precomperssion, the velocities of strikers are all the same. For all chains, the strikers are the same as the beads in the

chains. The focusing effect is achieved by changing the materials of beads and placing the chains properly. The wave speeds in the chains can be estimated as [3,51]:

$$V_s \approx 0.9145a\left(\frac{v_l A|_c^2}{m^2}\right)^{1/5} \tag{6.1}$$

where v_l is the velocity of the last particle and Chatterjee [10] found

$$v_l \approx 0.682V_k \tag{6.2}$$

where V_k is the velocity of the striker.

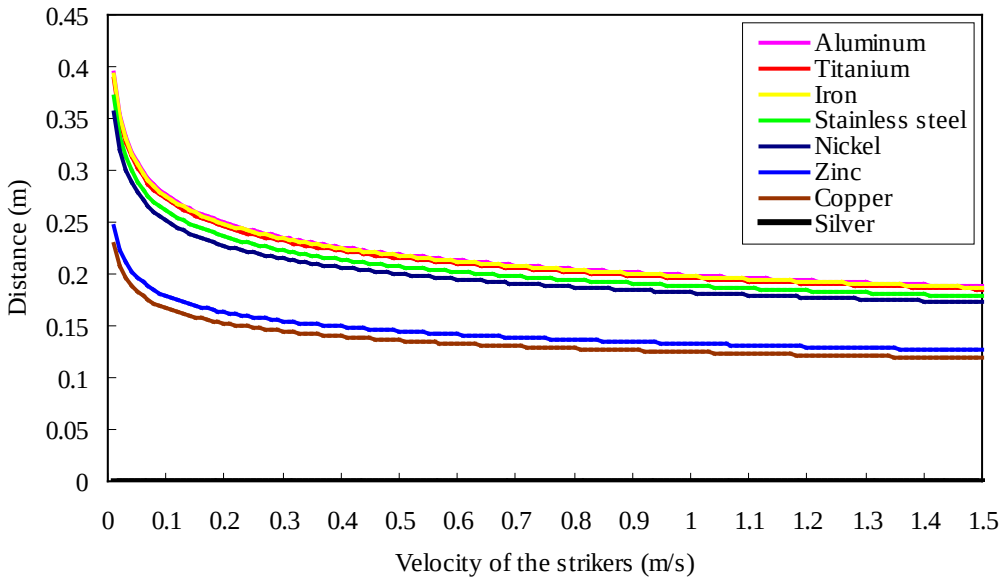

Figure 6.3. Distances from the chain made of certain material to the middle chain as functions of the velocity of the strikers

If the velocities of the strikers are known, the wave speeds in the chains can be estimated by Equation (6.1) and Equation (6.2), then the distance between certain chain and the middle

chain can be calculated using the condition the traveling times for the waves to arrive at the focal point are the same. For different velocities of the strikers, different distances can be obtained. The materials listed in Table 6.2 are used. Figure 6.3 shows the distances from chains of beads made of different materials from the middle chain as functions of velocity of the strikers. The black line in Figure 6.3 overlapped with the *x* axis denotes the middle chain. Only 8 chains are shown here because of the symmetry. As shown in Figure 6.3, the chains are not equally spaced in this example.

6.2.3 Discussions

In the numerical studies of the previous subsection, three different schemes were used to tune the acoustic lens. All of them have their own disadvantages. For scheme I, it is difficult to precisely (in the order of millinewton) apply precompression on the chains and to get identical dynamic contact forces for all chains subjected to different precompression in practice with simple experimental setup. For scheme II, although no additional precompression is required but to apply identical dynamic contact force simultaneously is still difficult for chains made of different materials. For scheme III, to get identical velocities for all strikers is a little easier, but Figure 6.3 shows that the distance between any two of aluminum, titanium and iron chains are less than the diameter of the beads for most cases, which is impractical.

7.0 CONCLUSIONS AND RECOMMENDATION FOR FUTURE STUDIES

7.1 CONCLUSIONS

In the fundamental research, the laser generation of HNSWs in a chain of stainless steel beads was investigated first. The ability of the short-duration pulsed laser for generating nonlinear solitary waves in a chain of spherical particles with variable precompression was demonstrated. The evolution of the excited pulse shape within the chain was studied experimentally, showing a rapid formation of a stationary wave after the 4^{th} particle from the excitation site. The experimentally measured dependence of the solitary wave velocity on the pulse amplitude was found in excellent agreement with the theoretical predictions for all precompression levels being tested. A simplified model that predicts the amount of dynamical contact force that can be generated in a chain of particle using a pulsed laser was proposed. This model can be used to estimate the mechanical pulse transferred to the granular system. This laser-based generation of HNSWs is non-contact, easy-to-control, and also able to generate multiple chains simultaneously, which is very difficult to achieve by dropping a mechanical striker. Then it was demonstrated that the electromagnetically induced precompression could be used to tune the properties of HNSWs such as wave speed and duration. The relation between the speed of HNSWs and the dynamic contact force for all precompression levels agreed with

theoretical prediction by the long wavelength approximation very well. The electromagnetically induced precompression is easy-to-control and can be changed gradually, and it does not change the boundary conditions used in numerical simulation. The method presented here provides an easy way to tune the HNSWs propagating in a one-dimensional chain of ferromagnetic or weakly magnetic beads.

A HNSW-transducer was designed and built. The designed HNSW transducer is compact, low cost and easy-to-control. It has good repeatability, tunability and doesn't need couplant and the use of electrical arbitrary function generator. The actuator consists of a one-dimensional chain of particles surmounted by an electromagnet that lifts and releases the striker from a certain height. By remotely activating the electromagnet the movement of the striker can be guaranteed with high level of repeatability. This automatic excitation of HNSWs could be useful in applications where a remote placement of equipment or a complex geometrical arrangement of the chains is required.

Several applications of the HNSW transducer were presented. In the cement setting monitoring test, it was shown that the HNSW-based method could be used to monitor the setting of cement paste and measure the elastic modulus of cement paste nondestructively at very early age. In the concrete curing monitoring test, it was found that a single pulse perpendicularly incident to the actuator/cement interface results in a series of reflected pulses, categorized into PSW and SSW. The amplitudes and TOFs of these two reflected waves are strongly dependent on the stiffness of the sample. The trend of the HNSWs characteristics were compared to the penetration resistance obtained from the ASTM C 403 [85] performed on mortar samples from the same mixture. As the concrete became stiffer, the TOF of both the PSW and SSW decreased

continuously. Two transition points were observed in the trend for the TOF with time. These points approximately corresponded to the times of initial and final set established by the ASTM C 403 test [85]. For both the cement setting and concrete curing monitoring tests, a thin aluminum sheet had to be inserted between the transducer and the specimens to prevent the last bead from falling into the fresh specimens. Adding the aluminum sheet not only made the numerical simulation more complicated, but also increased the degree of difficulty of conducting the experiment. Placing the aluminum sheet on top of the specimen at proper time was critical for both tests. If the aluminum sheet was placed too early, the specimen was not strong enough to hold the aluminum sheet and the transducer, and if the aluminum sheet was placed too late, the coupling between the aluminum sheet and the specimen would be bad which invalidated the experimental results. The HNSW transducer was also used to monitor the curing process of tow ton epoxy consisting resin and hardener for different resin/hardener ratios. By observing the characteristics of the reflected pulse, we were able to monitor the change of the epoxy's strength and discriminate different resin/hardener ratios. The HNSW features were able to discriminate good bond and fair bond from slip and disbond conditions in the aluminum lap-joint. The outlier analysis could help enhance the capability to discriminate good bond from fair bond. The composite plate with impact damage was inspected by the HNSW transducer, the transducer was only able to detect some of the damage, the reason might be that some damage did not result in stiffness difference which is large enough to be detected or the results mainly depended on the surface condition. Finally, the results of a preliminary numerical study on application of HNSWs in acoustic lens were presented.

7.2 RECOMMENDATION FOR FUTURE STUDIES

The HNSW transducer developed in this study is able to test a single point automatically, but when a large structure needs to be inspected, a scanning system which carries and places the HNSW transducer precisely is required to accelerate the inspection process.

The heterogeneous chain of beads that can temporarily store energy and then release the energy slowly during a relatively long time window could be used as a shock protector. A few preliminary studies have already been published, but the optimal design of such protector is a complicated problem and a lot of work needs to be done.

Acoustic diode [46] has the potential to be tuned to allow sound to pass through in only one way, which makes the “true soundproofing” possible. Another possible application of acoustic diode is energy harvesting. The implementation of acoustic diode in experiment is difficult but significant.

Acoustic lens studied in Chapter 6 has a huge potential range of applications such as military or medical uses. The generation of a “sound bullet” by acoustic lens has already been numerically simulated [50]. But the realization of precisely manipulating the sound waves in practice is still a challenging problem. The development of an automated, controllable, scalable acoustic lens able to generate high energy intensity acoustic waves is desired.

APPENDIX A

CALIBRATION OF THE SENSOR BEADS

The calibration procedures suggested by Eggenspieler [135] is summarized as follows.

1) Put the sensor bead on an aluminum plate and apply a small amount of FSA adhesive at the bottom of the sensor bead to avoid the rebound of the sensor bead when the striker hits the sensor bead. And make sure the sensor is orientated, such that the Piezo sensor layer, which is sandwich between two cut steel beads, is horizontal.

2) Place the hollow plastic rod vertically on the plate and make sure the sensor bead is in the middle of the rod, then apply glue between plastic rod and aluminum plate to fix the rod during the calibration.

3) Take a striker, an identical bead as the sensor bead except no PZT embedded.

4) Drop the striker from the height of h = 2cm.

5) Look at the oscilloscope to make sure no ringing problem exists. If any ringing problem is found, repeat steps 1-5, otherwise go to step 6.

6) Zoom the oscilloscope window, so that you only get Piezo pulse from zero to maximum or little over maximum in time. And use proper sampling rate in order to reduce the error in numerical integration.

7) Repeat the calibration process 10 times and save the data.

8) Use the Newton's formula to calculate the calibration constant. The Newton's formula is given as

$$Force = K \cdot Voltage$$

where K is the unknown calibrated coefficient.

$$v = \sqrt{2gh}$$

where v is the velocity of the striker when it hits the sensor bead, g is the gravity coefficient.

$$mv = \int_{t=t_0}^{t=t_f} F \cdot dt = K \int_{t=t_0}^{t=t_f} V(t) \cdot dt = K \cdot A$$

where m is the mass of the striker, A is the area between the curve of output voltage and the x axis from $t = t_0$ to $t = t_f$, which can be obtained by numerical integration, F is the dynamic force measured by the sensor bead.

Thus

$$K = \frac{mv}{A} = \frac{m\sqrt{2gh}}{A}$$

9) Repeat step 8 for ten acquisitions got in step 7 to get ten different values of K.

10) Calculate the relative standard deviation, if the relative standard deviation is less than the selected threshold, select the mean value of K as the final K value.

PUBLICATIONS STEMMED FROM THIS WORK

Peer-reviewed journal papers

Xianglei Ni, Piervincenzo Rizzo, and Chiara Daraio. Laser-based excitation of nonlinear solitary waves in a chain of particles. *Physical Review E*. 84(2):026601-1-026601-5, 2011.

Xianglei Ni, Piervincenzo Rizzo, and Chiara Daraio. Actuators for the generation of highly nonlinear solitary waves . *Review of Scientific Instruments*. 82(3):034902-1-034902-6, 2011.

Xianglei Ni and Piervincenzo Rizzo. Use of highly nonlinear solitary waves in NDT. *submitted to Materials Evaluation*.

Xianglei Ni, Piervincenzo Rizzo, Jinkyu Yang, Devvrath Kathri, and Chiara Daraio.Monitoring the Hydration of Cement Using Highly Nonlinear Solitary Waves. *submitted to NDT & E International*.

Xianglei Ni and Piervincenzo Rizzo. Highly nonlinear solitary waves for the inspection of adhesive joints. *submitted to Experimental Mechanics*.

Xianglei Ni, Somayeh Nassiri, Piervincenzo Rizzo, and Julie Vandenbossche. Monitoring strength development in fresh concrete using highly nonlinear solitary waves. *in preparation*.

Conference papers

Xianglei Ni, Piervincenzo Rizzo, and Chiara Daraio. Novel sensor technology for NDE of concrete. *Proc. SPIE*. 7292:729218, 2009.

Xianglei Ni, Ricki Garden, and Piervincenzo Rizzo. Novel actuator based on the stress wave propagation in highly nonlinear materials. *Proceedings of Structural Health Monitoring*. 2009.

Xianglei Ni, Ricki Garden, and Piervincenzo Rizzo. Laser induced highly nonlinear solitary waves for structural NDE. *Proc. SPIE*. 7647:76470S, 2010.

Xianglei Ni, Somayeh Nassiri, Piervincenzo Rizzo, and Julie Vandenbossche. Highly nonlinear solitary waves-based sensor for monitoring concrete. *Proc. SPIE*. 7981:79812L, 2011.

Xianglei Ni and Piervincenzo Rizzo. SHM of structural materials by means of highly nonlinear solitary waves. *Proceedings of Structural Health Monitoring*. 2011.

BIBLIOGRAPHY

[1] Peter J. Shull. *Nondestructive Evaluation: Theory, Techniques, and Applications*. Marcel Dekker, 2002.

[2] http://www.asnt.org/ndt/primer1.htm

[3] Vitali F. Nesterenko. *Dynamics of Heterogeneous Materials*. Springer, 2001.

[4] V. F. Nesterenko. Propagation of nonlinear compression pulses in granular media. *Journal of Applied Mechanics and Technical Physics*, 24(5):733-743, 1983.

[5] A. N. Lazaridi and V. F. Nesterenko. Observation of a new type of solitary waves in a one-dimensional granular medium. *Journal of Applied Mechanics and Technical Physics*, 26(3):405-408, 1985.

[6] V. F. Nesterenko, A. N. Lazaridi and E. B. Sibiryakov. The decay of soliton at the contact of two "acoustic vacuums". *Journal of Applied Mechanics and Technical Physics*, 36(2):166-168, 1995.

[7] C. Coste, E. Falcon, and S. Fauve. Solitary waves in a chain of beads under Hertz contact. *Physical Review E*, 56(5):6104-6117, 1997.

[8] E. Falcon, C. Laroche, S. Fauve and C. Coste. Collision of a 1-D column of beads with a wall. *The European Physical Journal B*. 5(1):111-131, 1998.

[9] Surajit Sen, Marian Manciu, and James D. Wright. Solitonlike pulses in perturbed and driven Hertzian chains and their possible applications in detecting buried impurities. *Physical Review E*. 57(2):2386-2397, 1998.

[10] Anindya Chatterjee. Asymptotic solution for solitary waves in a chain of elastic spheres. *Physical Review E*. 59(5):5912-5919, 1999.

[11] Surajit Sen, Marian Manciu, and Felicia S. Manciu. Ejection of ferrofluid grains using nonlinear acoustic impulses— A particle dynamical study. *Applied Physics Letters*. 75(10):1479-1481, 1999.

[12] C. Coste and B. Gilles. On the validity of Hertz contact law for granular material acoustics. *The European Physical Journal B*. 7(1):155-168, 1999.

[13] E. J. Hinch and S. Saint–Jean. The fragmentation of a line of balls by an impact. *Proceedings of the Royal Society A*. 455(1989):3201-3220, 1999.

[14] Marian Manciu, Surajit Sen, Alan J Hurd. The propagation and backscattering of soliton-like pulses in a chain of quartz beads and related problems. (I). Propagation. *Physica A*. 274(3-4):588-606, 1999.

[15] Marian Manciu, Surajit Sen, Alan J Hurd. The propagation and backscattering of soliton-like pulses in a chain of quartz beads and related problems. (II). Backscattering. *Physica A*. 274(3-4):607-618, 1999.

[16] Marian Manciu, Surajit Sen, Alan J Hurd. Crossing of identical solitary waves in a chain of elastic beads. *Physical Review E*. 63(1):016614-1-016614-6, 2000.

[17] Marian Manciu, Surajit Sen, and Alan J. Hurd. Impulse propagation in dissipative and disordered chains with power-law repulsive potentials. *Physica D*. 157(3):226-240, 2001.

[18] Surajit Sen and Marian Manciu. Solitary wave dynamics in generalized Hertz chains: An improved solution of the equation of motion. *Physical Review E*. 64(5):056605-1-056605-4, 2001.

[19] Ai-Guo Xu and Jongbae HONG. Soliton-Like Pulses in Vertical Granular Chain Under Gravity: Particle-Like or Wave-Like?. *Communications in Theoretical Physics*. 35(1):106-113, 2001.

[20] Jongbae Hong and Aiguo Xu. Nondestructive identification of impurities in granular medium. *Applied Physics Letters*. 81(25):4868-4870, 2002.

[21] Felicia S. Manciu and Surajit Sen. Secondary solitary wave formation in systems with generalized Hertz interactions. *Physical Review E*. 66(1): 016616-1-016616-11, 2002.

[22] V. F. Nesterenko, C. Daraio, E. B. Herbold, and S. Jin. Anomalous Wave Reflection at the Interface of Two Strongly Nonlinear Granular Media. *Physical Review Letters*. 95(15):158702-1-158702-4, 2005.

[23] Stéphane Job, Francisco Melo, Adam Sokolow and Surajit Sen. How Hertzian Solitary Waves Interact with Boundaries in a 1D Granular Medium. *Physical Review Letters*. 94(17):178002-1-178002-4, 2005.

[24] Lautaro Vergara. Scattering of Solitary Waves from Interfaces in Granular Media. *Physical Review Letters*. 95(10):108002-1108002-4, 2005.

[25] C. Daraio, V. F. Nesterenko1, E. B. Herbold, and S. Jin. Strongly nonlinear waves in a chain of Teflon beads. *Physical Review E*. 72(1):016603-1-016603-9, 2005.

[26] Jongbae Hong. Universal Power-Law Decay of the Impulse Energy in Granular Protectors. *Physical Review Letters*. 94(10):108001-1-108001-4, 2005.

[27] C. Daraio, V. F. Nesterenko, E. B. Herbold, and S. Jin. Energy Trapping and Shock Disintegration in a Composite Granular Medium. *Physical Review Letters*. 96(5):058002-1-058002-4, 2006.

[28] C. Daraio and V. F. Nesterenko. Strongly nonlinear wave dynamics in a chain of polymer coated beads. *Physical Review E*. 73(2):026612-1-026612-7, 2006.

[29] C. Daraio, V. F. Nesterenko, E. B. Herbold, and S. Jin. Tunability of solitary wave properties in one-dimensional strongly nonlinear phononic crystals. *Physical Review E*. 73(2):026610-1-026610-10, 2006.

[30] Alexandre Rosas, Aldo H. Romero, Vitali F. Nesterenko, and Katja Lindenberg. Observation of Two-Wave Structure in Strongly Nonlinear Dissipative Granular Chains. *Physical Review Letters*. 98(16):164301-1-164301-4, 2007.

[31] Stephane Job, Francisco Melo, Adam Sokolow, and Surajit Sen. Solitary wave trains in granular chains: Experiments, theory and simulations. *Granular Matter*. 10(1):13-20, 2007.

[32] Mason A. Porter, Chiara Daraio, Eric B. Herbold, Ivan Szelengowicz, and P. G. Kevrekidis. Highly nonlinear solitary waves in periodic dimer granular chains. *Physical Review E*. 77(1):015601-1-015601-4, 2008.

[33] Surajit Sen, Jongbae Hong, Jonghun Bang, Edgar Avalos, and Robert Doney. Solitary waves in the granular chain. *Physics Reports*. 462(2):21-66, 2008.

[34] Devvrath Khatri, Chiara Daraio and Piervincenzo Rizzo. Coupling of highly nonlinear waves with linear elastic media. *Proc. SPIE*. 7292:72920P, 2009.

[35] R. Carretero-González, D. Khatri, Mason A. Porter, P. G. Kevrekidis, and C. Daraio. Dissipative Solitary Waves in Granular Crystals. *Physical Review Letters*. 102(2):024102-1024102-4, 2009.

[36] Mason A. Porter, Chiara Daraio, Ivan Szelengowicz, Eric B. Herbold, and P.G. Kevrekidis. Highly nonlinear solitary waves in heterogeneous periodic granular media. *Physica D*. 238(6):666-676, 2009.

[37] G. Theocharis, M. Kavousanakis, P. G. Kevrekidis, Chiara Daraio, Mason A. Porter, and I. G. Kevrekidis. Localized breathing modes in granular crystals with defects. *Physical Review E*. 80(6):066601-1-066601-11, 2009.

[38] Alain Molinari and Chiara Daraio. Stationary shocks in periodic highly nonlinear granular chains. *Physical Review E*. 80(5):056602-1-056602-15, 2009.

[39] E. B. Herbold, J. Kim, V. F. Nesterenko, S. Wang, and C. Daraio. Tunable frequency band-gap and pulse propagation in a strongly nonlinear diatomic chain. *Acta Mechanica*. 205(1-4):85-103, 2009.

[40] Fernando Fraternali, Mason A. Porter, and Chiara Daraio. Optimal Design of Composite Granular Protectors. *Mechanics of Advanced Materials and Structures*. 17(1): 1-19, 2010.

[41] N. Boechler, G. Theocharis, S. Job, P. G. Kevrekidis, Mason A. Porter, and C. Daraio. Discrete Breathers in One-Dimensional Diatomic Granular Crystals. *Physical Review Letters*. 104(24): 244302-1-244302-4, 2010.

[42] G. Theocharis, N. Boechler, P. G. Kevrekidis, S. Job, Mason A. Porter, and C. Daraio. Intrinsic energy localization through discrete gap breathers in one-dimensional diatomic granular crystals. *Physical Review E*. 82(5):056604-1-056604-11, 2010.

[43] Laurent Ponson, Nicholas Boechler, Yi Ming Lai, Mason A. Porter, P. G. Kevrekidis, and Chiara Daraio. Nonlinear waves in disordered diatomic granular chains. *Physical Review E*. 82(2):021301-1-021301-9, 2010.

[44] C. Daraio, D. Ngo, V. F. Nesterenko, and F. Fraternali. Highly nonlinear pulse splitting and recombination in a two-dimensional granular network. *Physical Review E*. 82(3):036603-1-036603-8, 2010.

[45] Alessandro Spadoni and Chiara Daraio. Generation and control of sound bullets with a nonlinear acoustic lens. *Proceedings of the National Academy of Sciences of the United States of America*. 107(16):7230-7234, 2010.

[46] N. Boechler, G. Theocharis, and C. Daraio. Bifurcation-based acoustic switching and rectification. *Nature Materials*. 10(9):665-668, 2011.

[47] A. Leonard, F. Fraternali and C. Daraio. Directional Wave Propagation in a Highly Nonlinear Square Packing of Spheres. *Experimental Mechanics*. Online First, 2011.

[48] N. Boechler, J. Yang, G. Theocharis, P. G. Kevrekidis, and C. Daraio. Tunable vibrational band gaps in one-dimensional diatomic granular crystals with three-particle unit cells. *Journal of Applied Physics*. 109(7):074906-1-074906-7, 2011.

[49] Duc Ngo, Devvrath Khatri, and Chiara Daraio. Highly nonlinear solitary waves in chains of ellipsoidal particles. *Physical Review E*. 84(2):026610-1-026610-7, 2011.

[50] A. Spadoni, C. Daraio, W. Hurst, and M. Brown. Nonlinear phononic crystals based on chains of disks alternating with toroidal structures. *Applied Physics Letters*. 98(16):161901-1-161901-3, 2011.

[51] Jinkyu Yang, Claudio Silvestro, Devvrath Khatri, Luigi De Nardo, and Chiara Daraio. Interaction of highly nonlinear solitary waves with linear elastic media. *Physical Review E*. 83(4):046606-1-046606-12, 2011.

[52] L. D. Landau and E. M. Lifshitz. *Theory of Elasticity*. 3rd Edition. Pergamon, 1986.

[53] R. m. White. Generation of elastic waves by transient surface heating. *Journal of Applied Physics*. 34(12):3559-3567, 1963.

[54] D. A. Hutchins. Ultrasonic generation by pulsed lasers, in *Physical Acoustics*, Vol. XVIII, Mason, W.P., and Thurston, R.N., Academic Press, New York, 1988, pp. 21–123.

[55] C. B. Scruby and L. E. Drain. *Laser ultrasonics: techniques and applications*. Adam Hilder, New York, 1990.

[56] J. D. Aussel and J. P. Monchalin. Precision laser-ultrasonic velocity measurement and elastic constant determination. *Ultrasonics*. 27(3):165-177, 1989.

[57] Shi-Chang Wooh and Quanlin Zhou. Behavior of laser-induced ultrasonic waves radiated from a wet surface. Part I. Theory. *Journal of Applied Physics*. 89(6):3469-3477, 2001.

[58] Shi-Chang Wooh and Quanlin Zhou. Behavior of laser-induced ultrasonic waves radiated from a wet surface. Part II. Experimental work. *Journal of Applied Physics*. 89(6):3478-3485, 2001.

[59] Francesco Lanza di Scalea, Piervincenzo Rizzo, and Alessandro Marzani. Propagation of ultrasonic guided waves in lap-shear adhesive joints: Case of incident a0 Lamb wave. *Journal of the Acoustical Society of America*. 115(1):146-156, 2004.

[60] C. Thomsen, H. T. Grahn, H. J. Maris, and J. Tauc. Surface generation and detection of phonons by picosecond light pulses. *Physical Review B*. 34(6):4129-4138, 1986.

[61] http://en.wikipedia.org/wiki/Electromagnet

[62] K. Van Den Abeele, W. Desadeleer, G. De Schutter, and M. Wevers. Active and passive monitoring of the early hydration process in concrete using linear and nonlinear acoustics. *Cement and Concrete Research*. 39(5):426-432, 2009.

[63] Jinying Zhu and Seong-Hoon Kee. Monitoring early age microstructure development of cement paste using bender elements. *Proc. SPIE*. 7649:76491R, 2010.

[64] C.M. Sayers and R.L. Grenfell. Ultrasonic propagation through hydrating cements. *Ultrasonics*. 31(3):147-153, 1993.

[65] A. Smith, T. Chotard, N. Gimet-Breart, and D. Fargeot. Correlation between hydration mechanism and ultrasonic measurements in an aluminous cement: effect of setting time and temperature on the early hydration. *Journal of the European Ceramic Society*. 22(12):1947-1958, 2002.

[66] Thomas Voigt, Guang Ye, Zhihui Sun, Surendra P. Shah, and Klaas van Breugel. Early age microstructure of Portland cement mortar investigated by ultrasonic shear waves and numerical simulation. *Cement and Concrete Research*. 35(5):858-866, 2005.

[67] J. Stepišnik, M. Lukač, and I. Kocuvan. Measurement of cement hydration by ultrasonics. *American Ceramic Society Bulletin*. 60(4):481-483, 1981.

[68] Prabhakar P. Rao, David L. Sutton, Jerry D. Childs, and Willis C. Cunningham. An Ultrasonic Device for Nondestructive Testing of Oilwell Cements at Elevated Temperatures and Pressures. *Journal of Petroleum Technology*. 34(11):2611-2616, 1982.

[69] J. Keating, D.J. Hannant, and A.P. Hibbert. Comparison of shear modulus and pulse velocity techniques to measure the build-up of structure in fresh cement pastes used in oil well cementing. *Cement and Concrete Research*. 19(4):554-566, 1989.

[70] J. Keating, D.J. Hannant, and A.P. Hibbert. Correlation between cube strength, ultrasonic pulse velocity and volume change for oil well cement slurries. *Cement and Concrete Research*. 19(5):715-726, 1989.

[71] C.M. Sayers and A. Dahlin. Propagation of ultrasound through hydrating cement pastes at early times. *Advanced Cement Based Materials*. 1(1):12-21, 1993.

[72] Ralph D'Angelo, Thomas J. Plona, Lawrence M. Schwartz, and Peter Coveney. Ultrasonic measurements on hydrating cement slurries: Onset of shear wave propagation. *Advanced Cement Based Materials*. 2(1):8-14, 1995.

[73] A. Boumiz, C. Vernet, and F.Cohen Tenoudji. Mechanical properties of cement pastes and mortars at early ages: Evolution with time and degree of hydration. *Advanced Cement Based Materials*. 3(3-4):94-106, 1996.

[74] M.I. Valič. Hydration of cementitious materials by pulse echo USWR: Method, apparatus and application examples. *Cement and Concrete Research*. 30(10):1633-1640, 2000.

[75] T. Chotard, N. Gimet-Breart, A. Smith, D. Fargeot, J.P. Bonnet, and C. Gault. Application of ultrasonic testing to describe the hydration of calcium aluminate cement at the early age. *Cement and Concrete Research*. 31(3):405-412, 2001.

[76] G. Ye, K. van Breugel, and A.L.A. Fraaij. Experimental study and numerical simulation on the formation of microstructure in cementitious materials at early age. *Cement and Concrete Research*. 33(2):233-239, 2003.

[77] T. Öztürk, O. Kroggel, P. Grübl, and J.S. Popovics. Improved ultrasonic wave reflection technique to monitor the setting of cement-based materials. *NDT & E International*. 39(4):258-263, 2006.

[78] Wonsiri Punurai, Jacek Jarzynski, Jianmin Qu, Kimberly E. Kurtis, and Laurence J. Jacobs. Characterization of entrained air voids in cement paste with scattered ultrasound. *NDT & E International*. 39(6):514-524, 2006.

[79] Jie Zhang, Lei Qin, and Zongjin Li. Hydration monitoring of cement-based materials with resistivity and ultrasonic methods. *Materials and Structures*. 42(1):15-24, 2009.

[80] Q.L. Yu, H.J.H. Brouwers, and A.C.J. Korte de. Gypsum hydration: a theoretical and experimental study. In: *17th International Conference on Building Materials*, ibausil, Weimar, Germany, 2009.

[81] M. Moukwa, M. Brodwin, S. Christo, J. Chang, and S.P. Shah. The influence of the hydration process upon microwave properties of cements. *Cement and Concrete Research*. 21(5):863-872, 1991.

[82] Youssef El Hafiane, Agnès Smith, Jean Pierre Bonnet, Pierre Abelard, and Philippe Blanchart. Electrical characterization of aluminous cement at the early age in the 10 Hz–1 GHz frequency range. *Cement and Concrete Research*. 30(7):1057-1062, 2000.

[83] Tarun R. Naik, V. Mohan Malhotra, and John S. Popovics. The Ultrasonic Pulse Velocity Method. In: *Handbook on Nondestructive testing of concrete*. edited by V.M. Malhotra and Nicholas J. Carino. CRC Press, Boca Raton, 2004.

[84] ASTM C 109/C 109M – 08. *Standard test method for compressive strength of hydraulic cement mortars*.

[85] ASTM, ASTM C 403 / C403M-08. In *Standard test method for time of setting of concrete mixtures by penetration resistance*. PA, 1999.

[86] McCullough FB, Rasmussen RO. Fast-track paving: Concrete temperature control and traffic opening criteria for bonded concrete overlays, *FHWA-RD-98-167*. Mclean, VA, 1999.

[87] N. De Belie, C.U. Grosse, J. Kurz, H.-W. Reinhardt. Ultrasound monitoring of the influence of different accelerating admixtures and cement types for shotcrete on setting and hardening behaviour. *Cement and Concrete Research*. 35(11):2087-2094, 2005.

[88] H.K. Lee, K.M. Lee, Y.H. Kim, H. Yim, D.B. Bae. Ultrasonic in-situ monitoring of setting process of high-performance concrete. *Cement and Concrete Research*. 34(4):631-640, 2004.

[89] Stephen Pessiki and Matthew R. Johnson. Nondestructive Evaluation of Early-Age Concrete Strength in Plate Structures by the Impact-Echo Method. *ACI Materials Journal*. 93(3):260-271, 1996.

[90] Stephen P. Pessiki and Nicolas J. Carino. Setting Time and Strength of Concrete Using the Impact-Echo Method. *ACI Materials Journal*. 85(5):389-399, 1988.

[91] H.W. Reinhardt and C.U. Grosse. Continuous monitoring of setting and hardening of mortar and concrete. *Construction and Building Materials*. 18(3):145-154, 2004.

[92] Nicolas Robeyst, Elke Gruyaert, Christian U. Grosse, and Nele De Belie. Monitoring the setting of concrete containing blast-furnace slag by measuring the ultrasonic p-wave velocity. *Cement and Concrete Research*. 38(10):1169-1176, 2008.

[93] G. Ye, P. Lura, K. van Breugel, and A.L.A. Fraaij. Study on the development of the microstructure in cement-based materials by means of numerical simulation and ultrasonic pulse velocity measurement. *Cement and Concrete Composites*. 26(5):491-497, 2004.

[94] Th. Voigt, Ch. U. Grosse, Z. Sun, S. P. Shah, and H. -W. Reinhardt. Comparison of ultrasonic wave transmission and reflection measurements with P- and S-waves on early age mortar and concrete. *Materials and Structures*. 38(8):729-738, 2005.

[95] Julie R. Rapoport, John S. Popovics, Subramaniam V. Kolluru, and Surendra P. Shah. Using Ultrasound to Monitor Stiffening Process of Concrete with Admixtures. *ACI Materials Journal*. 97(6):675-683, 2000.

[96] Kolluru V. Subramaniam, J. P. Mohsen, C. K. Shaw, and S. P. Shah. Ultrasonic Technique for Monitoring Concrete Strength Gain at Early Age. *ACI Materials Journal*. 99(5):458-462, 2002.

[97] T. Voigt, Y. Akkaya, and S.P. Shah. Determination of Early Age Mortar and Concrete Strength by Ultrasonic Wave Reflections. *Journal of Materials in Civil Engineering*. 15(3):247-254, 2003.

[98] Thomas Voigt and Surendra P. Shah. Properties of Early-Age Portland Cement Mortar Monitored with Shear Wave Reflection Method. *ACI Materials Journal*. 101(6):473-482, 2004.

[99] Kolluru V. Subramaniam, Jaejun Lee, and Bruce J. Christensen. Monitoring the setting behavior of cementitious materials using one-sided ultrasonic measurements. *Cement and Concrete Research*. 35(5):850-857, 2005.

[100] Y. Akkaya, T. Voigt, K. V. Subramaniam, and S. P. Shah. Nondestructive measurement of concrete strength gain by an ultrasonic wave reflection method. *Materials and Structures*. 36(8):507-514, 2003.

[101] V. Garnier, G. Corneloup, J.M. Sprauel, and J.C. Perfumo. Setting time study of roller compacted concrete by spectral analysis of transmitted ultrasonic signals. *NDT & E International*. 28(1):15-22, 1995.

[102] T. Öztürk, J. Rapoport, J. S. Popovics, and S. P. Shah. Monitoring the setting and hardening of cement-based materials with ultrasound. *Concrete Science and Engineering*. 1(2):83-91, 1999.

[103] S.H. Pu, F. Cegla, M. Drozdz, M.J.S. Lowe, P. Cawley, and N.R. Buenfeld. Monitoring the setting and early hardening of concrete using an ultrasonic waveguide. *Insight - Non-Destructive Testing and Condition Monitoring*. 46(6):350-354, 2004.

[104] Seung-Seok Lee, Joon Hyun Lee, Ik Keun Park, Sung-Jin Song, and Man Yong Choi. Nondestructive Curing Monitoring of Early-Age Concrete Using Rayleigh Wave Velocity. *Key Engineering Materials*. 321-323:318-321, 2006.

[105] Sung Woo Shin, Chung Bang Yun, John S. Popovics, and Jae Hong Kim. Improved Rayleigh Wave Velocity Measurement for Nondestructive Early-Age Concrete Monitoring. *Research in Nondestructive Evaluation*. 18(1):45-68, 2007.

[106] B. Glišić and N. Simon. Monitoring of concrete at very early age using stiff SOFO sensor. *Cement and Concrete Composites*. 22(2):115-119, 2000.

[107] K. Van Den Abeele, W. Desadeleer, G. De Schutter, M. Wevers. Active and passive monitoring of the early hydration process in concrete using linear and nonlinear acoustics. *Cement and Concrete Research*. 39(5):426-432, 2009.

[108] J. J. Peters, D. J. Barnard, N. A. Hudelson, T. S. Simpson, and D. K. Hsu. A prototype tap test imaging system: Initial field test results. *Review of Progress in Quantitative Nondestructive Evaluation*. 19:2053-2060, 2000.

[109] David K. Hsu. Nondestructive Evaluation of Sandwich Structures: A Review of Some Inspection Techniques. *Journal of Sandwich Structures and Materials*. 11(4):275-291, 2009.

[110] G. Ji, Z. Ouyang, and G. Li. Local Interface Shear Fracture of Bonded Steel Joints with Various Bondline Thicknesses. *Experimental Mechanics*. Online first.

[111] R.D. Adams and B.W. Drinkwater. Nondestructive testing of adhesively-bonded joints. *NDT & E International*. 30(2):93-98, 1997.

[112] C. Meola, G.M. Carlomagno, and L. Giorleo. Non-destructive evaluation of bonded structures with lock-in thermography. *Journal of Adhesion Science and Technology*. 17(9):1207-1222, 2003.

[113] J.A. Schroeder, T. Ahmed, B. Chaudhry, and S. Shepard. Non-destructive testing of structural composites and adhesively bonded composite joints: pulsed thermography. *Composites Part A*. 33(11):1511-1517, 2002.

[114] Carosena Meola, Giovanni M. Carlomagno, Antonino Squillace, and Giuseppe Giorleo. The use of infrared thermography for nondestructive evaluation of joints. *Infrared Physics & Technology*. 46(1-2):93-99, 2004.

[115] Hassan A. Jama, Esam M.A. Hussein, and Pearl Lee-Sullivan. Detection of debonding in composite-aluminum joints using gamma-ray Compton scattering. *NDT & E International*. 31(2):99-103, 1998.

[116] Cezary Gozdecki and Jerzy Smardzewski. Detection of failures of adhesively bonded joints using the acoustic emission method. *Holzforschung*. 59(2):219-229, 2005.

[117] C. Cosenza, D. Cerniglia, and B.B. Djordjevic. Non-contact ultrasonic inspection of skin/core bond in honeycomb with Lamb waves. *Proceedings. 2002 IEEE: Ultrasonics Symposium*. 1:749-752, 2002.

[118] F. Lanza di Scalea, P. Rizzo, and A. Marzani. Assessment of bond state in lap-shear joints by guided wave transmission monitoring. *Insight - Non-Destructive Testing and Condition Monitoring*. 46(3):135-141, 2004.

[119] F. Lanza di Scalea, M. Bonomo, and D. Tuzzeo. Ultrasonic Guided Wave Inspection of Bonded Lap Joints: Noncontact Method and Photoelastic Visualization. *Research in Nondestructive Evaluation*. 13(3):153-171, 2001.

[120] Bénédicte Le Crom and Michel Castaings. Shear horizontal guided wave modes to infer the shear stiffness of adhesive bond layers. *Journal of the Acoustical Society of America*. 127(4):2220-2230, 2010.

[121] S. E. Hanneman, V. K. Kinra, and C. Zhu. A new technique for ultrasonic nondestructive evaluation of adhesive joints: Part II. Experiment. *Experimental Mechanics*. 32(4):332-339, 1992.

[122] P. Cawley and R.D. Adams. Sensitivity of the coin-tap method of nondestructive testing. *Materials Evaluation*. 47:558-563, 1989.

[123] P. Cawley and R.D. Adams. The mechanics of the coin-tap method of non-destructive testing. *Journal of Sound and Vibration*. 122(2):299-316, 1988.

[124] Peter Cawley. A high frequency coin-tap method of non-destructive testing. *Mechanical Systems and Signal Processing*. 5(1):1-11, 1991.

[125] Huadong Wu and M. Siegel. Correlation of accelerometer and microphone data in the "coin tap test". *IEEE Transactions on Instrumentation and Measurement*. 49(3):493-497, 2000.

[126] David K. Hsu, Daniel J. Barnard, John J. Peters, and Vinay Dayal. Physical basis of tap test as a quantitative imaging tool for composite structures on aircraft. *Review of Progress in Quantitative Nondestructive Evaluation*. 19:1857-1864, 2000.

[127] John J. Peters, Zachary A. Nielsen, and David K. Hsu. Comparison of local stiffness of composite honeycomb sandwich structures measured by tap test and mechanical test. *Review of Progress in Quantitative Nondestructive Evaluation*. 20:1031-1038, 2001.

[128] S. Baglio and N. Savalli. "Fuzzy tap-testing" sensors for material health-state characterization. *IEEE Transactions on Instrumentation and Measurement*. 55(3):761-770, 2006.

[129] D. Barnard, C. Foreman, and D. Hsu. Generating tap test images with a free-hand motorized tapper. *Review of Progress in Quantitative Nondestructive Evaluation*. 28:1680-1686, 2009.

[130] Robert Lee Crane and Giles Dillingham. Composite bond inspection. *Journal of Materials Science*. 43(20):6682-6694, 2008.

[131] Piervincenzo Rizzo, Marcello Cammarata, Debaditya Dutta, Hoon Sohn, and Kent Harries. An unsupervised learning algorithm for fatigue crack detection in waveguides. *Smart Materials and Structures*. 18(2):025016-1-025016-11, 2009.

[132] Piervincenzo Rizzo, Elisa Sorrivi, Francesco Lanza di Scalea, and Erasmo Viola. Wavelet-based outlier analysis for guided wave structural monitoring: Application to multi-wire strands. *Journal of Sound and Vibration*. 307(1-2):52-68, 2007.

[133] K. Worden, G. Manson, and N.R.J. Fieller. Damage detection using outlier analysis. *Journal of Sound and Vibration*. 229(3):647-667, 2000.

[134] Sergios Theodoridis and Konstantinos Koutroumbas. *Pattern recognition*. Academic Press, San Diego, California, 2008.

[135] D. Eggenspieler. *Non destructive evaluation using phononic-crystal meta-material*. Internal report, California Institute of Technology, 2008.